

Duygu Tahaoglu

A Ph.D. Thesis

AGU 2022

# MODELLING AND INVESTIGATION OF BORON-BASED NANOSTRUCTURES

A THESIS

SUBMITTED TO THE DEPARTMENT OF MATERIALS SCIENCE  
AND MECHANICAL ENGINEERING  
AND THE GRADUATE SCHOOL OF ENGINEERING AND SCIENCE  
OF ABDULLAH GUL UNIVERSITY  
IN PARTIAL FULFILLMENT OF THE REQUIREMENTS  
FOR THE DEGREE OF  
DOCTOR OF PHILOSOPHY

By

Duygu TAHAOĞLU

June 2022

# MODELLING AND INVESTIGATION OF BORON-BASED NANOSTRUCTURES

A THESIS

SUBMITTED TO THE DEPARTMENT OF MATERIALS SCIENCE AND  
MECHANICAL ENGINEERING  
AND THE GRADUATE SCHOOL OF ENGINEERING AND SCIENCE OF  
ABDULLAH GUL UNIVERSITY  
IN PARTIAL FULFILLMENT OF THE REQUIREMENTS  
FOR THE DEGREE OF  
DOCTOR OF PHILOSOPHY

By

Duygu TAHAOĞLU

June 2022

## SCIENTIFIC ETHICS COMPLIANCE

I hereby declare that all information in this document has been obtained in accordance with academic rules and ethical conduct. I also declare that, as required by these rules and conduct, I have fully cited and referenced all materials and results that are not original to this work.

Name-Surname: Duygu TAHAOĞLU

Signature :

## REGULATORY COMPLIANCE

Ph.D. thesis titled “Modelling and Investigation of Boron-Based Nano Structures” has been prepared in accordance with the Thesis Writing Guidelines of the Abdullah Gül University, Graduate School of Engineering & Science.

Prepared By  
Duygu TAHAOĞLU

Advisor  
Prof. Dr.Murat DURANDURDU

Co-Advisor  
Assist. Prof. Fahri  
ALKAN

Head of the Materials Science and Mechanical Engineering Program  
Prof. Dr. Murat DURANDURDU



## ACCEPTANCE AND APPROVAL

Ph.D. thesis titled “Modelling and Investigation of Boron-Based Nano Structures” and prepared by Duygu TAHAOĞLU has been accepted by the jury in the Materials Science and Mechanical Engineering Graduate Program at Abdullah Gül University, Graduate School of Engineering & Science.

28 / 06 / 2022

(Thesis Defense Exam Date)

### JURY:

Advisor : Prof. Dr. Murat DURANDURDU .....

Member : Prof. Dr. Hakan USTA.....

Member : Prof. Dr. Serdar ÖNSES .....

Member : Prof. Dr. Mehmet ŞAHİN .....

Member : Prof. Dr. Zeki BÜYÜKMUMCU .....

### APPROVAL:

The acceptance of this Ph.D. thesis has been approved by the decision of the Abdullah Gül University, Graduate School of Engineering & Science, Executive Board dated ..... /..... / 2022 and numbered .....

..... /..... / .....

Graduate School Dean  
Prof. Dr. İrfan ALAN

# ABSTRACT

## MODELLING AND INVESTIGATION OF BORON-BASED NANOSTRUCTURES

Duygu TAHAOĞLU  
Ph.D. in Materials Science and Mechanical Engineering  
**Advisor:** Prof. Dr. Murat DURANDURDU  
**Co-Advisor:** Assist. Prof. Fahri ALKAN

June 2022

Polyhedral boron clusters and their applications have been subject to research in many fields such as medicine, materials science, catalytic applications, energy studies, etc. These molecules owe their popularity to their exceptional 3D stable structures, as well as their various sought-after properties in many applications. This doctoral thesis was prepared within the focus of a computational investigation of different polyhedral borane and carborane clusters by using DFT methods. The results of our studies were reported in two main chapters (Chapters 3 and 4). In the first part (Chapter 3), theoretical evaluation of relative stabilities and electronic structure for  $[B_nX_n]^{2-}$  clusters were provided. The structural and electronic characteristics of  $[B_nX_n]^{2-}$  clusters were examined by comparison with the  $[B_{12}X_{12}]^{2-}$  counterparts with a focus on the substituent effects ( $X = H, F, Cl, Br, CN, BO, OH, NH_2$ ). The effects of the substituents were discussed in relation to their mesomeric ( $\pm M$ ) and inductive ( $\pm I$ ) effects. The results showed that the icosahedral barrier can be reduced through substitution by destabilizing the  $[B_{12}X_{12}]^{2-}$  cluster with symmetry-reducing ligands or ligands with +M effects rather than stabilizing the larger clusters. In the second part (Chapter 4), the investigation of the photophysical properties of carborane-containing luminescent systems was presented. The *o*-CB-*Anth* system is known to exhibit a dual-emission property by radiating in the visible region from two low energy conformations with local excited (LE) and hybridized local and charge transfer (HLCT) characters, however, it shows a very low emission quantum yield in solution state similar to many other CB-luminescent systems. In this section, the excited-state potential energy surface (PES) of *o*-CB-*Anth* and *o*-CB-*Pent* were investigated in detail and the effect of a low-lying CT on the low quantum yield was discussed.

*Keywords: Borane dianions, Icosahedral barrier, Carboranes, Luminescent materials, Substitution*

# ÖZET

## BORON BAZLI NANO YAPILARIN MODELLENMESİ VE İNCELENMESİ

Duygu TAHAOĞLU  
Malzeme Bilimi ve Makine Mühendisliği Anabilim Dalı Doktora  
Tez Yöneticisi: Prof. Dr. Murat DURANDURDU  
Eş Danışman: Assist. Prof. Fahri ALKAN

Haziran-2022

Çokyüzlü bor kümeleri ve uygulamaları tıp, malzeme bilimi, katalitik uygulamalar, enerji çalışmaları vb. Birçok alanda araştıma konusu olmuştur. Bu moleküller, popülerliklerini kararlı 3 boyutlu yapılarının yanında sahip oldukları, ve birçok uygulama alanında aranan özelliklerine borçludur. Bu doktora tezi, farklı çokyüzlü boran ve karboran kümelerinin yoğunluk fonksiyonu teorisi metotları kullanılarak hesaplamalı olarak incelenmesi odağında hazırlanmıştır. Çalışmalarımızın sonuçları iki ana bölümde rapor edilmiştir (Chapter 3 ve 4). Birinci bölümde,  $[B_nX_n]^{2-}$  kümelerinin bağlı kararlılıklarının ve elektronik yapılarının teorik bir değerlendirmesi verilmektedir.  $[B_nX_n]^{2-}$  kümelerinin yapısal ve elektronik karakterleri,  $[B_{12}X_{12}]^{2-}$  molekülleri ile karşılaştırılarak, süstitüent etkileri ( $X = H, F, Cl, Br, CN, BO, OH, NH_2$ ) incelendi. Bu etkiler, süstitüentlerin mezomerik ( $\pm M$ ) ve endüktif ( $\pm I$ ) etkileriyle ilişkilendirilerek tartışıldı. Sonuçlar, ikosahedral bariyerin, daha büyük kümeleri stabilize etmek yerine simetriyi azaltan ligandlar veya  $+M$  etkileri olan ligandlarla  $[B_{12}X_{12}]^{2-}$  kümesini kararsızlaştırarak azaltılabileceğini göstermektedir. İkinci bölüm, karboran kümeleri ve bunların ışık yayan sistemler üzerindeki etkileri çerçevesinde yaptığımız çalışmayı kapsamaktadır. *o*-CB-antrasin sisteminin, yerel uyarılmış (LE) ve hibritleştirilmiş yerel ve yük transferi (HLCT) karakterlerine sahip iki düşük enerjili konformasyondan görünür bölgede ışıma yaparak çift emisyon özelliği gösterdiği bilinmektedir, ancak diğer birçok CB bazlı ışık yayan sistemde de görüldüğü gibi çözücü içerisinde çok düşük emisyon kuantum verimine sahiptir. Bu bölümde, *o*-CB-Anth ve *o*-CB-Pent sistemlerinin uyarılmış durum potansiyel enerji yüzeyi (PES) detaylı olarak incelenmiş ve düşük seviyeli bir yük transfer (CT) durumunun kuantum verimi üzerindeki etkisi tartışılmıştır.

*Anahtar kelimeler: Boran dianyonlar, İkosahedral bariyer, Karboranlar, Işık yayan malzemeler, İkame türevler*

# Acknowledgements

First of all, I would like to express my deepest gratitude to my advisor Prof. Murat DURANDURDU for his helpful advice and valuable assistance throughout my doctoral study. I am eternally grateful for his endless patience, support, and encouragement.

I would like to give special thanks to my co-advisor Assist. Prof. Fahri ALKAN who involved in my Ph.D. process when I needed his guidance the most. I am most grateful for his guidance not only in my studies but also in the skills that an academic researcher should acquire during the doctoral process.

I would like to thank Prof. Andreas DREUW, who I am very happy to have had the chance to know, and who gave me the opportunity to work in his research group at Heidelberg University, Germany, for his understanding, guidance, and support.

With the same level of gratitude, I would also like to thank the members of my thesis committee throughout my research, Prof. Hakan USTA, and Prof. Serdar ÖNSES, for their valuable comments and advice.

I acknowledge the Higher Education Council (YÖK) for the financial support for my research at the University of Heidelberg, Germany, as a part of the YUDAB – International Research Scholarship Program for Ph.D. students who work in research assistant positions at universities. This dissertation was also partially supported by Abdullah Gül University Scientific Research Projects (BAP) under project number FDK-2018-122.

I would also like to thank all my colleagues who directly and indirectly help me with their support and encouragement.

Last but not the least, I want to express my sincere gratitude to my precious parents, my sister, and especially my husband and son for their great love, never-ending encouragement, and support throughout my life.

# TABLE OF CONTENTS

<b>1. INTRODUCTION .....</b>	<b>1</b>
1.1 MOTIVATION OF THE STUDY .....	1
1.2 OVERVIEW .....	2
1.3 BORON SOURCES AT A GLANCE .....	2
1.3.1 <i>A Brief Introduction to Boron Chemistry</i> .....	3
1.4 POLYHEDRAL BORON BASED STRUCTURES .....	7
1.4.1 <i>Boranes</i> .....	9
1.4.2 <i>Carboranes</i> .....	13
1.4.3 <i>Applications</i> .....	14
<b>2. THEORETICAL BACKGROUND .....</b>	<b>18</b>
2.1 QUANTUM MECHANICS / ELECTRONIC STRUCTURE .....	18
2.1.1 <i>The Electronic Problem</i> .....	18
2.1.2 <i>Variational Method</i> .....	19
2.2 HARTREE-FOCK THEORY .....	20
2.2.1 <i>Self-Consistent Field Procedure</i> .....	22
2.3 DENSITY FUNCTIONAL THEORY .....	25
2.3.1 <i>Kohn-Sham Equations</i> .....	25
2.3.2 <i>Exchange-Correlation Functionals</i> .....	27
2.3.2.1 Local Density Approximation (LDA) for $E_{xc}[\rho]$ .....	28
2.3.2.2 Generalized-Gradient Density Approximation (GGA) for $E_{xc}[\rho]$ .....	28
2.3.2.3 Hybrid Functionals .....	29
2.4 TIME-DEPENDENT DENSITY FUNCTIONAL THEORY .....	30
2.4.1 <i>Charge-Transfer (CT) Problem in TDDFT</i> .....	31
2.4.2 <i>Excited State Analysis</i> .....	32
2.5 BASIS SETS .....	34
2.6 COMPUTATIONAL PROCEDURES .....	34
2.6.1 <i>Geometry Optimization and Frequency Calculation</i> .....	34
2.7 SOLVATION METHODS .....	36
<b>3. SUBSTITUENT EFFECTS ON THE STABILITY OF BORANE DIANIONS</b> <b>.....</b>	<b>38</b>
3.1 INTRODUCTION .....	38
3.2 COMPUTATIONAL DETAILS .....	40
3.3 RESULTS AND DISCUSSION .....	42
3.3.1 <i>Geometry</i> .....	42
3.3.2 <i>Electronic Structure</i> .....	43
3.3.3 <i>Reaction Energies</i> .....	48
3.3.4 <i>Population Analysis</i> .....	53
3.4 CONCLUSIONS .....	56
<b>4. FLUORESCENCE QUENCHING IN CARBORANE-FLUOROPHORE</b> <b>SYSTEMS.....</b>	<b>58</b>
4.1 INTRODUCTION .....	58
4.2 COMPUTATIONAL DETAILS .....	60
4.3 RESULTS AND DISCUSSION .....	65
4.3.1 <i>o-CB-Ant System</i> .....	65

4.3.2	<i>Substitution Effect</i> .....	72
4.3.3	<i>Effect of the fluorophore</i> .....	77
4.4	CONCLUSIONS.....	81
5.	<b>CONCLUSIONS AND FUTURE PROSPECTS</b> .....	<b>83</b>
5.1.	CONCLUSIONS.....	83
5.2	SOCIETAL IMPACT AND CONTRIBUTION TO GLOBAL SUSTAINABILITY .....	84
5.3	FUTURE PROSPECTS .....	85



# LIST OF FIGURES

Figure 1. 1 Distribution (%) of the total B <sub>2</sub> O <sub>3</sub> reserves of the world by country.[1].....	3
Figure 1. 2 A summary of the global minima of B <sub>n</sub> <sup>-</sup> clusters (n = 3 – 25, 27) confirmed by experiment. Close-lying isomers are also shown for B <sub>25</sub> <sup>-</sup> and B <sub>27</sub> <sup>-</sup> . [29] Copyright 2015 Taylor & Francis Online .....	5
Figure 1. 3 Isoelectronic ( <i>closo</i> )-B <sub>12</sub> borane/carborane clusters.....	8
Figure 1.4 Experimentally realized borane clusters.....	9
Figure 1.5 a) Comparison of the total energy per boron vertex (E/n) results of different levels of theories. b) Cumulative BH addition energy (ΔH <sub>add</sub> ) in kcal/mol for the <i>closo</i> -borane dianions, [B <sub>n</sub> H <sub>n</sub> ] <sup>2-</sup> (n = 5-17). Reproduced from the reference [64].	11
Figure 1.6 Examples of supraicosahedral clusters in different sizes [66,71,74,77,78]. (The figure is modified from the reference [71]). Copyright 2013 Wiley .....	12
Figure 2. 1 Diagram of SCF calculation procedure .....	24
Figure 2. 2 Schematic representation of a typical valence-excited state and a CT excited state. The transition occurs from the occupied orbital <i>i</i> to the virtual orbital <i>a</i> , which are located on the same molecule in the valence-excited state and located on different molecules/fragments in the CT excited state. ....	32
Figure 3. 1 Structural representation of [B <sub>10</sub> H <sub>10</sub> ] <sup>2-</sup> , [B <sub>12</sub> H <sub>12</sub> ] <sup>2-</sup> , [B <sub>13</sub> H <sub>14</sub> ] <sup>2-</sup> , [B <sub>14</sub> H <sub>14</sub> ] <sup>2-</sup> , [B <sub>15</sub> H <sub>15</sub> ] <sup>2-</sup> and [B <sub>16</sub> H <sub>16</sub> ] <sup>2-</sup> clusters along with point group symmetries. ....	40
Figure 3.2 a) The average B-B bond lengths or (B-B) <sub>avg.</sub> (Å) for cage boron atoms in [B <sub>n</sub> X <sub>n</sub> ] <sup>2-</sup> clusters, and deviations in the (B-B) <sub>avg.</sub> for b) [B <sub>12</sub> X <sub>12</sub> ] <sup>2-</sup> and c) [B <sub>13</sub> X <sub>13</sub> ] <sup>2-</sup> with respect to different substitutions. ....	42
Figure 3.3 Deviations in (B-B) <sub>avg.</sub> length depending on the substitution for a) [B <sub>10</sub> X <sub>10</sub> ] <sup>2-</sup> , b) [B <sub>13</sub> X <sub>13</sub> ] <sup>2-</sup> , c) [B <sub>14</sub> X <sub>14</sub> ] <sup>2-</sup> , d) [B <sub>15</sub> X <sub>15</sub> ] <sup>2-</sup> and e) [B <sub>16</sub> X <sub>16</sub> ] <sup>2-</sup> clusters.....	43
Figure 3.4 HOMO-LUMO levels of (a) [B <sub>10</sub> X <sub>10</sub> ] <sup>2-</sup> , (b) [B <sub>12</sub> X <sub>12</sub> ] <sup>2-</sup> , (c) [B <sub>13</sub> X <sub>13</sub> ] <sup>2-</sup> , (d) [B <sub>14</sub> X <sub>14</sub> ] <sup>2-</sup> , (e) [B <sub>15</sub> X <sub>15</sub> ] <sup>2-</sup> and (f) [B <sub>16</sub> X <sub>16</sub> ] <sup>2-</sup> clusters calculated with PBE0/6-311++G**.....	44
Figure 3.5 a) HOMO-LUMO levels with pictorial representation of orbitals and, b) VDEs of 9, 10-substituted anthracene C <sub>14</sub> H <sub>8</sub> X <sub>2</sub> (X= H, F, Cl, Br, CN, BO, OH and NH <sub>2</sub> ) calculated with PBE0/6-311++G** .....	45
Figure 3.6 Comparison of HOMO and LUMO levels for [B <sub>12</sub> H <sub>12</sub> ] <sup>2-</sup> cluster calculated with different density functionals of varying exact exchange along with Hartree-Fock (HF) theory. ....	46
Figure 3.7 Comparison of calculated (a) VDE values and (b) H-L gaps for the clusters with different substituents using PBE0/6-311++G** level of theory. ....	48
Figure 3.8 a) Calculated relative ΔH <sub>add</sub> values for the formation of perfunctionalized boron clusters based on the reaction [B <sub>12</sub> X <sub>12</sub> ] <sup>2-</sup> + (n-12)B <sub>6</sub> X <sub>6</sub> H <sub>4</sub> → [B <sub>n</sub> X <sub>n</sub> ] <sup>2-</sup> + (n-12)B <sub>5</sub> X <sub>5</sub> H <sub>4</sub> (n=13, 14, 15 and 16), and b) calculated relative ΔH <sub>add</sub> values for the formation of single-substituted boron clusters based on the reaction [B <sub>12</sub> H <sub>11</sub> X] <sup>2-</sup> + (n-12)B <sub>6</sub> H <sub>10</sub> → [B <sub>n</sub> H <sub>n-1</sub> X] <sup>2-</sup> + (n-12)B <sub>5</sub> H <sub>9</sub> (n=13 and 14). For all substitution, ΔH <sub>add</sub> are scaled relative to the case where X=H. All values are obtained with PBE0/ 6-311++G** level of theory.....	50
Figure 3.9 Calculated relative ΔH <sub>add</sub> values for the formation of single-substituted carborene clusters based on the reaction C <sub>2</sub> B <sub>10</sub> H <sub>11</sub> X + (n-12)B <sub>6</sub> X <sub>6</sub> H <sub>4</sub> → C <sub>2</sub> B <sub>n-2</sub> H <sub>n-1</sub> X + (n-12)B <sub>5</sub> X <sub>5</sub> H <sub>4</sub> (n=13, 14). For all substitution, ΔH <sub>add</sub> are scaled relative to the case where X=H. All values are obtained with PBE0/ 6-311++G** level of theory. ....	53
Figure 3.10 Schematic representation of the NPA charge distribution in the dianions in terms of an inner core (B <sub>10</sub> /B <sub>12</sub> /B <sub>13</sub> /B <sub>14</sub> /B <sub>15</sub> /B <sub>16</sub> ) and an outer shell	

(X <sub>10</sub> /X <sub>12</sub> /X <sub>13</sub> /X <sub>14</sub> X <sub>15</sub> /X <sub>16</sub> ). The same charge distribution with CHELPG method is illustrated in Figure 3.11.....	54
Figure 3.11 Schematic representation of the ESP (CHELPG) charge distribution the dianions in terms of an inner core (B <sub>10</sub> /B <sub>12</sub> /B <sub>13</sub> /B <sub>14</sub> /B <sub>15</sub> /B <sub>16</sub> ) and an outer shell (X <sub>10</sub> /X <sub>12</sub> /X <sub>13</sub> /X <sub>14</sub> /X <sub>15</sub> /X <sub>16</sub> ).....	55
Figure 4. 1 The illustration of important geometric parameters for excited-state geometries of <i>o</i> -CB-Ant along with numbering of C atoms used in the text. ....	61
Figure 4. 2 Heat maps of transition density matrix (TDM) graphs for S <sub>1</sub> states of a) LE b) HLCT and c) CT states calculated with different XC functionals.....	65
Figure 4. 3 Relative energies of the frontier levels for <i>o</i> -CB and Ant moieties with respect to C <sub>1</sub> -C <sub>2</sub> distance on <i>o</i> -CB. ....	66
Figure 4. 4 Illustration of the absorption and potential emission paths along with the corresponding geometries of the <i>o</i> -CB-Ant system. Transition energies ( <b>E0</b> → <b>1/E1</b> → <b>0</b> ) and the oscillator strengths ( <b>f</b> ) are shown for each process. Adiabatic S <sub>1</sub> state energies ( <b>ES1</b> ) were calculated by the addition of <b>E0</b> → <b>1/E1</b> → <b>0</b> for the absorption and emissive/non-emissive processes to the ground state energies ( $\Delta E_0$ ) at corresponding geometric conformations. These three conformations correspond to the minimum energy points on the excited state (S <sub>1</sub> ) potential energy surface. % contribution of anthracene and <i>o</i> -CB based orbitals to HOMO and LUMO for each transition are shown on the orbital pictures. ....	67
Figure 4. 5 (a-c) Potential energy surfaces (PESs) for the adiabatic excited-state energies (E <sub>S1</sub> ) with respect to $\varphi$ at fixed C <sub>1</sub> -C <sub>2</sub> bond lengths, (d-f) heat maps of transition density matrix (TDM) graphs for selective S <sub>1</sub> states calculated with M06-2X/6-31G*( $\Delta r$ and $\Lambda$ indexes are given in Table 4.4), and (g-i) calculated oscillator strengths for the corresponding S <sub>1</sub> → S <sub>0</sub> transitions. Frontier orbital pictures are also given for some specific conformations on PES diagrams to show the excited state character change. Atom numbering for the TDM plots is given in Figure 4.6.....	68
Figure 4. 6 Atomic labels for the heat maps of TDM (H atoms are not given in the heat maps). <i>o</i> -CB atoms are numbered as 1-12 (left and down in TDM plots) whereas <i>Ant</i> atoms are numbered as 13-26. (right and up in TDM plots).....	69
Figure 4. 7 (a-c) Potential energy surfaces (PESs) for the adiabatic excited-state energies (E <sub>S1</sub> ) with respect to C <sub>1</sub> -C <sub>2</sub> bond lengths at fixed $\varphi$ , (d-f) TDMs for selective S <sub>1</sub> states ( $\Delta r$ and $\Lambda$ indexes are given in Table 4.5), and (g-i) calculated oscillator strengths for the corresponding S <sub>1</sub> → S <sub>0</sub> transitions. Atom numbering for the TDM plots are given in Figure 4.6. ....	71
Figure 4. 8 Positions of substituents for <i>o</i> -CB-Ant derivatives (X: F, Cl, CN and OH).72	
Figure 4. 9 Potential energy diagrams for the rotation at fixed C <sub>1</sub> -C <sub>2</sub> bond lengths of a) HLCT state and b) CT state for the C-substituted derivatives of the <i>o</i> -CB-Ant dyad with their corresponding oscillator strengths (c-d).....	75
Figure 4. 10 Potential energy surfaces with respect to $\varphi$ for partially stretched and fixed C <sub>1</sub> -C <sub>2</sub> bond lengths for the B-substituted derivatives of the <i>o</i> -CB-Ant. For these surfaces, $\varphi = -90^\circ$ corresponds to the HLCT state for each system. ....	76
Figure 4. 11 Potential energy surfaces with respect to $\varphi$ for fully stretched and fixed C <sub>1</sub> -C <sub>2</sub> bond lengths for the B-substituted derivatives of the <i>o</i> -CB-Ant. For these surfaces, $\varphi = 0^\circ$ corresponds to the CT state for each system. ....	77
Figure 4. 12 Illustration of the absorption and potential emission paths along with the corresponding geometries of the <i>o</i> -CB- <i>Pnt</i> system. The conformations for LE and CT states correspond to the minimum energy points on the S <sub>1</sub> potential energy surface, while the HLCT state is obtained with excited-state geometry optimization with constrains (C <sub>1</sub> -C <sub>2</sub> = 2.25 Å and $\varphi = -87^\circ$ ). % contribution of pentacene and <i>o</i> -	



<i>CB</i> based orbitals to HOMO and LUMO for each transition are shown on the orbital pictures.....	78
Figure 4. 13 Relative energies of the frontier levels for <i>o</i> -CB and Pent moieties with respect to C <sub>1</sub> -C <sub>2</sub> distance on <i>o</i> -CB. ....	79
Figure 4. 14 Potential energy surfaces (PESs) for the adiabatic excited-state energies (E <sub>S1</sub> ) with respect to $\varphi$ at fixed C <sub>1</sub> -C <sub>2</sub> bond lengths, (a-c) and calculated oscillator strengths for the corresponding S <sub>1</sub> → S <sub>0</sub> (d-f). The same PESs (g-i) and oscillator strengths (j-l) are given with respect to C <sub>1</sub> -C <sub>2</sub> bond lengths at fixed $\varphi$ as well. ....	81



# LIST OF TABLES

Table 1. 1 Classification of Boron Hydrides according to Wade's Rule.....	8
Table 3. 1 Vertical detachment energies (VDEs) in eV calculated at different levels of theory for $[B_{12}X_{12}]^{2-}$ (The values in the parenthesis are VDE values with Zero Point Energy (ZPE) correction).....	47
Table 3.2 Adiabatic detachment energies (ADEs) in eV calculated at different levels of theory for $[B_{12}X_{12}]^{2-}$ (The values in the parenthesis are ADE values with ZPE correction).....	47
Table 3.3 Calculated formation enthalpies ( $\Delta H_{\text{add}}$ ) <sup>*</sup> of perfunctionalized borane clusters, $[B_nX_n]^{2-}$ , from icosahedral $[B_{12}X_{12}]^{2-}$ with different level of theories.....	49
Table 3.4 Calculated formation enthalpies ( $\Delta H_{\text{add}}$ ) <sup>*</sup> of $[B_nH_{n-1}X]^{2-}$ clusters from icosahedral $[B_{12}H_{11}X]^{2-}$ .....	52
Table 3.5 Calculated formation enthalpies ( $\Delta H_{\text{add}}$ ) <sup>*</sup> of $[C_2B_{n-1}H_{n-2}X]^{2-}$ clusters from icosahedral $[C_2B_{10}H_{11}X]^{2-}$ using PBE0 .....	52
Table 4. 1 Benchmark results for the emission and absorption energies in eV (emission wavelengths in parenthesis) for different XC-functionals from the three different conformers in comparison with the experimental results. ....	62
Table 4. 2 Pictorial frontier orbitals of the three conformations for $S_1$ state along with the orbital contributions from <i>o</i> -CB and <i>Ant</i> moieties calculated with different XC functionals.....	63
Table 4. 3 $\Delta r$ and $\Lambda$ values for the excited states of <i>o</i> -CB- <i>Ant</i> system with different XC functionals.....	63
Table 4. 4 $\Delta r$ and $\Lambda$ values for the TDMs given in Figure 4.5 for selective $S_1 \rightarrow S_0$ transitions on the PESs with respect to $\varphi$ at fixed $C_1$ - $C_2$ bond lengths. ....	69
Table 4. 5 $\Delta r$ and $\Lambda$ values for the TDMs given in Figure 4.7 for selective $S_1 \rightarrow S_0$ transitions on the PESs with respect to $C_1$ - $C_2$ bond lengths at fixed $\varphi$ . ....	71
Table 4. 6 Transition energies ( $E_{0 \rightarrow 1}$ or $E_{1 \rightarrow 0}$ ), oscillator strengths ( $f$ ), adiabatic $S_1$ state energies ( $E_{S_1}$ ), $C_1$ - $C_2$ lengths and dihedral angles ( $\varphi$ ) for ground state and three main $S_1$ state conformations of <i>o</i> -CB- <i>Ant</i> . (Energies are given in eV.) .....	73

# LIST OF ABBREVIATIONS

ADE	Adiabatic Detachment Energy
AdNDP	Adaptive Natural Density Partitioning
AIE	Aggregation Induced Emission
BNCT	Boron Neutron Capture Therapy
CB	Carborane
CCSD	Coupled Cluster Singles and Doubles
CI	Configuration Interaction
CT	Charge Transfer
DFT	Density Functional Theory
GGA	Generalized-Gradient Density Approximation
GTO	Gaussian-type Orbital
HF	Hartree Fock
HK	Hohenberg-Kohn
HLCT	Hybridized Local and Charge Transfer
HOMO	Highest Occupied Molecular Orbital
ICT	Intramolecular Charge Transfer
IEFPCM	Integral Formalism Variant of the Polarizable Continuum Model
KS	Kohn-Sham
LCAO	Linear Combination of Atomic Orbitals
LDA	Local Density Approximation
LE	Locally-excited
LED	Light Emitting Diode
LUMO	Lowest Unoccupied Molecular Orbital
MEP	Molecular Electrostatic Potential
MO	Molecular Orbital
MP	Møller–Plesset
NBO	Natural Bonding Orbital
NPA	Natural Population Analysis
PCM	Polarizable Continuum Model
PES	Potential Energy Surface

SCF	Self-Consistent Field
STO	Slater-type Orbital
TDDFT	Time-Dependent Density Functional Theory
TDM	Transition Density Matrix
TICT	Twisted Intramolecular Charge Transfer
TMS	Tetramethylsilyl
VDE	Vertical Detachment Energy





*To my family*

# Chapter 1

## Introduction

### 1.1 Motivation of the Study

For a few decades, the focus of the experimental and theoretical studies on various boron-based clusters such as bare boron clusters, boranes, carboranes, metallaboranes, etc., have been to identify stable and low-energy conformations while exploring their electronic and chemical properties for potential applications. Among the boron-based molecules, polyhedral boranes and carboranes have drawn significant attention for the development of new generation materials exhibiting sterling qualities such as structural durability, functional electrical and magnetic properties, etc. The polyhedral boron chemistry has been dominated by the icosahedral clusters of borane dianions, carboranes, and their metal incorporated derivatives due to their highly stable structures. Although theoretical studies suggest the possibility of larger borane hydrides beyond the icosahedral dianion, the obstacle to their isolation has not been overcome yet. The synthesis of supraicosahedral geometries was succeeded only by the inclusion of carbon (carboranes) or metal atoms (metallaboranes) in the skeletal cage structure. In Chapter 3, the stability of boron hydride and derivative dianions of different sizes were compared, and the effects of functionalization on the barrier and the possibility of the isolation of larger dianions were discussed.

An important application of boron-based systems is the development of next-generation luminescent materials with tunable properties. In that regard, tunability of the light-emitting materials within the carborane-fluorophore architecture appears as an exciting research area. In our study, we provide a new physical insight for the underlying mechanism of low emission efficiency for carborane-fluorophore systems in the solution state and to demonstrate the effects of some molecular modifications on their photophysical characteristics in our study presented in Chapter 4.

Although the high number of studies on these fields reveals many extraordinary properties of boron, resulting from its electron-deficient nature, boron chemistry is relatively new to carbon chemistry and still has many unexplored features. Therefore, there are still broad applications and inherent properties to be discovered for these materials.

## 1.2 Overview

This dissertation is organized as follows:

The first chapter briefly introduces the boron chemistry which mainly arises from the electron-deficient nature of boron element. In this chapter, molecular structures and bonding motifs formed by boron elements, their properties, and the historical development of boron chemistry are covered. Special attention will be paid to the polyhedral borane and carborane clusters.

The second chapter provides theoretical quantum chemistry concepts, covering general information about density functional theory (DFT) and time-dependent density functional theory (TDDFT).

Chapter 3 describes our work on the substituent effects on the electronic structures and stability of different sized borane dianion clusters. The effect of functionalization on the icosahedral barrier for the realization of larger clusters is also discussed.

In chapter 4, the excited state characters are investigated for the o-carborane-anthracene system, and the origins of its low quantum yield in solution are addressed.

Finally, in chapter five, the main conclusions of this dissertation are provided with a brief summary and a few concluding remarks for further developments are mentioned.

## 1.3 Boron Sources at a Glance

Boron is commonly found in earth, rocks, and water. Due to its high chemical affinity for other elements, it is not found as a free element in nature, but in the form of minerals, especially as borates and borosilicates. High concentrations of boron deposits in economic size, commonly as oxide compounds, are mostly found in arid, high volcanic and geothermal regions of Turkey and the USA. Figure 1.1 presents that the important boron deposits in the world with approximately 73% of the total reserve are found in

Turkey, and this is followed by Russia and the United States with 7.7% and 6.2%, respectively[1].

Although boron salts have been used for hundreds of years to serve many purposes, the mystery over its unique chemistry has continued until the middle of the 20<sup>th</sup> century. Boron products are currently used in domestic requirements such as glass, cleaning-detergent, agriculture, adhesive, etc. However, the recently uncovered features of boron bring a potential for its use in wider and more advanced technologies, and it is of great importance for Turkey to know the boron in detail and to research its applications in all aspects.

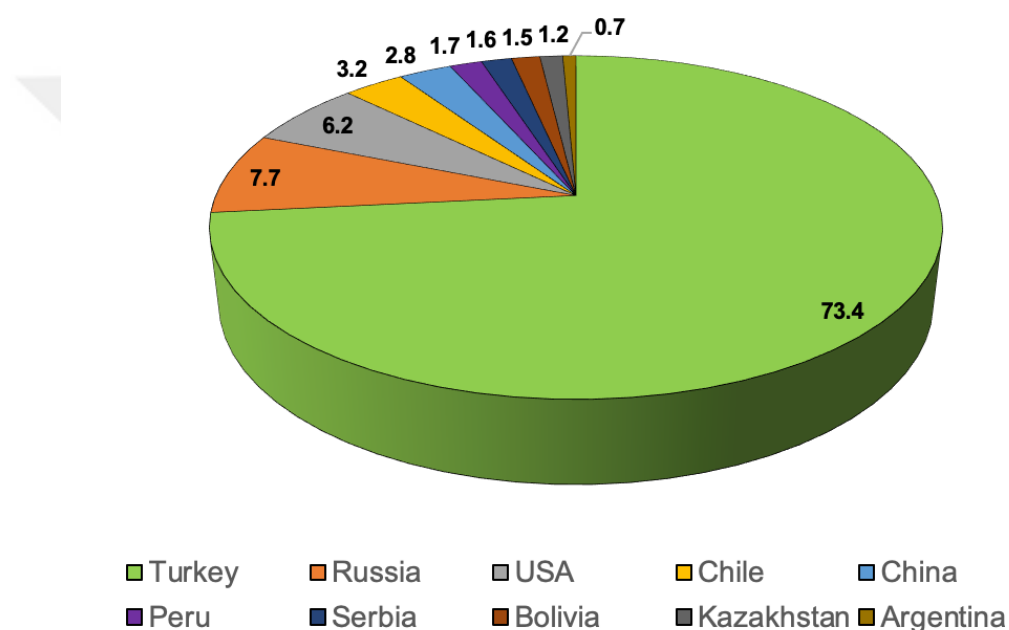


**Figure 1. 1** Distribution (%) of the total B<sub>2</sub>O<sub>3</sub> reserves of the world by country.[1]

### 1.3.1 A Brief Introduction to Boron Chemistry

Carbon element has a very special place in chemistry due to its ability to form molecules of unlimited types in various sizes by covalent bonding. Its compounds are built by these conventional covalent bonds, leading to chain-like structures and rigid rings. Despite lying next to carbon in periodic table, bonding nature and ability of boron-containing systems is still an active research area, particularly in cluster chemistry. Moreover, the way of forming compounds of boron is not always as clear and straightforward as that of carbon, and boron rich systems presents electronic and structural complexity.



Boron element, a metalloid, is the lightest member of the IIIA group in the periodic table. Its electron deficient nature is the main reason behind its two-face chemistry. Two-face chemistry is used to refer to its ability to make both classical 2-center-2-electron (2c-2e)  $\sigma$ -bonds, similar to those of the neighboring carbon element (e.g.,  $\text{BH}_4^-$ , the analog of  $\text{CH}_4$  molecule) and multicenter bonding. It is the latter that we are going to address in the scope of this thesis.

Since boranes do not naturally exist, the discovery of their unusual features had to wait for the synthesis of the first borane molecules. After the first report of a diborane structure with a gas-phase electron diffraction analysis in 1937[2], a bridging hydrogen and triangle BHB motifs were observed for many other borane molecules as well. The unusual 3-center-2-electron (3c-2e) bond model was formulated by W. N. Lipscomb to explain these structures, which was a revolution for the theory of chemical bonding, resulting in the award of a Nobel Prize in 1976 for his studies on the structure of boranes illuminating problems of chemical bonding [3–5].

Owing to its electron-deficient nature, boron-based molecules exhibit a structural complexity resulting in hypercoordination. In elemental boron clusters, the molecular structures vary according to the varying number of boron atoms. Although the systematic attempt to understand the structures of bare boron clusters with computational methods dates back to the early 1990s[6,7], the first experimental data were obtained in 2002 by Wang et. al with the observation of  $\text{B}_5$  and  $\text{B}_5^-$  clusters[8]. Since then, the structure of size-selected clusters and the nature of their chemical bonding have been investigated by photoelectron spectroscopy in combination with theoretical calculations[9–28]. Photoelectron spectroscopy, being a powerful technique in analyzing the electronic structure of matters, allows us to investigate the nature of the chemical bonding of the molecules by using ultraviolet (UV) or visible light sources. From a structural point of view, all these studies revealed that the energetically favorable small elemental boron clusters exist in a planar/quasi planar orientation consisting of triangular lattices. A general structural trend for anionic bare boron clusters is shown in Figure 1.2.

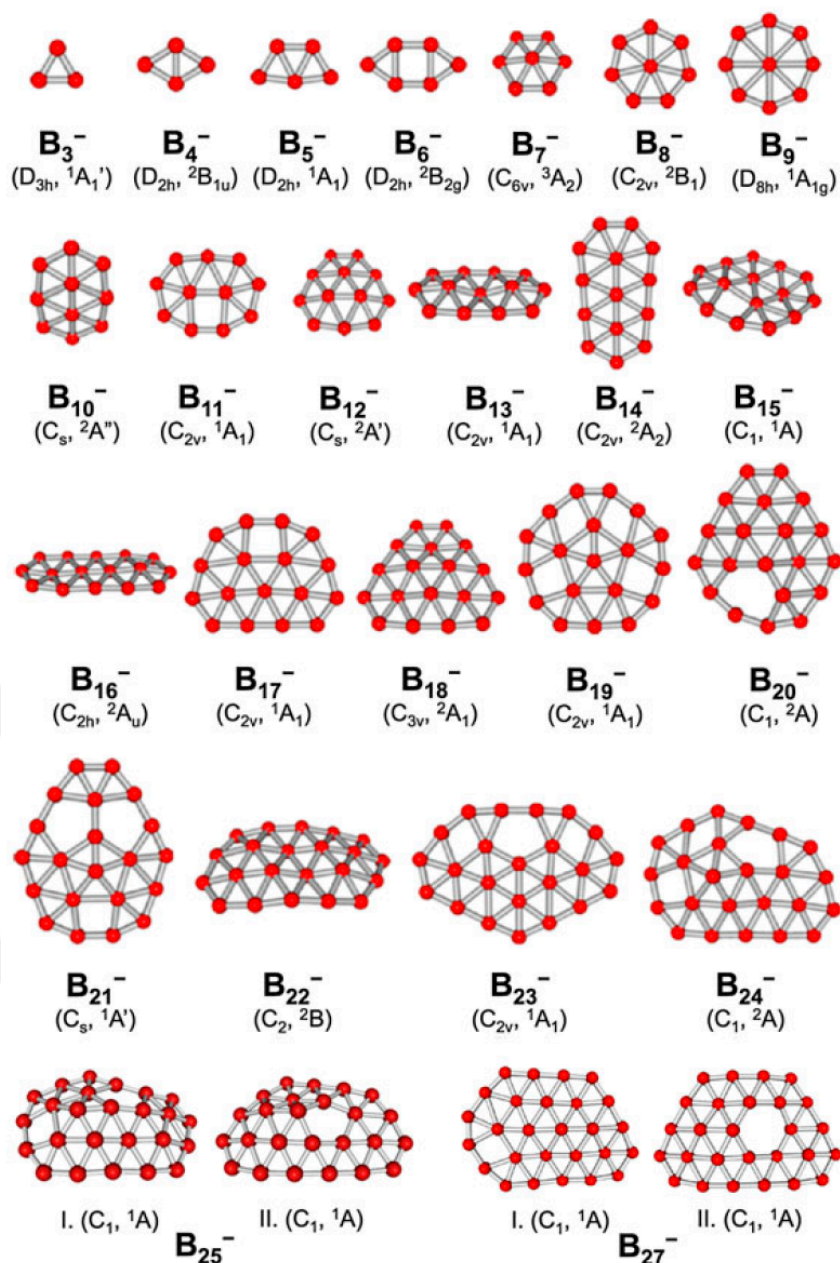


**Figure 1. 2** A summary of the global minima of  $B_n^-$  clusters ( $n = 3 - 25, 27$ ) confirmed by experiment. Close-lying isomers are also shown for  $B_{25}^-$  and  $B_{27}^-$ . [29] Copyright 2015 Taylor & Francis Online

Experimental results supported by computational simulations show that elemental boron clusters exhibit a  $2D \rightarrow 3D$  transition after a critical size of  $B_{20}$  [14,30]; thus, the first tubular type boron cluster, which can be considered as a seed for boron nanotubes, was observed. On the other hand, it has been computationally shown that the transition to 3D structure occurs earlier in cationic clusters ( $B_{16}^+$ ) [17,31], most likely due to the electron loss from already electron-deficient structure, which forces the molecular pattern to fold

closer. In the case of anionic boron clusters, this transition takes place at a much larger size; the clusters up to 30 atoms were shown by the experimental and computational works that the planar/quasi-planar structures are still at the global minimum[28].

Due to its electron deficiency, all-boron clusters tend to be somehow curved; and unlike neighboring carbon, they cannot form sheet-like structures built up by honey-comb lattices such as graphene. However, for large boron clusters with a planar orientation, which are called borophenes, stability is provided with one or more hexagonal spaces through the triangular pattern[26–28]. The highly stable planar  $B_{36}$  cluster, reported by Piazza et al.[32], and subsequently  $B_{35}$  cluster, reported by Li et al.[33], are important in showing that all-boron sheets (borophenes) with hexagonal vacancies are potentially viable. After these studies, new members of the borophene family have also been added to the literature[34–36].

Given the similarities between carbon-based molecules, it would not be surprising to expect boron clusters to form structures similar to fullerenes. Although studies on these clusters, which are called borospherenes, progress generally on a theoretical basis, the first all-boron fullerene-like cage cluster  $B_{40}$  was observed experimentally by Zhai et. al in 2014[37]. Chemical bonding analysis revealed the  $\sigma$  and  $\pi$  delocalized bonds through  $B_{40}$  borospherene, but unlike  $C_{60}$  fullerene, the cluster was found to possess heptagonal faces on its surface. It has been shown by preliminary studies that this cluster has an important potential to be used for hydrogen storage. Further computational investigations resulted in different medium size stable boron clusters, especially  $B_{80}$ , being reported as well[16,38].

The stable structure of boron clusters can be summarized with the principle put forward by Boustani and Quandt. According to this principle, which is formulated based on the structural similarities of boron clusters, pentagonal pyramid  $B_6$  (e.g., in  $B_{12}$ ) and the hexagonal pyramid  $B_7$  (e.g., convex and quasi-planar structures) are the two basic units constructing the most stable clusters[39]. The chemical bonding properties behind the ability of boron clusters to form such diverse structures is an intriguing topic. Having both localized and delocalized bonds along with the multicenter bonding as a result of boron's electron deficiency somewhat limits the use of the traditional molecular orbital (MO) approach for deciphering the chemical bonding of boron clusters, especially for the large systems exhibiting low-symmetry[29]. The most chemically intuitive pictures of electronic structure and chemical bonds for boron clusters are provided within the AdNDP formalism, which was developed by Zubarev and Boldyrev[40,41]. AdNDP is

the acronym for “Adaptive Natural Density Partitioning” and is a generalization of the Natural Bonding Orbital Analysis (NBO). Since the electronic structure is represented in terms of  $nc-2e$  bonds, which enables obtaining of both Lewis bonding elements (core electrons, lone pairs, and  $2c-2e$  bonds) and delocalized bonding elements, AdNDP has become a useful tool for the investigation of the bonding patterns in boron-based clusters. According to the studies, all 2D boron clusters are constructed by  $2c-2e$   $\sigma$  bonds between the periphery atoms while delocalized  $\sigma$  and  $\pi$  bonds are formed by the interior atoms, providing the system aromaticity or antiaromaticity. Similarities observed in the structures of carbon and boron-based molecules also emerge in their electronic structures and many 2D hydrocarbon analogues of boron clusters with similar aromaticity and antiaromaticity have been reported[11,20–25,28].

## 1.4 Polyhedral Boron Based Structures

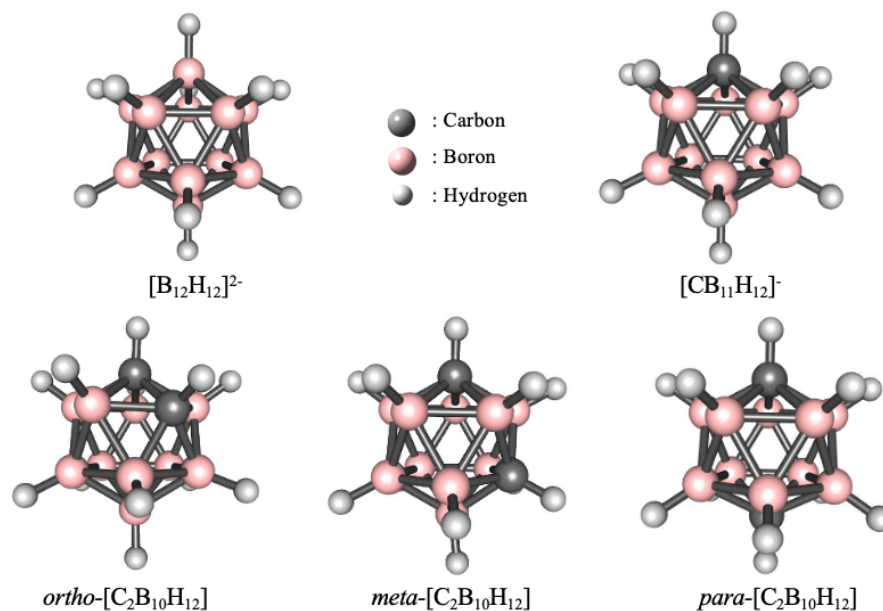
Polyhedral clusters containing only boron atoms or in combination with other elements have been drawing quite an attention due to their different bonding characteristic from our understanding of covalent bonding. Boron-based polyhedral clusters include highly reactive borane clusters as well as boranes with high thermal, chemical and electrochemical stability. Within the scope of this thesis, our focus is on the latter.

The relationship between the number of electron pairs participating in the skeletal structure of carboranes, boranes, and higher boranes is expressed by Wade in his article published in 1971[42], and it was developed as a method for the prediction of the cluster shapes. While boron hydrides can be classified as *closo*, *nido*, and *arachno* for cages with  $(n+1)$ ,  $(n+2)$ , and  $(n+3)$  electron pairs, respectively, the clusters with fewer than  $(n+1)$  pairs are called *hypercloso* cages. The last one generally involves metallaboranes/metallacarboranes and boron halides ( $B_nX_n$ ), where the cages are stabilized by metals in the skeletal structure, and the electron density donation to the cage by exo halides, respectively. The application of this relation was then extended by Wade[43] to a wide range of other compounds, such as metal clusters, metal-hydrocarbon complexes, and some hydrocarbons. Wade’s rule was later modified by Mingos with its applications to the main group and transition metal polyhedral structures[44].

**Table 1. 1** Classification of Boron Hydrides according to Wade's Rule

Type	Formula	Skeletal Electron Pairs
Closo	$[\text{B}_n\text{H}_n]^{2-}$	$n+1$
Nido	$\text{B}_n\text{H}_{n+4}$	$n+2$
Arachno	$\text{B}_n\text{H}_{n+6}$	$n+3$

Polyhedral boron chemistry is dominated by *icosahedral* borate dianions, carboranes, metallaboranes, and metallacarboranes due to their high stabilities. Highly symmetric  $\text{B}_{12}$  icosahedra appear to be the building block for various crystalline phases of bulk boron structures[39,45], and is the common unit of the most stable three-dimensional boron-based molecules, including the allotropes of elemental boron, boron-rich solids and the parent anion of the polyhedral boranes; however, it is not stable alone and collapses without a support of a bulk lattice.

**Figure 1. 3** Isoelectronic (*closo*)- $\text{B}_{12}$  borane/carborane clusters

The main icosahedral boron-based clusters are shown in Figure 1.3. Monocarbapcloso-dodecaborane (-) ( $[\text{CB}_{11}\text{H}_{12}]^-$ ), and dicarbapcloso-dodecaborane ( $\text{C}_2\text{B}_{10}\text{H}_{12}$ ) are the isoelectronic derivatives of  $[\text{B}_{12}\text{H}_{12}]^{2-}$  cluster. In all these isoelectronic clusters, the cage atoms are connected with 13 pairs of valence electrons with a delocalized bonding, which serve as examples of electron deficient systems. The chemical inertness of these delocalized bonds and the unique physical and chemical properties of the clusters make them valuable for a wide variety of research and application fields such as medicine, catalyst studies, non-linear optics, coordination chemistry, etc.[46–48] In the following

sections, the general features of these clusters and their importance are explained. Synthesis methods are not given since their non-relevance to the scope of this thesis.

### 1.4.1 Boranes

Before the discovery of *closo*-boranes, *nido* and *arachno*-boranes were known; however, among these different types of boron hydrides (see Table 1.1) *closo*-boranes have been drawn particular attention due to their special electronic structure and coordination environment. A series of parent *closo*-borane dianions ( $[\text{B}_n\text{H}_n]^{2-}$ ,  $n = 5-9, 11, 12$ )[49–52] were synthesized after the first isolation of  $[\text{B}_{10}\text{H}_{10}]^{2-}$  in 1959[5], and their geometries are shown in Figure 1.4. The electronic stability of these dianions is provided by the stabilization of extra electrons in a  $\sigma$ -delocalized electronic environment.

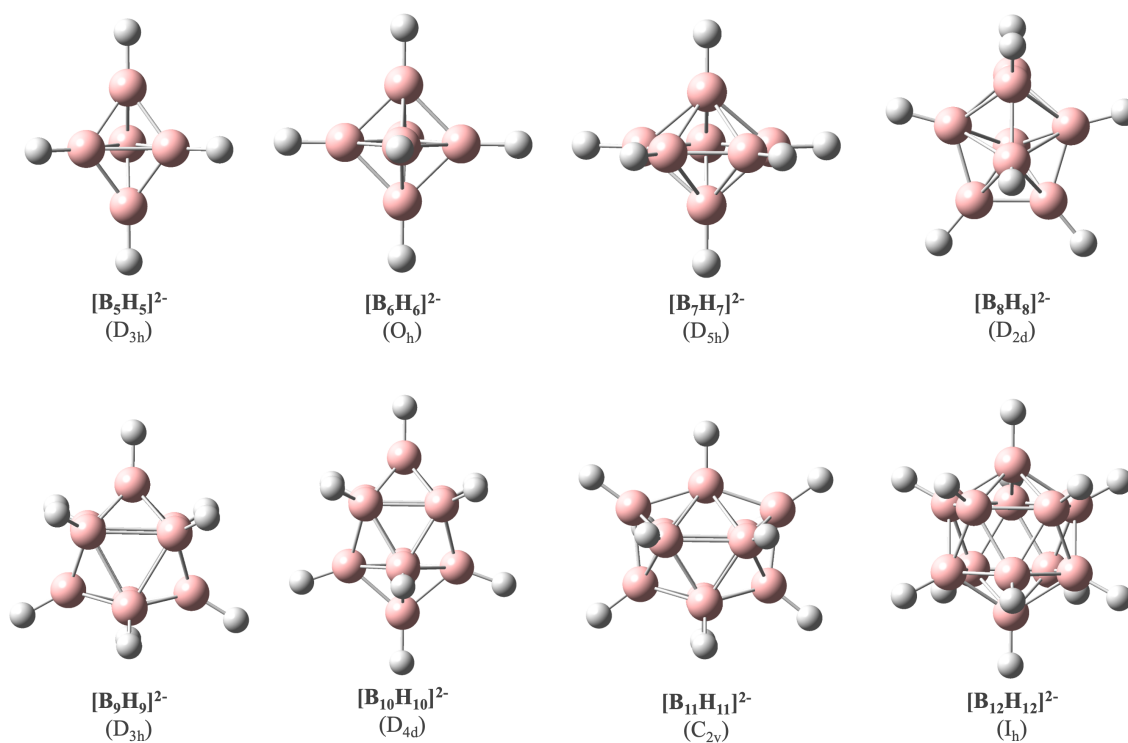


**Figure 1.4** Experimentally realized borane clusters

The *closo*-dodecaborane dianion,  $[\text{B}_{12}\text{H}_{12}]^{2-}$ , has a key place in boron chemistry, owing to its impressive icosahedral structure and thermodynamic stability. The electronic structure and stability of  $[\text{B}_{12}\text{H}_{12}]^{2-}$  have been the subject of many theoretical studies. [53,54] The first experimental gas phase measurements on its electronic stability using photoelectron spectroscopy were reported by Aprà et al. in 2019, which enables an experimental benchmark for comparison with high-level theories.[55] The presented

results in the study are important in confirming the high accuracy of the data produced by the CCSD (T) method and suggesting a reasonable, cost-effective DFT alternative (PBE0) for the dianion system.

Substitution is a useful way to provide different functions to the cluster. For the functionalization of borane dianion the synthesis of per-hydroxylated parent borane ( $[\text{B}_{12}(\text{OH})_{12}]^{2-}$ ) and per-B-hydroxylated icosahedral carborane derivatives (1,12- $\text{H}_2\text{-C}_2\text{B}_{10}(\text{OH})_{10}$ ) can be given as examples, which were achieved by Hawthorne et al.[56] Then  $[\text{B}_{12}(\text{OH})_{12}]^{2-}$  could be converted into ester functions resulting in a complete organoderivatization of the icosahedral surface.[57] Halogenated borane dianions are other examples of the icosahedral borane derivatives.[58–61] However, the fact that  $[\text{B}_{12}\text{H}_{12}]^{2-}$  cluster does not have a specific reaction center due to its highly symmetrical structure makes its functionalization difficult.

Exploring the lower borane series prompted chemists to search for the larger borane dianions beyond  $[\text{B}_{12}\text{H}_{12}]^{2-}$ , which are called supraicosahedral clusters. Despite the intensive experimental effort for the synthesis of larger parent borane dianions,  $[\text{B}_n\text{H}_n]^{2-}$  ( $n > 12$ ), they, unfortunately, could not be realized yet. The synthesis of a larger borane,  $[\text{B}_{19}\text{H}_{20}]^-$ , has been reported by Gaines et al.[62], however, this molecule was found to exhibit a structure in the form of appended *nido* cages rather than an expanded *closo* cage. At this point, theoretical investigations are of great importance to investigate the reason behind this failure and to suggest new alternative synthetic ways if possible. All the computational studies on the investigation of larger borane dianions indicate a barrier to supraicosahedral clusters, which is called icosahedral barrier. To determine the relative stabilities of a set of hypothetical *closo*-boranes  $[\text{B}_n\text{H}_n]^{2-}$  ( $n = 9\text{-}24$ ), Lipscomb and co-workers used the average energy per BH unit ( $E/n$ ) as a criterion. In addition, the degree of sphericity was also considered an important parameter for high stability.[63] Their results were encouraging as some of the larger clusters such as  $[\text{B}_{14}\text{H}_{14}]^{2-}$  and  $[\text{B}_{17}\text{H}_{17}]^{2-}$ , were found more stable than experimentally available  $[\text{B}_9\text{H}_9]^{2-}$ ,  $[\text{B}_{11}\text{H}_{11}]^{2-}$  and even  $[\text{B}_{10}\text{H}_{10}]^{2-}$ . The stability of larger boranes beyond the icosahedral dianion ( $n = 13\text{-}17$ ) were also evaluated by Schleyer and co-workers[64] according to various parameters such as 3D aromaticity and B-B bond length range size in addition to the energy criteria by taking the highly symmetric  $[\text{B}_{12}\text{H}_{12}]^{2-}$  and  $[\text{B}_6\text{H}_6]^{2-}$  as references for the quantitative comparison. Due to the inadequacy of the stability assessment by using average energies per vertex ( $E/n$ ), which does not take the fractional variation of the extra electrons through the cluster size, cumulative BH addition energy ( $\Delta H_{\text{add}}$ ) was also considered as a criterion

in their paper. The comparison of the energy-based results is presented in Figure 1.4. Both graphs show a clear decline in the energy values with increasing cluster size up to 12 vertices. The sudden rise in the transition from the size of 12 to 13 indicates that this step is not energetically favorable, that is, a barrier. After 13 vertices, a decreasing curve appears again. While  $[\text{B}_{12}\text{H}_{12}]^{2-}$  is the most stable dianion according to  $E/n$  results,  $[\text{B}_{16}\text{H}_{16}]^{2-}$  and  $[\text{B}_{17}\text{H}_{17}]^{2-}$  were found to be more favorable when  $\Delta H_{\text{add}}$  was taken into account, which suggests that energetically unfavorable steps may be the reason behind the failure of the larger dianions to be isolated.

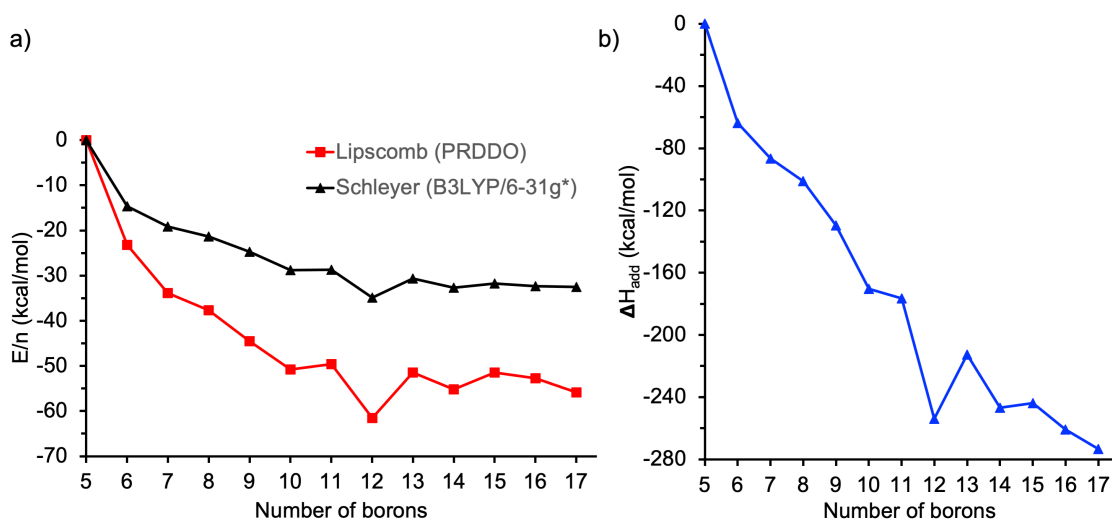


**Figure 1.5** a) Comparison of the total energy per boron vertex ( $E/n$ ) results of different levels of theories. b) Cumulative BH addition energy ( $\Delta H_{\text{add}}$ ) in kcal/mol for the *closo*-borane dianions,  $[\text{B}_n\text{H}_n]^{2-}$  ( $n = 5-17$ ). Reproduced from the reference [64].

On the other hand, Muetterties et al.[50] approached this issue in terms of coordination number. They stated that maximization of the number of nearest-neighbor contacts up to some limit is an advantage for stability, however, there should be a limit here since the increase in the coordination number results in a sterically crowded structure, which reduces the stability. The icosahedral  $[\text{B}_{12}\text{H}_{12}]^{2-}$  cluster is built up of six-coordinated B atoms (including B-H sides), which provides the dianion highly symmetrical and nearly spherical structure; that being said, this coordination number may not be an upper limit since there are examples of seven- and eight-coordinated boron atoms.[65] The electron-deficient nature of boron atoms may be insufficient to provide the number of coordination required for supraicosahedral borane dianions.

It should be noted that the icosahedral barrier can be overcome with the insertion of metal or C atoms to the cluster. The first isolation of a supraicosahedral boron-based cluster was achieved as a 13-vertex carborane in 2003[66], which is followed by other



successful synthesis and characterization of several supraicosahedral clusters in the form of metallaboranes, carboranes and metallocarboranes consisting of 13-16 vertices.[67–76] Some examples to those clusters are presented in Figure 1.6.

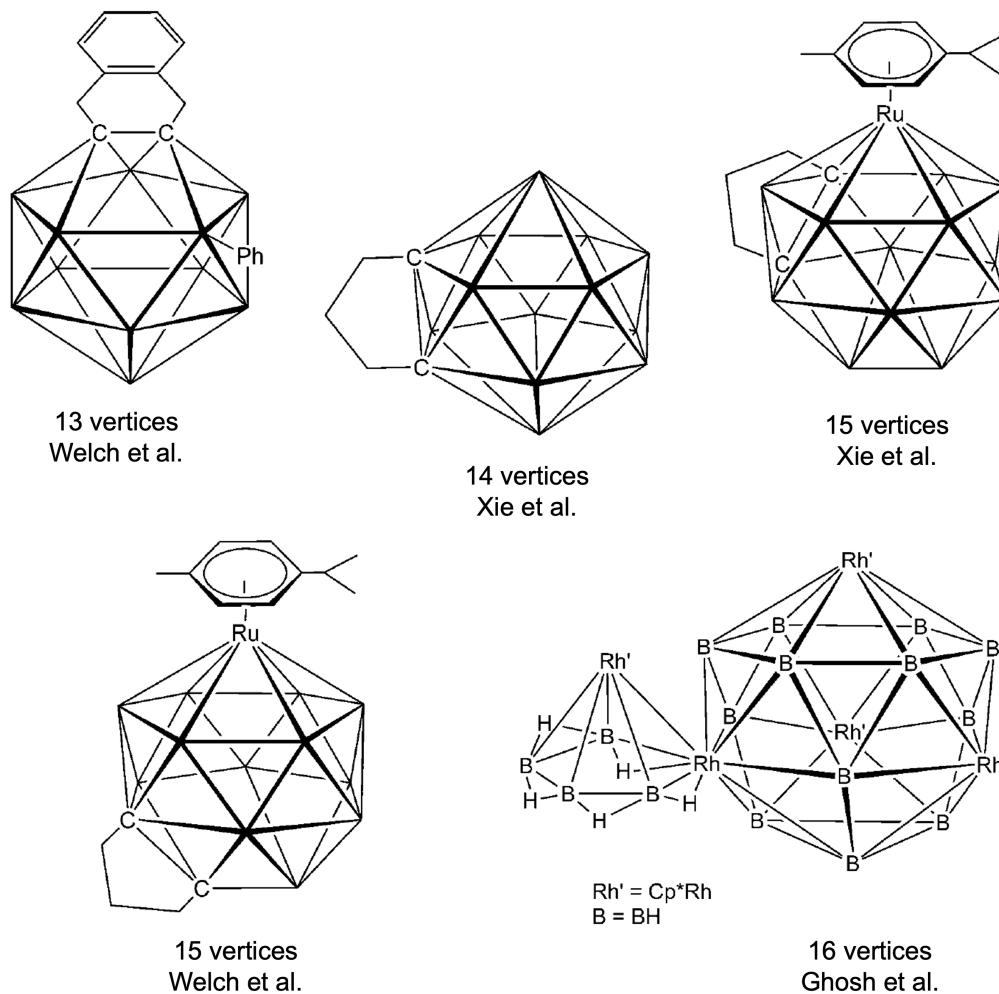


**Figure 1.6** Examples of supraicosahedral clusters in different sizes [66,71,74,77,78]. (The figure is modified from the reference [71]). Copyright 2013 Wiley

Boron chemistry continues to evolve in a similar way to carbon chemistry with ongoing discoveries and functionalization of the *closo*-borane family. The perfect icosahedron *closo*-dodecaborane,  $[B_{12}H_{12}]^{2-}$  with its very stable physical and chemical properties, 3D aromaticity, and easy-to-modify B-H bonds, is the focus of interest in a wide range of research fields, which are given in section 1.4.3. Although the derivatives of boron clusters have been successfully prepared, the expensive preparation methods necessitate the development of safer, simpler, and low-cost synthesis methods.[79]

## 1.4.2 Carboranes

Isoelectronic substitution of one or two B-H vertices in  $[\text{B}_{12}\text{H}_{12}]^{2-}$  by C-H leads to the formation of the aromatic derivatives  $[\text{CB}_{11}\text{H}_{12}]^-$  anion and  $[\text{C}_2\text{B}_{10}\text{H}_{12}]$  isomers and brings the cluster further stability.

Monocarba-closo-dodecaborane(-),  $[\text{CB}_{11}\text{H}_{12}]^-$ , has a high resistance to cage degradation. Carborane anions ( $[\text{CB}_{11}\text{H}_{12}]^-$  and the derivatives) are among the most weakly-coordinating and least nucleophilic ones of all known anions. Unlike  $[\text{B}_{12}\text{H}_{12}]^{2-}$  dianion, its polarity due to the C atom facilitates its selective functionalization and enables the solubility in water which provide some synthetic advantages. The readers can refer to the reference [80] for detailed information about the derivatives and the synthesis methods. Carborane anions also exhibit high electrochemical and chemical stability similar to their isoelectronic neutral carborane counterparts. Having a large steric profile, easy functionalization, and compatibility for the integration into more complex systems are other attractive properties of these clusters. Despite all the advantageous features, their production cost is the main barrier to their widespread use.[81]

Neutral icosahedral carborane exists as three isomeric members, which are *ortho-* (*o-*), *meta-* (*m-*) and *para-*carborane (*p*-carborane) presented in Figure 1.3. Apart from the differences in their electronic structure, the most prominent common feature is their highly stable skeletal framework. Isomerization from *o*-carborane to *m*-carborane occurs upon heating above 425 °C, which then further isomerizes to the most robust isomer, *p*-carborane, over the temperatures of 600 °C due to the electrostatic repulsion between carbon nuclei as driving force. Neutral carborane clusters and their derivatives are highly stable toward degradation under a wide range of conditions from exposure to strong acids and oxidants. Only strong bases can cause the removal of one BH vertex from *o*-carborane resulting in the formation of 11 vertex *nido* structure. The extraordinary cage stability allows the functionalization without disrupting the icosahedral geometry. 3D aromaticity and the electron-withdrawing character of skeletal C atoms with an inductive effect are two main electronic properties that control the substitution. The substitution can occur either by deprotonation and nucleophilic substitution at the acidic C-H vertices or by electrophilic substitution at the hydridic B-H vertices. Although similar methods can be applied for derivatizing the three isomers, the different positions of the C atoms result in significant differences in electronic structure as depending on the C positions, these three isomers exhibit different polarities[82] and consequently show different electronic

acceptor capabilities (para < meta << ortho)[83,84]. Lower polarity and weaker inductive electron attraction of *meta* and *para* isomers result in reduced acidity of C-H, consequently lower reactivity toward metalation at C position compared to the *o*-carborane. Hence, it is more difficult to reduce *m*- and *p*-carboranyl species. All these isomers are highly hydrophobic because of the hydridic character of BH vertices; hence, the formation of classical hydrogen bonds is prevented. On the other hand, weakly acidic CH vertices allow them to incorporate functional organic systems. Difficulty in synthesis and high cost because of the absence of large-scale production are also the main problems for these neutral clusters.[85] For detailed information about synthesis and derivation of neutral icosahedral carboranes, “Carboranes” book by Russell Grimes can be consulted.[86,87]

### 1.4.3 Applications

The highly stable nature of icosahedral borane/carborane clusters in terms of thermal and chemical stability draws the attention as remarkable building blocks in a wide variety of material science studies[88,89] and they have been the subject of study in many research fields such as catalysis, electronics, energy storage, medicinal applications, etc.[48,89–95] due to their unusual properties.

The versatility in electronic tailoring potential of polyhedral boron-based systems by introducing electron-withdrawing or electron-donating substituents brings a remarkable advantage to especially metal-boron cluster chemistry for their use in catalyst design.[46] Jordan et al. investigated a novel hafnium carboranyl hydride complex as an analogue to a metallocene-based catalyst for the catalyzation of alkyne hydrogenation reactions and showed its catalytic activity.[96] The use of zirconium and titanium complexes of polyhedral carboranes as catalysts in the polymerization of ethylene were reported.[97–100] Other applications of metallocarboranes in catalysis are polymerization of styrene[101] and *n*-butyl acrylate[102]. The catalytic applications of metallocarboranes are still in the exploratory stage; however, studies that may lead to their industrial use continue.

Their great potential in medical applications due to their inherent properties such as high stability, biocompatibility, easy functionalization, and high boron content has been one of the important driving forces in the development of boron-based chemistry.[103] Medical applications include mainly boron neutron capture therapy (BNCT) for cancer and pharmacophore chemistry. Solubility in water is an important precondition for many medical applications. The sodium salt of parent borane dianion, Na<sub>2</sub>[B<sub>12</sub>H<sub>12</sub>], and

carborane anion,  $[\text{CB}_{11}\text{H}_{12}]^-$ , are the extensively studied polyhedral clusters in medical studies since they also meet the solubility requirement. The absence of a clear reaction center in the borane dianion makes its functionalization problematic. Carborane anion, on the other hand, is found as a more suitable option as it combines the advantages of both neutral carboranes and borane dianion. Boron neutron capture therapy (BNCT) for cancer treatments is a binary method based on the nuclear reaction of two essential nontoxic species, nonradioactive  $^{10}\text{B}$  and low-energy thermal neutrons.[104] BNCT provides an alternative way to selectively destroy cancer cells even for glioblastoma multiforme, which is extremely resistant to all current therapy methods.[104–106] For a successful treatment, a boron delivery agent has to meet some requirements such as low systemic toxicity, high tumor/normal tissue concentration ratios, and rapid clearance from blood and normal tissues.[107] The reason behind the preference for polyhedral boron clusters instead of any boron-based compounds in BNCT studies is their high boron atom number per molecule, extremely high stability, and low toxicity. However, only a few polyhedral borane systems are used in clinical treatments and there is still a need to develop more selective and effective boron delivery agents to turn BNCT into a viable treatment method; and a lot of work is still required to achieve a breakthrough in BNCT. The potential of boranes/carboranes in medical applications is not limited to BNCT. The development in carborane chemistry led to the investigation of these molecules as pharmacophores. Carboranes are used as hydrophobic pharmacophores; their versatile chemistry and incorporation with organic substituents allow their use in drug design.[48,108]

Salts of highly stable  $[\text{CB}_{11}\text{H}_{12}]^-$  anion and its derivatives are of great interest especially for electrochemical systems.[109] As an alternative to Li-ion batteries, Mg-based systems have been studied intensively due to the lower cost, higher abundance of Mg in the earth's crust, and higher tolerance of Mg to air.[110–113] 12-vertex closo-carborane anion involving Mg systems has attracted scientists as an option for halide-free Mg batteries with enhanced electrochemical performance. For example, it was utilized in magnesium batteries in the Toyota Research Institute,[114,115] due to its extreme redox stability and noncorrosive nature unlike other electrodes employed in these systems.[116,117]

Utilizing the boron clusters family is also of interest for nonlinear optics applications. Among this family,  $[\text{B}_{12}\text{H}_{12}]^{2-}$  dianion and  $[\text{C}_2\text{B}_{10}\text{H}_{12}]$  isomers take the attention as electron donor and strong electron acceptor, respectively.[118] Examples of

such systems for the optical responses have been investigated by different groups.[119–126]

Polyhedral (car)boranes are excellent units for constructing different molecular architectures exhibiting a wide range of features. Having a compact, aromatic 3D structure as well as high chemical and thermal stability, borane clusters become a widely used structural component for functional polymeric materials, which are called boron cluster-containing polymers. The compact and near-spherical structure of icosahedral borane derivatives plays an important role in acting as linkers in 3D-network materials. Interaction of  $[B_{12}H_{12}]^{2-}$  with metal (M) centers is dominantly established through M-H-B bridge formation in the coordination networks, whereas the covalent interactions involving C-R units (e.g., R = carboxylate) become important for the 3D networks linked by  $C_2R_2B_{10}H_{10}$ . [127] The introduction of borane clusters into polymeric frameworks provides new functionalities to the polymeric materials while also improving the thermal and electrochemical properties of polymers. For example, the use of boron cluster-containing polymers can provide an ablation-resistant coating for ceramics or can contribute to obtaining oxidation-resistant materials. The biocompatibility of boron clusters allows their use also in biomedical applications.[128] The attractive features of boron clusters also allow them to be used as functional units affecting the electronic structure in molecular rods for the development of novel liquid crystals.[46]

Apart from their potential in medicine, energy storage, catalysis, and as building blocks, there is a significant interest in carboranes for their use in luminescent materials in various applications such as light-emitting diodes (LEDs), lasers, probes, sensors, etc.[129,130] The most popular strategy to design luminescent materials with intriguing emission properties is the development of carborane-fluorophore conjugates in recent years. [93,131–143] Neutral carboranes also offer the possibility to tune the electronic properties of luminescent molecules without causing complications arising from their steric effect.[144]

For these systems, both absorption and emission spectra were found to be dominated by the fluorophore unit as expected as a result of the transparency of carboranes in the UV/Vis region over 200 nm. In addition to which isomer is used, the substituents and their positions in a carborane-fluorophore system are of great importance in modification of the luminescent properties. Since the cage carbon atoms are next to each other, the effect of the substitution at the second cage carbon becomes more pronounced in *o*-carborane systems. These effects were demonstrated clearly in the work

by Teixidor et al.[129] The authors reported that in the *o*-carborane-anthracenyl systems, phenyl (Ph)-substituted derivative does not exhibit any fluorescence due to the charge transfer between the Ph and anthracenyl units. It was also shown that the low quantum yield can be prevented by using a spacer to separate the fluorophore from the cluster. Similar fluorescence quenching was also reported by the same group as a result of the introduction of Ph to the carborane-styrene system.[145] Many carborane-based-luminescent systems appear to have significantly enhanced emission yields in a crystal or an aggregated state contrary to their solutions.[93,146] Observation of significant increases in emission quantum yield as a result of bulky substituents, as in the example of tetramethylsilyl (TMS)[94], at the second cage carbon in the solution state, points up that the free rotations in solution is an important factor in emission quenching. It has been shown by Chujo's group[147] that another important factor affecting the quantum yield in *o*-carborane-fluorophore systems is the distance between the cage carbon atoms ( $C_c-C_c$ ). Their experimental study proved that emission quenching can be induced by bond elongation in the absence of intramolecular rotation.[148] The theoretical study of Duan et al. clearly demonstrated how the transition switches from the local excitation to a charge transfer upon  $C_c-C_c$  elongation.[149] Photophysical properties of *o*-carborane-based systems are addressed in Chapter 4 in more detail.

# Chapter 2

## Theoretical Background

Our studies in this thesis cover the computational investigation of the ground state energetics along with the excited state and spectroscopic properties of boron-based materials. Before the detailed presentation of the studies, this chapter aims to give a brief theoretical background behind our calculations.

### 2.1 Quantum Mechanics / Electronic Structure

Computational chemistry aims to understand the underlying mechanisms of the chemical phenomena observed in experiment, and provide guidance to the experimental work with accurate predictions. Depending on the problem in question, different methodologies are available mainly in four broad classes: molecular mechanics (classical force fields), ab initio methods, semi-empirical methods and density functional theory (DFT). Among these methods, molecular mechanics is based on a very simple model, in which the molecules are considered as a collection of spheres (atoms) held together by springs (bonds), where the system is treated classically based on force fields. In comparison, the rest of the formalisms have different approaches for the solutions to general energy problem, they are all based on the quantum mechanical treatment of an N-body system; and this treatment has the Schrödinger equation at its core. This brings us to the electronic problem.

#### 2.1.1 The Electronic Problem

A plain but not simple expression for the complete (non-relativistic) quantum description of an N-body system is given by the Schrödinger equation:

$$\hat{H}|\Psi\rangle = E|\Psi\rangle \quad (2.1)$$

where  $\hat{H}$  is the Hamiltonian operator, and  $\Psi$  is the wave function describing the system. The eigenvalue of this equation,  $E$ , is the energy of the system including nuclei and electrons. Here, the Hamiltonian operator corresponds to the total energy of the system and includes all kinetic and potential energies of the particles as described below in atomic units:

$$\hat{H} = - \sum_{i=1}^N \frac{1}{2} \nabla_i^2 - \sum_{A=1}^M \frac{1}{2M_A} \nabla_A^2 - \sum_{i=1}^N \sum_{A=1}^M \frac{Z_A}{r_{iA}} + \sum_{i=1}^N \sum_{j>i}^N \frac{1}{r_{ij}} + \sum_{A=1}^M \sum_{B>A}^M \frac{Z_A Z_B}{R_{AB}} \quad (2.2)$$

$M_A$  is the ratio of the mass of nucleus  $A$  to the mass of an electron,  $Z_A$  is the atomic number of nucleus  $A$ , and  $\nabla^2$  is the Laplacian operator. The first and the second terms are the operators for the kinetic energy of the electrons ( $T_e$ ) and nuclei ( $T_n$ ), respectively. Potential energy resulting from the Coulomb attraction between electrons and nuclei ( $V_{en}$ ) is represented with the third term, while the fourth and the fifth terms correspond to the repulsion between electrons ( $V_{ee}$ ) and between nuclei ( $V_{nn}$ ), respectively. Equation (2.2) shows that the number of electron-electron interactions that has to be considered increases with the increasing number of electrons as the system size grows.

Equation (2.1) can only be solved approximately for the systems composed of more than two particles (many-body problem). Therefore, the solution of the equation requires certain approximations. A good starting point is the Born-Oppenheimer approximation, which can be introduced to simplify the problem by reducing it to an electronic problem only. It is a central approach in quantum chemistry, which suggests that since nuclei are much heavier than electrons, they move much slower and electrons can be considered to be moving in the field of fixed nuclei.[150] Therefore, the kinetic energy term of nuclei can be neglected while the potential energy of the repulsion between the nuclei can be considered to be constant. Within this approximation, the Schrödinger equation can be separated into an electronic and a nuclear equation. Therefore, we can now focus on solving the Schrödinger equation with the electronic Hamiltonian.

### 2.1.2 Variational Method

One of the main approximations in quantum mechanics is the variational method. According to the variational principle for the ground state, the energy of a trial wavefunction is always higher than the exact ground state energy, whereas equality is only satisfied when the trial wavefunction matches the exact ground-state wavefunction.



Therefore, the best wavefunction for the system by definition is the one that minimizes the energy. The variational theorem written in Dirac's notation is:

$$\frac{\langle \Psi | \hat{H} | \Psi \rangle}{\langle \Psi | \Psi \rangle} \geq E_0 \quad (2.3)$$

where  $|\Psi\rangle$  is the trial wave function. The denominator is written to secure the normalization condition.

The Hartree-Fock (HF) method and the Density Functional Theory (DFT) based on the variational theorem are discussed in the following sections.

## 2.2 Hartree-Fock Theory

The Hartree-Fock (HF) theory is an approximate method for solving the time-independent Schrödinger equation, and is an important starting point for other computational methodologies. HF theory provides a concrete basis for the molecular orbital (MO) approach in chemistry through Koopmans' theorem as the wavefunction ( $\Psi$ ) of an N-electron system is given as a set of one-electron wavefunctions by a single Slater determinant:

$$\Psi(x_1, x_2, \dots, x_N) = \frac{1}{\sqrt{N!}} \begin{vmatrix} \chi_i(x_1) & \chi_j(x_1) & \dots & \chi_k(x_1) \\ \chi_i(x_2) & \chi_j(x_2) & \dots & \chi_k(x_2) \\ \vdots & \vdots & \ddots & \vdots \\ \chi_i(x_N) & \chi_j(x_N) & \dots & \chi_k(x_N) \end{vmatrix} \quad (2.4)$$

where  $\chi(x)$  denotes the spin orbitals. Exchange effects are introduced by the antisymmetric nature of a Slater determinant and the Pauli exclusion principle is satisfied. In HF, the N electron system is handled as a set of one-electron equations to solve the Schrödinger equation. As the variational principle states, the wavefunction that provides the lowest possible energy is the best wavefunction describing the system. So, the Hartree-Fock equation is derived by minimizing the energy with respect to the choice of spin orbitals, which results in the one-electron HF equations:

$$f(i)\chi(x_i) = \epsilon\chi(x_i) \quad (2.5)$$

where  $f(i)$  is the Fock operator, which is an effective one-electron operator described as followed:

$$f(x_i) = -\frac{1}{2}\nabla_i^2 - \sum_{A=1}^M \frac{Z_A}{r_{iA}} + v^{HF}(x_i) \quad (2.6)$$

In the electronic Hamiltonian, the kinetic energy and electron-nuclei attraction terms are separable and they can be written for each electron in the same form in one electron equation. On the other hand, it is not possible to divide the electronic repulsion term into a single-electron term; therefore, the presence of other electrons is expressed as an average potential of all other electrons experienced by the  $i$ th electron,  $v^{HF}(x_i)$ . The dependence of this term on the wave function of the entire system creates a nonlinear problem, hence the equation (2.5) must be solved iteratively. Here the basic idea is to perform iterative calculations by making an initial guess at the spin orbitals to calculate the average field ( $v^{HF}$ ) and then solving the HF equation (2.5) for a new set of spin orbitals until the calculated spin orbitals converge to the ones used to construct the Fock operator within a set of iteration factor (self-consistency).[151]

In a real system, the electronic interactions are very complicated. Negatively charged electrons repel each other, and this clearly affects their motion. The electrons have a strong tendency to avoid each other to minimize the repulsion. Therefore, the motions of the electrons are highly correlated, and one of the fundamental challenges in computational chemistry is the correct description of the correlated wavefunction. This problem is simplified by the HF method with the construction of the wavefunction of uncorrelated electrons. HF is a very useful approximation for providing initial predictions for many systems and a good base-level theory. However, it falls short of yielding accurate energetics because of its neglect of electron correlation. When high accuracy is desired, the electron correlation has to be considered with methods such as Configuration Interaction (CI), Møller–Plesset (MP) perturbation theory, and Coupled-Cluster (CC) methods. However, since a very high accuracy in the calculations demands high-computational cost and time, and they also have limitations on the system size. Therefore, the choice of the method depends heavily on the interplay between the accuracy and system size.

## 2.2.1 Self-Consistent Field Procedure

Within the self-consistent field approach, the first step is to make an initial guess for the spin orbitals. Each spin orbitals ( $\chi_i(x)$ ) consists of two parts: the spatial ( $\psi_i(r)$ ) and the spin functions ( $\psi_{spin}(s)$ ).

$$\chi_i(x) = \psi_i(r)\psi_{spin}(s) \quad (2.7)$$

Here the spin function can be simplified by the spin integration under the restricted orbital assumption and the spatial part could be written as a set of spatial basis functions.

$$\psi_i(r) = \sum_{v=1}^K C_{vi}\varphi_v(r), \quad i = 1, 2, \dots, K \quad (2.8)$$

$C_{vi}$  and the  $\varphi_v(r)$  represents the expansion coefficients and the basis functions, respectively. As suggested by Roothaan[152], introducing this equation allows us to reduce the problem of finding the wave functions to the problem of calculating a set of expansion coefficients. Thus, the HF equation (2.5) becomes a computation-friendly matrix equation.

$$\sum_v F_{\mu\nu}C_{vi} = \varepsilon_i \sum_v S_{\mu\nu}C_{vi}, \quad i = 1, 2, \dots, K \quad (2.9)$$

In this equation, the Fock matrix,  $F_{\mu\nu}$ , and the overlap matrix,  $S_{\mu\nu}$ , are both  $K \times K$  Hermitian matrices. Fock matrix is the matrix representation of the Fock operator and could be written as the summation of the core-Hamiltonian ( $H_{\mu\nu}^{core}$ ), which involves the one-electron operator describing the kinetic energy and the nuclear attraction of an electron, and the two-electron part ( $G_{\mu\nu}$ ). Before giving any detail about the steps of SCF calculation, it is also necessary to mention the density matrix. The total density of a closed-shell system of N electrons described by a single determinant wave function with occupied molecular orbitals ( $\psi_a$ ) holding two electrons is

$$\rho(r) = 2 \sum_a^{N/2} |\psi_a(r)|^2 \quad (2.10)$$

and charge density could be defined in terms of density matrix with the introduction of molecular orbital expansion (Eq. 2.8) as

$$\rho(r) = \sum_{\mu\nu} P_{\mu\nu} \varphi_{\mu}(r) \varphi_{\nu}^*(r) \quad (2.11)$$

where the density matrix  $P_{\mu\nu}$  is directly related to the expansion coefficients  $C$ .

$$P_{\mu\nu} = 2 \sum_a^{N/2} C_{\mu a} C_{\nu a}^* \quad (2.12)$$

After introducing the required definitions and calculations involved in the self-consistency procedure, finally, we can summarize the SCF calculation steps as follows.



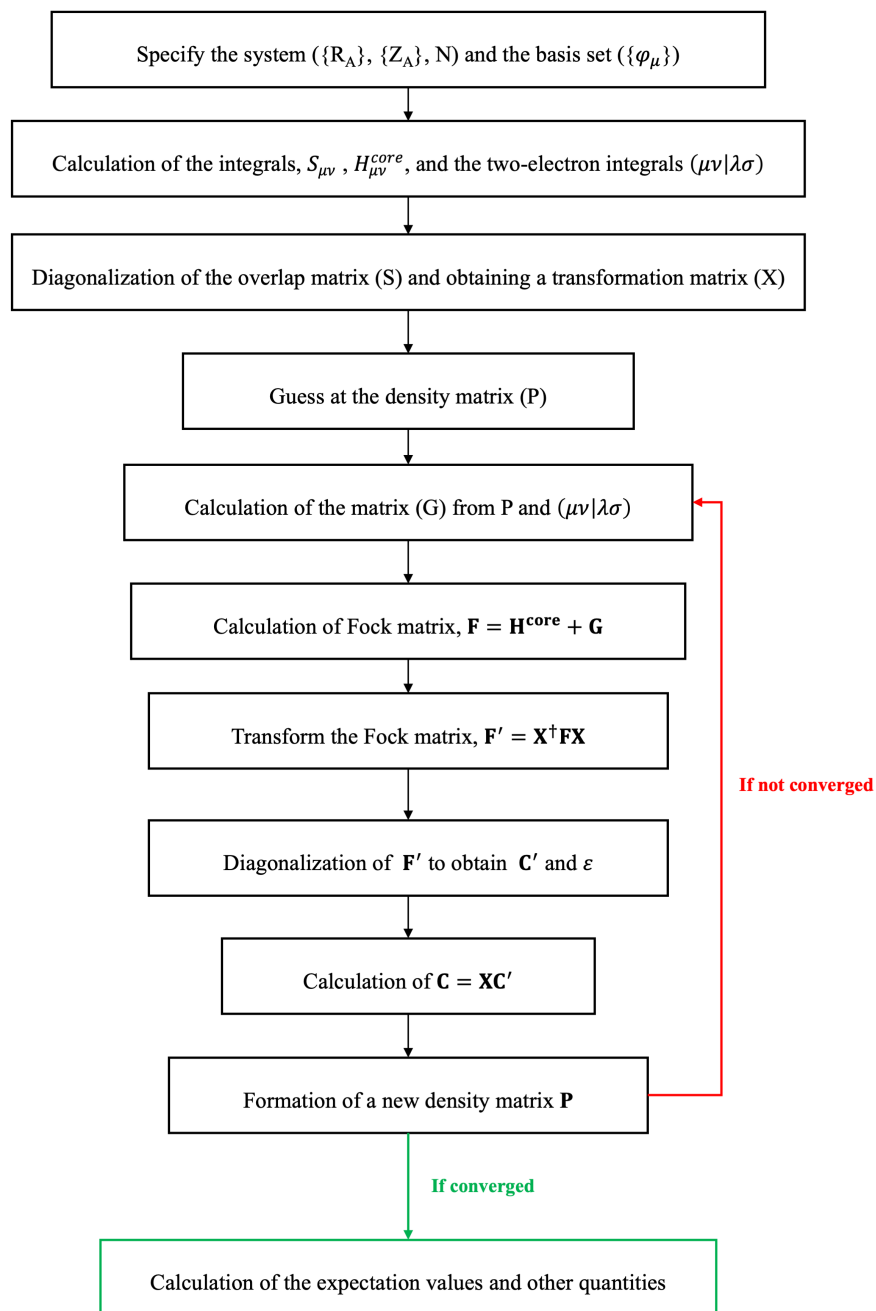


**Figure 2. 1** Diagram of SCF calculation procedure

As a result of this procedure, the electronic wave function, hence the electronic energy, is obtained within the Born-Oppenheimer approximation. The total energy is calculated by adding the nuclear-nuclear repulsion to the electronic energy, and this calculation is repeated for different nuclear coordinates to explore the potential energy surface of nuclear motion.

## 2.3 Density Functional Theory

The approach of defining the energies of many-body systems in terms of electron density was first put forward in the Thomas-Fermi model.[153–155] However, the basis of modern density functional theory (DFT) was later constructed by Hohenberg and Kohn,[156] known as the Hohenberg-Kohn (HK) theorems. The first HK theorem states that the Hamiltonian operator, hence any ground-state property of a molecule, is a functional of the ground state electron density function. The dependence of the components in the ground state electronic energy expression can be written as:

$$E_0[\rho_0] = T[\rho_0] + V_{ee}[\rho_0] + V_{ext}[\rho_0] \quad (2.7)$$

where  $T[\rho_0]$  is the kinetic energy of the electrons,  $V_{ee}[\rho_0]$  is the energy term for the electron-electron repulsion and  $V_{ext}[\rho_0]$  is the external potential energy due to the nuclei-electron attraction. The last term is defined as:

$$V_{ext}[\rho_0] = \int \rho_0(\vec{r})v_{ext}d\vec{r} \quad (2.8)$$

and the rest is collected into a new quantity, the Hohenberg-Kohn functional,  $F_{HK}[\rho_0]$ . So, the energy definition can be written in the following form:

$$E_0[\rho_0] = F_{HK}[\rho_0] + \int \rho_0(\vec{r})v_{ext}d\vec{r} \quad (2.9)$$

The variational approximation in DFT is introduced with the second HK theorem, which states that the energy calculated by any trial electron density function will be higher than or equal to the exact ground state energy ( $E_0 \leq E[\rho]$ ). Although the existence of the energy functional is proved by the HK theorems, the form of the functional is unfortunately not defined. Further developments in DFT were provided by Kohn and Sham[157] and a way to approach the unknown functional was suggested. In 1998, the Nobel Prize in Chemistry was shared equally between Walter Kohn for his development of the density-functional methods and John A. Pople for his role in the development of the computational methods in quantum chemistry.[158]

### 2.3.1 Kohn-Sham Equations

The Kohn-Sham (KS) equations, the basis of the current DFT calculations, have emerged as a result of a similar treatment to the HF variational approach. An initial trial

electron density function,  $\rho$ , is used to calculate an initial guess of Kohn-Sham orbitals and energy; then the calculation proceeds iteratively through an SCF method similar to that used in HF.

Within the framework of the KS approach, the major part of the energy is computed with good accuracy and the rest arising particularly from the electron-electron interaction is determined by an approximate functional.[159] In the energy definition in Eq. 2.9, the unknown functionals are the electronic kinetic energy and the electron-electron interactions. The KS approach is also based on a fictitious system of non-interacting electrons, which gives the exact density of the interacting system. As a result of this approach, the system can be described by a single determinant wavefunction consisting of KS-orbitals in a similar manner to HF formalism. Within this approach, the kinetic energy of a system now can be written as follows:

$$T_s[\rho] = -\frac{1}{2} \sum_i^N \langle \psi_i | \nabla^2 | \psi_i \rangle \quad (2.10)$$

Here is the kinetic energy, ( $T_s[\rho]$ ), is not the true kinetic energy; instead, it represents the kinetic energy of a system of non-interacting electrons, which produce the ground-state electron density. For a system of N electrons, the exact total electron density is defined as:

$$\rho(r) = \sum_{i=1}^N |\psi_i(r)|^2 \quad (2.11)$$

where  $\rho(r)$  is the exact electron density of the system calculated from the one-electron orbitals of the non-interacting system. The classical Coulomb interaction, which forms a significant part of electron-electron interaction, can also be calculated as:

$$V_c[\rho] = \frac{1}{2} \int \frac{\rho(r_1)\rho(r_2)}{|r_1 - r_2|} dr_1 dr_2 \quad (2.12)$$

The all errors rising from the electron-electron interaction are summed up under the term *exchange-correlation functional*;

$$E_{xc}[\rho] = (T[\rho] - T_s[\rho]) + (V_{ee}[\rho] - V_c[\rho]) \quad (2.13)$$

where  $(T[\rho] - T_s[\rho])$  stands for kinetic energy that is not covered by the non-interacting reference system, and  $(V_{ee}[\rho] - V_C[\rho])$  gives the difference between non-classical electron-electron interaction and classical Coulomb interaction. After all, the energy functional takes the following form in the KS approach:

$$E[\rho] = T_s[\rho] + V_{ext}[\rho] + V_C[\rho] + E_{xc}[\rho] \quad (2.14)$$

As stated before, similar to the HF approximation, now the variational principle can be applied and KS orbitals, which minimize the energy expression, can be calculated using the following equation:

$$\left[ -\frac{1}{2}\nabla^2 + v_{ext}(r) + \int \frac{\rho(r')}{|r-r'|} dr' + v_{xc}(r) \right] \psi_i^{KS}(r) = \varepsilon_i \psi_i^{KS}(r) \quad (2.15)$$

in which the local exchange-correlation potential,  $v_{xc}(r)$ , is introduced as follow:

$$v_{xc}(r) = \frac{\delta E_{xc}[\rho]}{\delta \rho} \quad (2.16)$$

Being the derivative of the functional  $E_{xc}[\rho(r)]$ ,  $v_{xc}(r)$  depends also on the  $\rho(r)$ , and varies at different points in the molecule, like  $\rho(r)$ . One advantage of using the electron density function instead of wave-function based Schrödinger equation is that the electron density is a function of position only, of three variables (x, y, z), and while the wavefunction is a function of 3N variables for an N-electron system. Consequently, DFT offers a computationally less demanding way to take the electron correlation into account. However, while the use of larger basis sets and higher correlation levels improve the wavefunction and approach us to an exact solution of the Schrödinger equation in ab-initio methods, improvement of the solution is unfortunately not so straightforward in DFT, and it requires some intuition coming from the previous experiences and comparison of the results with experimental data or with a reference high-level ab initio method to select an appropriate functional.[160]

### 2.3.2 Exchange-Correlation Functionals

The exact energy of the many-body system can be calculated only if the exact functional is known. Against the well-defined mathematical form of the Schrödinger equation in the ab-initio methods, the form of the exchange-correlation functional in DFT



functional is not known. Therefore, the quality of the DFT depends on the accuracy of the approximation to  $E_{xc}$ , and the main challenge of DFT is finding an appropriate functional for the system of interest.

At the moment, there are many different functional options available, and as stated earlier it is required a benchmark with experimental or a more accurate method for a better judgement. Still, it is very valuable to have a basic knowledge about the functional. A brief background on the derivation and structure of functionals are given in the next sections.

### 2.3.2.1 Local Density Approximation (LDA) for $E_{xc}[\rho]$

*Local density approximation* is the simplest approximation to  $E_{xc}[\rho(r)]$ , and is based on the idea of the hypothetical homogeneous electron gas. The assumption behind this model is that the value of *energy density* ( $\epsilon_{xc}$ ), which is the exchange and correlation energy per electron, equal to that given by a homogeneous electron gas with the same electron density at that point.[160] In LDA, the exchange-correlation functional given as:

$$E_{xc}^{LDA} = \int \rho(r) \epsilon_{xc}[\rho(r)] dr \quad (2.17)$$

LDA is found to surprisingly yield accurate results for the structural properties but it is not a reliable option for exchange-correlation functional in computing energies. Since the homogeneous electron gas model physically resembles an idealized metal with uniformly distributed valence electrons and positive charges, LDA can also be considered an appropriate method for simple metals. However, rapidly varying electron density, which is the case for the majority of the real systems, reduces the accuracy of this functional.[159]

For the open-shell atoms and molecules, an extended version of LDA can be utilized. In this version, which is called the *local spin density approximation*, electron spins are specified with different Kohn-Sham orbitals, similar to the unrestricted HF method, and provides only a moderate accuracy, which is also insufficient for most of the real applications in chemistry.

### 2.3.2.2 Generalized-Gradient Density Approximation (GGA) for $E_{xc}[\rho]$

Due to the limitations in the use of the LDA, DFT could not find sufficient use in computational chemistry studies until the early eighties. This situation changed drastically after the inhomogeneity in the electron density was taken into account by adding the

gradient of  $\rho$  to the exchange-correlation energy. The typical form of a GGA functional is written as

$$E_{xc}^{GGA} = \int \rho(r) \varepsilon_{xc}[\rho(r), \nabla\rho(r)] dr \quad (2.18)$$

It is possible to split the  $E_{xc}^{GGA}$  into its exchange and correlation contributions and handle them separately in practice. Although different exchange and correlation functionals can be used in various combinations together, only a few are commonly used in the studies such as BLYP (Becke's exchange[161] and Lee-Yang-Parr correlation[162]) and BP86 (Becke's exchange[161] and Perdew's 1986 correlation functional[163,164]). The GGA results show a considerable improvement for the structural parameters and energy values, especially in the case of binding energies of molecules, and is considered an accurate and efficient procedure for *d*-metal complex systems.[165] Further improvement can also be provided by the addition of the second derivative of  $\rho$  ( $\nabla^2\rho$ ) as in the form of meta-GGA methods.

### 2.3.2.3 Hybrid Functionals

In the exchange-correlation functional, the larger contribution often comes from the exchange part, thus enhancing the accuracy of the exchange expression is naturally the next step to obtain more accurate results from DFT calculations.[159] Herein the exact HF exchange comes into play. The hybrid functionals involve the exact exchange energy of a Slater determinant to some extent in addition to the DFT exchange-correlation energy, hence they provide an option between the non-interacting HF model and interacting electron gas. These functionals mainly differ from each other by having a different percentage of HF exchange. For example, the most popular hybrid functional Becke three-parameter hybrid functional (B3LYP), which is widely used in chemical applications has the following expression:

$$E_{xc}^{B3LYP} = E_{xc}^{LSDA} + a_0(E_x^{exact} - E_x^{LSDA}) + a_x\Delta E_x^{B88} + a_c\Delta E_c^{non-local} \quad (2.19)$$

where the empirical parameters are  $a_0= 0.20$ ,  $a_x= 0.72$  and  $a_c= 0.81$ , and the non-local correlation term is

$$\Delta E_c^{non-local} = E_c^{LYP} - E_c^{VWN} \quad (2.20)$$

More reasonable values for the binding energies, geometries, and frequencies can be obtained with hybrid functionals in general. Analogues to the hybrid GGA functionals, in meta-hybrid functionals the second derivative of  $\rho$  is also added as well as the HF exchange.

## 2.4 Time-Dependent Density Functional Theory

Although DFT is a useful method for the investigation of a wide range of properties of molecules such as equilibrium geometries, ground state energetics, electronic density distributions, and related properties, it is generally limited to the ground state characteristics; and time-dependent processes are beyond the reach of DFT. The dynamical processes in many-body systems such as electronic-excitation processes and their coupling to nuclear motion fall within the scope of time-dependent density functional theory (TDDFT).

The time evolution of a many-body system is treated by the time-dependent Schrödinger equation:

$$i \frac{\partial}{\partial t} \Psi(r, t) = \hat{H}(r, t) \Psi(r, t) \quad (2.21)$$

where the Hamiltonian is

$$\hat{H}(r, t) = \hat{T}(r) + \hat{V}_{ee}(r) + \hat{V}(t) \quad (2.22)$$

The operators for the kinetic energy ( $\hat{T}$ ) and electron-electron repulsion ( $\hat{V}_{ee}$ ), could be expressed as previously given in Eq. 2.2; but the sum of the one-particle potentials, is now a function of time.

$$\hat{V}(t) = \sum_{i=1}^N v(r_i, t) \quad (2.23)$$

The number of electrons,  $N$ , is a constant quantity with time; and the electron density is given as

$$\rho(r, t) = \sum_{i=1}^N |\psi_i(r, t)|^2 \quad (2.24)$$

TDDFT is based on the Runge-Gross theorem[166], which is a time-dependent analogue to the first HK theorem. It proves one-to-one correspondence between the external potential,  $v(r, t)$ , and the electronic density,  $\rho(r, t)$ ; in other words, different time-dependent potentials will cause different time-dependent densities. So that the density could be accepted as a variable that completely determines the dynamics of the system and the KS approach becomes possible to be applied from a time-dependent point of view.

TDDFT is very closely related to some spectroscopic methods, and the calculation of the excitation energies of a molecular system is a very important application of TDDFT in the linear-response regime,[167] and it is based on the equations, first derived by Casida.[168] The excitation energies lying well below the ionization potential for the valence-excited states could be calculated accurately with TDDFT, with an error comparable to those of high-level correlation methods (e.g. EOM-CCSD, CASPT2).[169] A valence-excited state refers to a local excitation that takes place on the same molecule from a valence orbital to an unoccupied level. However, the reliability of DFT-based methods is highly dependent on the choice of the XC functionals; hence, the results of TDDFT calculations should always be checked by comparison with experimental data or benchmark calculations based on correlated wave-function methods.

#### **2.4.1 Charge-Transfer (CT) Problem in TDDFT**

Contrary to the very good results yielded for valence-excited states with TDDFT, serious problems may arise for the correct description of charge-transfer (CT) excited states, which results in a drastic underestimation of the order of several eV for the excitation energies and incorrect asymptotic behavior of potential energy curves of these states. The reason behind the failed  $1/R$  asymptote in the CT states can be explained as the incorrect description of electrostatic attraction between the positive and negative charges in a CT state due to self-interaction error in pure density functionals, where  $R$  corresponds to the distance between the positive and negative charges of the CT state. This effect can be described as that the transferred electron experiences the electrostatic repulsion with itself as if it is still in the orbital it left. Inclusion of nonlocal HF exchange in the exchange-correlation potential could improve the correct  $1/R$  long-range behavior of PES in CT states.[169]

The valence-excitation and charge transfer state are illustrated in Figure 2.2. When there is enough spatial separation between the molecules/fragments A and B,  $i$  and  $j$  orbitals do not overlap with  $a$  and  $b$ .

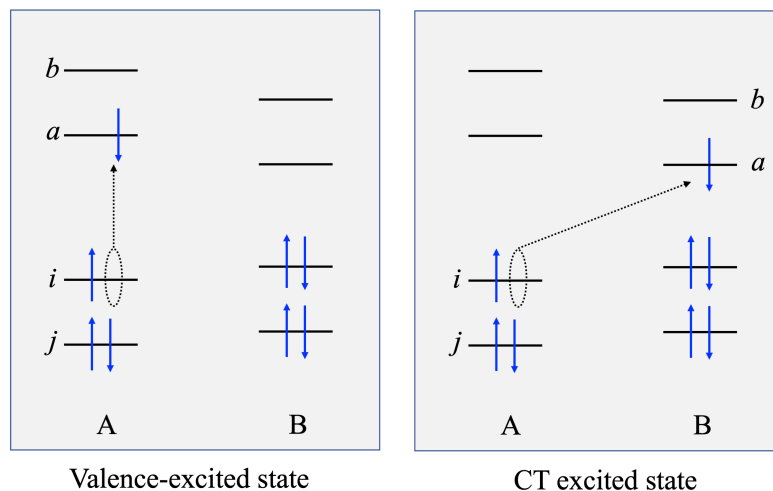


**Figure 2. 2** Schematic representation of a typical valence-excited state and a CT excited state. The transition occurs from the occupied orbital  $i$  to the virtual orbital  $a$ , which are located on the same molecule in the valence-excited state and located on different molecules/fragments in the CT excited state.

Employing hybrid functionals in electronic excitation calculations in time-dependent DFT gives good results for the valence-excitations (local character), however, it can cause failures in charge-transfer states. This problem can be recovered using the long-range corrected density functionals. wB97XD[170] and CAM-B3LYP[171] can be held up as the most popular functionals for the excited state calculations, in which the long-range orbital-orbital exchange interaction is treated with HF exchange contribution. Another example is a high nonlocality functional M06-2X[172,173], with double amount of nonlocal exchange, which is used in our excited-state study given in Chapter 4.

### 2.4.2 Excited State Analysis

Various excited state properties can be used to investigate the nature of excitation and some of them can also be very useful as a warning about the applicability of the selected method. In this section, the  $\Delta r$  and  $\Lambda$  indexes used in the excited state analysis in Chapter 4 will be briefly explained.

$\Lambda$  index, developed by Peach et al.[174], is a measure of the orbital overlap for electron and hole and has been also used as a diagnostic tool that provides a correlation

between the error in excitation energies and orbital overlap for some hybrid and GGA functionals. The index is expressed as

$$\Lambda = \frac{\sum_{ia} \kappa_{ia}^2 \int |\varphi_a(r)| |\varphi_i(r)| dr}{\sum_{ia} \kappa_{ia}^2} \quad (2.25)$$

which has the value  $0 \leq \Lambda \leq 1$ . Small and large values of  $\Lambda$  indicate long-range and short-range excitations, respectively.  $K_{ia}$  includes both excitation ( $X_{ia}$ ) and de-excitation ( $Y_{ia}$ ) coefficients.

$$\kappa_{ia} = X_{ia} + Y_{ia} \quad (2.26)$$

In the related work, it was shown that low values ( $\Lambda \leq 0.3$ ) are associated with high errors in the excitation energies while large values refer to smaller errors for the calculations, where PBE and B3LYP functionals are used. There is not such a correlation for CAM-B3LYP, which the best results among the functionals used were yielded even for the CT and Rydberg states.

$\Delta r$  index was developed by Guido et al.[175] as a new tool to be used in obtaining some indications about the nature of the electronic transitions under investigation. It basically corresponds to the average electron-hole distance upon excitation. It is expressed as follows

$$\Delta r = \frac{\sum_{ia} K_{ia}^2 |\langle \varphi_a | r | \varphi_a \rangle - \langle \varphi_i | r | \varphi_i \rangle|}{\sum_{ia} K_{ia}^2} \quad (2.27)$$

where the norm of the orbital centroid is represented by  $\langle \varphi_i | r | \varphi_i \rangle$ . Valence-excitations are characterized by the short  $\Delta r$  values, while much larger values correspond to the CT excitations. The values larger than 2.0 Å were found to refer to a high error in the transition energies calculated by various GGA and hybrid functionals, and the use of a range-separated hybrid functional or a hybrid with high (>33%) HF exchange becomes mandatory for more reliable results.

## 2.5 Basis Sets

Linear combination of atomic orbitals (LCAO) to yield approximate molecular orbitals (MOs) is expressed with a set of mathematical functions, which are called a basis set. The functions do not have to necessarily be representing the correct atomic orbitals; any set of mathematical functions building the useful MOs can be used.

The basis functions differ in how they represent the electron distribution around an atom. Due to their simplicity, Slater and Gaussian functions are the basis functions currently used in computational chemistry studies. Although a better approximation to atomic wavefunctions is provided by Slater-type orbital (STO) functions, evaluation of the integrals is much faster for the Gaussian-type orbital (GTO) functions.[176] The fast calculation becomes much more important with increasing size of the system, due to the significant increase in the number of two-electron integrals. Poor definition of a Gaussian function is eliminated by the linear combination of primitive Gaussian functions with a set of contraction coefficients to approximate the Slater function.

In this thesis, Pople's basis sets [177–180] were used, which are a different way of the convention of Gaussian functions in a split valence nature, where the valence and inner-shell atomic orbitals are represented separately by two single basis functions, respectively. The addition of polarization and diffuse functions (especially necessary for anions, Rydberg states, and highly electronegative atoms) can also be added for a better description of MOs, depending on the studied system.

## 2.6 Computational Procedures

### 2.6.1 Geometry Optimization and Frequency Calculation

The interest of the study might be a minimum or a transition state. For the ground-state structures, the calculation is based on energy minimization and corresponds to finding the geometry where the energy is minimum on the PES. The choice of input structure that is closer to the desired stationary point for the geometry optimizations is important to obtain correct ground-state structures. All the stationary points correspond to a minimum on the potential energy surface and the first derivative of the PES with respect to each geometric parameter is zero at these points. The global minimum is a minimum in all directions, but a saddle point is a minimum in all directions except along

the reaction coordinate. Therefore, the global minimum and a saddle point can be distinguished by the second derivatives, as written below:

<p><u>For a minimum</u></p> $\frac{\partial^2 E}{\partial q^2} > 0$	<p><u>For a transition state</u></p> $\frac{\partial^2 E}{\partial q^2} > 0 \text{ for all } q, \text{ except along the reaction coordinate}$ $\frac{\partial^2 E}{\partial q^2} < 0 \text{ along the reaction coordinate}$
---	---

The use of first and second derivatives of the energy is the most widely-used algorithm for geometry optimization. In the optimization procedure, the gradient matrix for the input structure is written as

$$\mathbf{g}_i = \begin{pmatrix} (\partial E / \partial q_1)_i \\ (\partial E / \partial q_2)_i \\ \vdots \\ (\partial E / \partial q_{3n})_i \end{pmatrix} \quad (2.21)$$

for a system of  $n$  nuclei, which generates a  $3n$ -dimensional hypersurface on a  $(3n+1)$ D graph.  $q_N$  represents the  $3n$  geometric parameters, as each atom is defined with three coordinates ( $x$ ,  $y$ , and  $z$ ). The second derivative of the energy gives the force constant matrix, which is called the Hessian.

$$\mathbf{H} = \begin{pmatrix} \partial^2 E / \partial q_1 q_1 & \partial^2 E / \partial q_1 q_2 & \cdots & \partial^2 E / \partial q_1 q_{3n} \\ \partial^2 E / \partial q_2 q_1 & \partial^2 E / \partial q_2 q_2 & \ddots & \partial^2 E / \partial q_2 q_{3n} \\ \vdots & \vdots & \ddots & \vdots \\ \partial^2 E / \partial q_{3n} q_1 & \partial^2 E / \partial q_{3n} q_2 & \cdots & \partial^2 E / \partial q_{3n} q_{3n} \end{pmatrix} \quad (2.22)$$

Although the Hessian is used for the characterization of the minima, transition states, or hilltops, it is particularly important for the calculation of infrared (IR) spectra of molecules.

The general matrix equation can be written as

$$\mathbf{q}_o = \mathbf{q}_i - \mathbf{H}^{-1} \mathbf{g}_i \quad (2.23)$$

where the input and optimized geometries are defined as the geometry coordinate matrices  $\mathbf{q}_i$  and  $\mathbf{q}_o$ , respectively. In the first step, an approximate Hessian is often obtained by molecular mechanics. After the first optimized geometry is calculated, it becomes the input geometry for the next step and is used to create a new gradient matrix



and Hessian. Due to the computational cost of analytical calculation of the second derivatives, the Hessian is computed with the following approximation:

$$\frac{\partial^2 E}{\partial q_i \partial q_j} \approx \frac{\Delta(\partial E / \partial q_j)}{\Delta q_i} \quad (2.24)$$

The optimization process in Eq. 2.23 repeats until the geometry and the gradients meet the optimization criteria for the minimization of the total energy.[160] In case of the interest in the IR spectrum of the molecule, the normal-mode frequencies can be calculated by an analytical frequency calculation, hereby the direction vectors and force constants can be obtained by the matrix diagonalization of the Hessian.

## 2.7 Solvation Methods

The study given in Chapter 4 involves the calculations simulated in a solvent medium to simulate the experimental conditions as much as possible. Therefore, it may be useful to give general information about solvation methods in this section to provide a sense without any details of the calculations.

Including the solvation effects in a calculation adds to the computational cost. Therefore, one of the issues to consider before starting a computational work is whether it is really necessary to take the solvation effects into account. When the purpose of the study is to investigate the inherent properties of a molecule, gas-phase computations can be adequate and the addition of a solvent only increases the complication of the calculations. On the other hand, the inclusion of the solvation in some studies, e.g., biological reactions, is unavoidable, and neglecting it is an obvious oversimplification that casts a shadow on the reliability of the results.

Solvation can be treated computationally in two basic approaches: microsolvation and continuum solvation.[160] Microsolvation is an explicit solvation method where the solution condition is attempted to be provided by placing a certain number of solvent molecules around the solute molecule. Although this approach can be important to see the solvent effect, it may remain insufficient to reflect the real cases. On the other hand, the solute is placed in a cavity within a solvent medium, and the interactions are calculated between the solute and the cavity in continuum solvation methods, which provides a better description of the solvent medium. Several different models with different levels

of sophistication are available in many computational chemistry programs. The integral equation formalism variant of the polarizable continuum model (IEF-PCM)[181–185], which is the default method in Gaussian 09, is used to add the solvent medium in our calculations.



# Chapter 3

## Substituent Effects on the Stability of Borane Dianions

### 3.1 Introduction

Boron has a rich and versatile coordination chemistry with an expectation of having analogous properties to carbon in respect of forming various bonds with different elements, but through different dynamics compared to carbon. As a result of its electron deficiency and strong bonding capacity with large coordination numbers via multicenter bonding, boron-containing systems have attracted considerable research interest in cluster chemistry[3,16,186,187]. For a few decades, the focus of the experimental and theoretical studies on various boron clusters such as bare boron clusters, boranes, carboranes, metallaboranes etc.[63–65,188] has been to identify stable and low-energy conformations while exploring their electronic and chemical properties for potential applications[46]. Many boranes and derivative clusters have been theoretically predicted and experimentally observed as stable gas phase dianions[189–194], which makes them potential materials for the use in different applications as charged anion class. More recently, (car)boranes and their derivatives have shown to be promising candidates as electrolytes for energy storage applications[195–197]. Polyhedral (car)boranes are also good alternatives as closomers[57] for their applications ranging from materials science to medicine.

Among the investigated closo-borane clusters, icosahedral  $[\text{B}_{12}\text{H}_{12}]^{2-}$  and its derivatives have attracted the most attention due to its exceptional stability[55]. In addition to  $[\text{B}_{12}\text{H}_{12}]^{2-}$ , other experimentally confirmed dianionic boranes ( $[\text{B}_n\text{H}_n]^{2-}$ ) such as  $[\text{B}_{10}\text{H}_{10}]^{2-}$ ,  $[\text{B}_{11}\text{H}_{11}]^{2-}$ ,  $[\text{B}_9\text{H}_9]^{2-}$ ,  $[\text{B}_8\text{H}_8]^{2-}$ ,  $[\text{B}_7\text{H}_7]^{2-}$  [4,5,50,51] reveal that these species are stable in their dianionic form. The stability of these clusters can be described by the

Wade-Mingos rules[42–44,198], which indicates that (n+1) skeletal electron pairs are required for a borane molecule to be stable. Von Ragué Schleyer et al.[64] reported that an increase in the cluster size of borane dianions causes a decrease in the coulomb repulsion and results in a large number of multicenter bonding interaction. Thus, the larger closo-boranes such as  $[B_{16}H_{16}]^{2-}$  and  $[B_{17}H_{17}]^{2-}$  were found to be more stable than the smaller ones (n=5-11) according to various parameters, such as the vertex basis PRDDO average energies, the synthesis basis cumulative BH addition energy or disproportionation approach[64].

Despite the predicted stabilities of larger closo-boranes, these systems *have not been realized experimentally* as parent borane clusters. The lack of successfully synthesized  $[B_nH_n]^{2-}$  clusters for n>12 has been attributed to the exceptional stability of icosahedral  $[B_{12}H_{12}]^{2-}$  cluster, which is also referred as *icosahedral barrier*[64]. It should be noted that the icosahedral barrier has been overcome for the cases of carboranes, metallaboranes and metallacarboranes. The first metal-free 13-vertex carborane has been experimentally realized in 2003[66]. Since then, a series of 13- and 14-vertex carboranes have been synthesized and structurally characterized[199,200]. More recently, Zheng et al. have successfully prepared the 15- and 16-vertex carboranes with the introduction of silyl groups to both cage carbons[201]. In the case of metallaboranes and metallacarboranes, several structures beyond the icosahedral barrier have been reported as well[78,202]. We also note that exploration of new synthetic routes and mechanisms for supraicosahedral systems is still an active research area as several theoretically predicted boron-based polyhedral clusters have not been experimentally synthesized yet.

In addition to supraicosahedral clusters, perfunctionalized clusters can provide new applications and synthetic routes for boron cluster chemistry. Different functional groups have been utilized for this purpose such as halogens, hydroxyl, ester, cyanide and amine groups[54,59,203–208], and electron holding ability of the terminal group is shown to be important to obtain stable clusters for borane derivatives[203,204]. More recently, selective functionalization of cage B-H bond in polyhedral boranes and carboranes have become a powerful methodology to synthesize a variety of structures with different functional groups[90,93,95,209]. On the other hand, the effect of perfunctionalization or selective functionalization on the stability and electronic structure of larger borane clusters (n ≥ 13) has not been explored. In that aspect, we performed DFT calculations on a series of polyhedral  $[B_nX_n]^{2-}$  clusters (n=10, 12, 13, 14, 15 and 16) where X denotes H, F, Cl, Br, CN, BO, OH and NH<sub>2</sub> groups and all the results of larger clusters are particularly

given in comparison to  $[B_{12}X_{12}]^{2-}$  counterparts, since this cluster has been the central focus of experimental [55,59,207,210] and theoretical[54,206,208] investigation among the borane clusters. The effect of substitution on geometries, electronic structure, charge distribution and formation enthalpies were investigated for these clusters. The results for the borane systems were also compared to selective carborane clusters in the case of formation enthalpies. We hope that our work can provide useful information in terms of cluster stability and possible reaction paths for target systems.

### 3.2 Computational Details

All DFT calculations were carried out using Gaussian 09[211] package program and Gaussview 5.0[212] was used for the visualization. Geometries were optimized and electronic structures were investigated for varying size of borane clusters and substituted derivatives ( $[B_nX_n]^{2-}$ ,  $n = 10, 12, 13, 14, 15, 16$ ;  $X = H, F, Cl, CN, BO, OH$  and  $NH_2$ ) using PBE0 functional[213,214], which was shown to have a good agreement with the experiment in previous work. 6-311++G\*\* basis set was used for the calculations. General structures and point group symmetries of the parent borane dianions are represented in Figure 3.1.

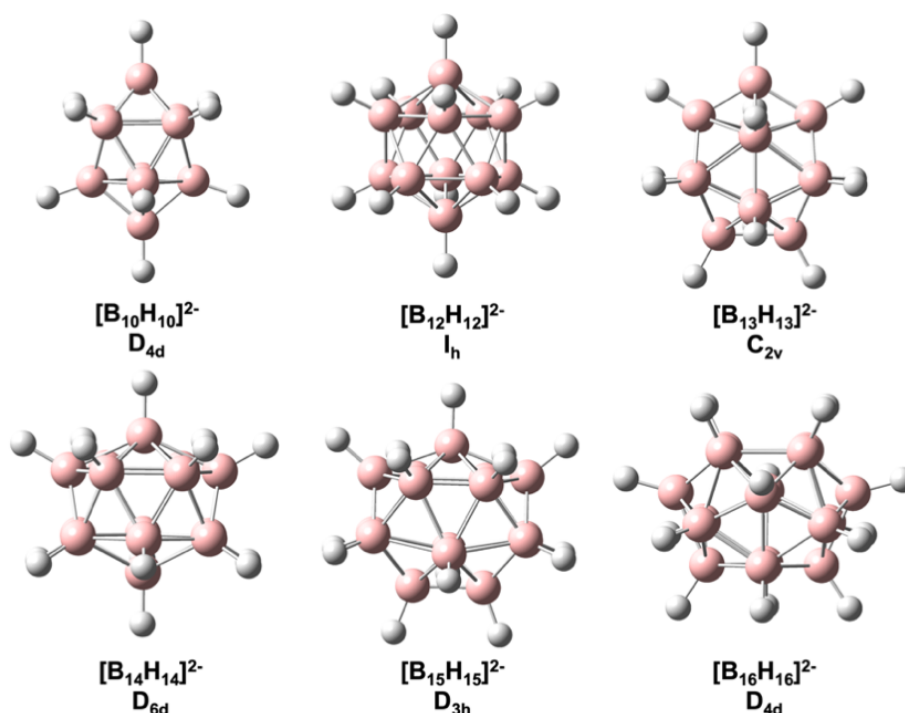
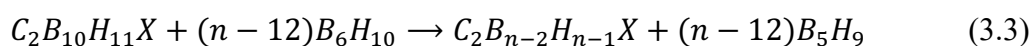
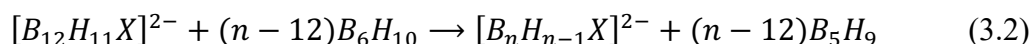
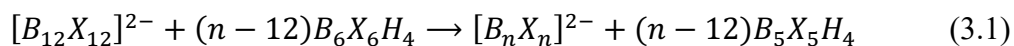


**Figure 3. 1** Structural representation of  $[B_{10}H_{10}]^{2-}$ ,  $[B_{12}H_{12}]^{2-}$ ,  $[B_{13}H_{13}]^{2-}$ ,  $[B_{14}H_{14}]^{2-}$ ,  $[B_{15}H_{15}]^{2-}$  and  $[B_{16}H_{16}]^{2-}$  clusters along with point group symmetries.

Geometry optimizations were followed by the frequency calculation on the same method for the confirmation of the minima on the potential energy surface. As a result of this analysis, there is no negative frequency found which signifies the kinetic stability of the clusters. The vertical and adiabatic detachment energies (VDE and ADE) were determined for the dianions as described in reference 20 with the same level of theory. Benchmark calculations for the electron detachment energies of  $[B_{12}X_{12}]^{2-}$  clusters were also performed using different functionals (GGA (BP86[215,216]), hybrid (B3LYP[217],PBE0[213,214]) and meta-hybrid (M06-2X[172])) to have a clear idea of functional effect on the energies and the results are provided in the supplementary information (SI). Charge distributions on the clusters were computed using electrostatic potential (ESP)-derived method (charges from electrostatic potentials using a grid (CHELPG[218])) and natural population analysis (NPA[219–222]). Due to the diagonalization problem during NPA for  $[B_{12}BO_{12}]^{2-}$  and  $[B_{16}(NH_2)_{16}]^{2-}$  with the 6-311++G\*\* basis set, 6-31G\* was used as for these two clusters.

Reaction enthalpies based on  $-BX$  addition to  $[B_{12}X_{12}]^{2-}$  clusters were calculated and their relation with different substituents as shown in Eq. 1 where  $n=13, 14, 15$  and  $16$ . Moreover, this approach was applied on the transition from 12-vertex to 13- and 14-vertex clusters for singly substituted borane and carborane clusters, as given in Eq 2 and Eq. 3 ( $n=13, 14$ ), respectively.



For the singly substituted clusters, different isomers were considered for the enthalpy calculations while only the results from lowest-energy isomers were reported. These reactions were mainly adapted from the study of Schleyer on the larger boranes[64] and other related studies[223,224]. The PBE0 results for formation enthalpies were also compared to those obtained with B3LYP[217] and M06-2X[172] for benchmark purposes.

## 3.3 Results and Discussion

### 3.3.1 Geometry

In Figure 3.2a, the average bond lengths ( $(B-B)_{avg.}$ ) between the cage boron atoms are shown with respect to different substituent groups. As shown in the figure, transition from 10 or 12-vertex to larger clusters exhibits a significant increase in  $(B-B)_{avg.}$ , and this increase is more pronounced for the lower symmetry 13- and 15- vertex clusters compared to 14- and 16 vertex cases. In case of  $[B_{10}X_{10}]^{2-}$  and  $[B_{12}X_{12}]^{2-}$ ,  $(B-B)_{avg.}$  do not show a significant variation for different substituents, whereas there is a noticeable expansion of the cage structure for larger clusters ( $n \geq 13$ ) upon substitution with the halogen atoms. For these clusters,  $(B-B)_{avg.}$  show a maximum increase of 0.017 Å, 0.021 Å, 0.027 Å and 0.033 Å for 13, 14, 15 and 16-vertex clusters respectively with the substitution of  $X=Br$  compared to the case where  $X=H$ .

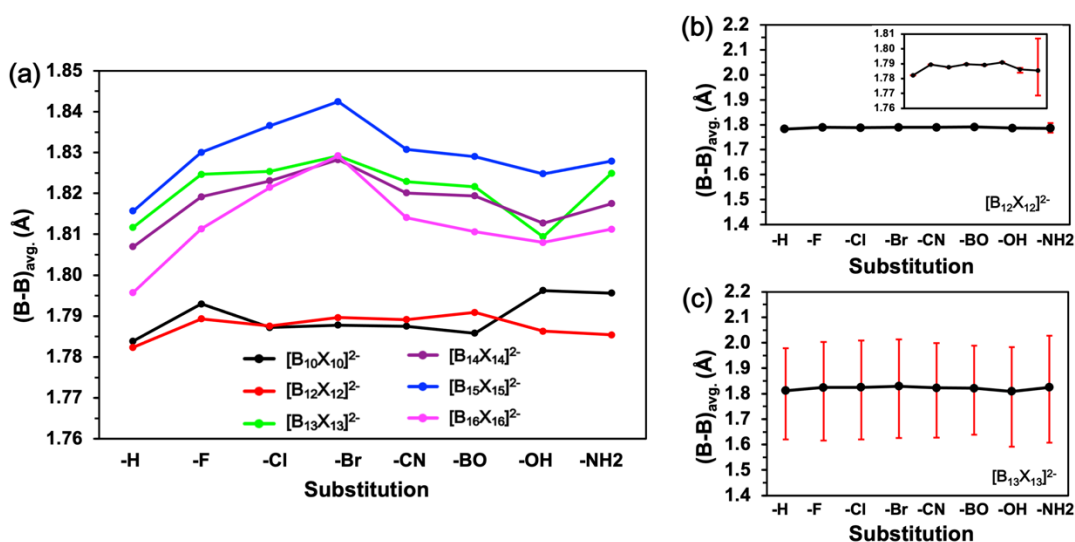


**Figure 3.2** a) The average B-B bond lengths or  $(B-B)_{avg.}$  (Å) for cage boron atoms in  $[B_nX_n]^{2-}$  clusters, and deviations in the  $(B-B)_{avg.}$  for b)  $[B_{12}X_{12}]^{2-}$  and c)  $[B_{13}X_{13}]^{2-}$  with respect to different substitutions.

In the case of  $[B_{12}X_{12}]^{2-}$  clusters exhibit an almost perfect icosahedral ( $I_h$ ) symmetry for single-atom substitutions ( $X=F$ ,  $Cl$  and  $Br$ ) or substitutions with linear geometry ( $X=CN$  and  $BO$ ), whereas the geometries show slight distortions from  $I_h$  symmetry with  $OH$  and  $NH_2$  substitution. The deviations in  $(B-B)_{avg.}$  are calculated to be 0.002 Å and 0.02 Å for  $OH$  and  $NH_2$  respectively as illustrated in Figure 3.2b. In contrast to  $[B_{12}X_{12}]^{2-}$ , different substitutions generally show similar deviations for the  $(B-B)_{avg.}$  of larger clusters (Figure 3.3), especially for the cases with lower point group symmetries

such as  $[B_{13}X_{13}]^{2-}$  as illustrated in Figure 3.2c. For  $[B_{14}X_{14}]^{2-}$  and  $[B_{16}X_{16}]^{2-}$ , the calculated deviations for the  $(B-B)_{\text{avg}}$  show a slight increase with OH and  $NH_2$  substitution similar to the case in  $[B_{12}X_{12}]^{2-}$ .

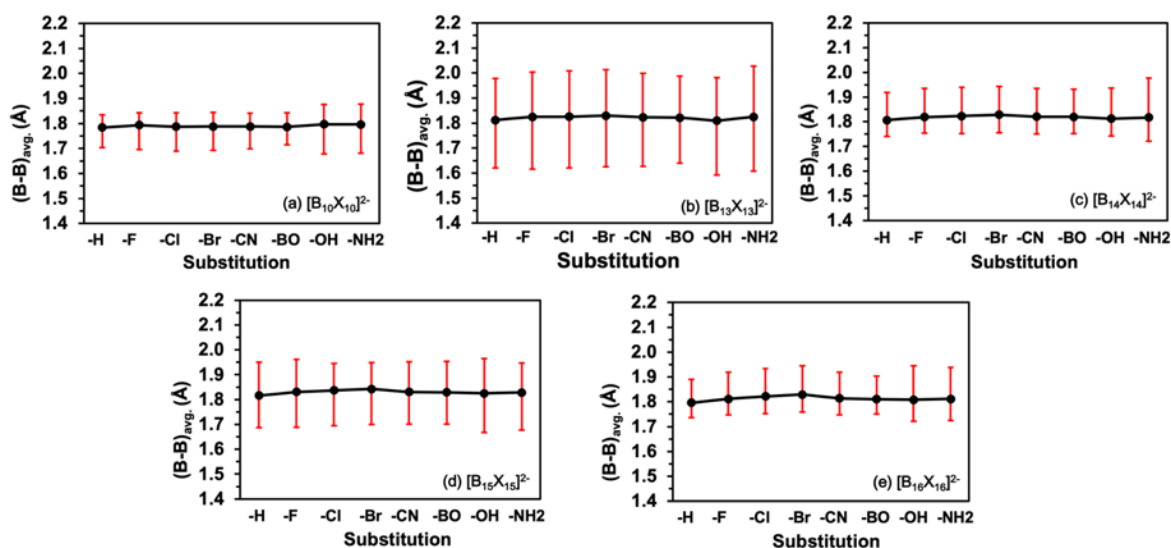


**Figure 3.3** Deviations in  $(B-B)_{\text{avg}}$  length depending on the substitution for a)  $[B_{10}X_{10}]^{2-}$ , b)  $[B_{13}X_{13}]^{2-}$ , c)  $[B_{14}X_{14}]^{2-}$ , d)  $[B_{15}X_{15}]^{2-}$  and e)  $[B_{16}X_{16}]^{2-}$  clusters.

### 3.3.2 Electronic Structure

Figure 3.4a-f show the pictorial representation of frontier orbitals along with their energies for different substituents of the investigated systems. As seen from the figure, the energetics of frontier orbitals show a similar trend for all dianion clusters, except for the case of Br substitution. For halogen substitution, both HOMO and LUMO levels of 10, 12, 13 and 15-vertex clusters exhibit a monotonic stabilization from F to Br as a result of -I (inductive) effects on the boron cage. In the case of  $[B_{14}Br_{14}]^{2-}$  and  $[B_{16}Br_{16}]^{2-}$  dianions, however, this trend is broken for  $X=Br$ , as the HOMO levels of these larger boranes are destabilized with respect to the case in Cl substitution. The population analysis for the HOMO levels reveals that only p orbitals of Br contribute to the HOMO of  $[B_{14}Br_{14}]^{2-}$  and  $[B_{16}Br_{16}]^{2-}$  clusters, while significant contribution from p orbitals of boron cage appears for the HOMOs in the case of  $X=Cl$  or F. The lack of mixing between Br and B orbitals most likely originates from the energy difference ( $\Delta E$ ) parameter between these levels. On the other hand, there is significant mixing predicted between Br and B orbitals for the LUMO level, resulting in the stabilization of this level for  $[B_{14}Br_{14}]^{2-}$  and  $[B_{16}Br_{16}]^{2-}$  clusters as expected. We note that a similar destabilization in the HOMO



level for halogen substitution was reported previously[59] for  $[B_{12}X_{12}]^{2-}$  clusters as well, however, the monotonic trend was shown to be broken for  $X=I$  in this case instead of  $X=Br$  found for larger cluster series in this study.

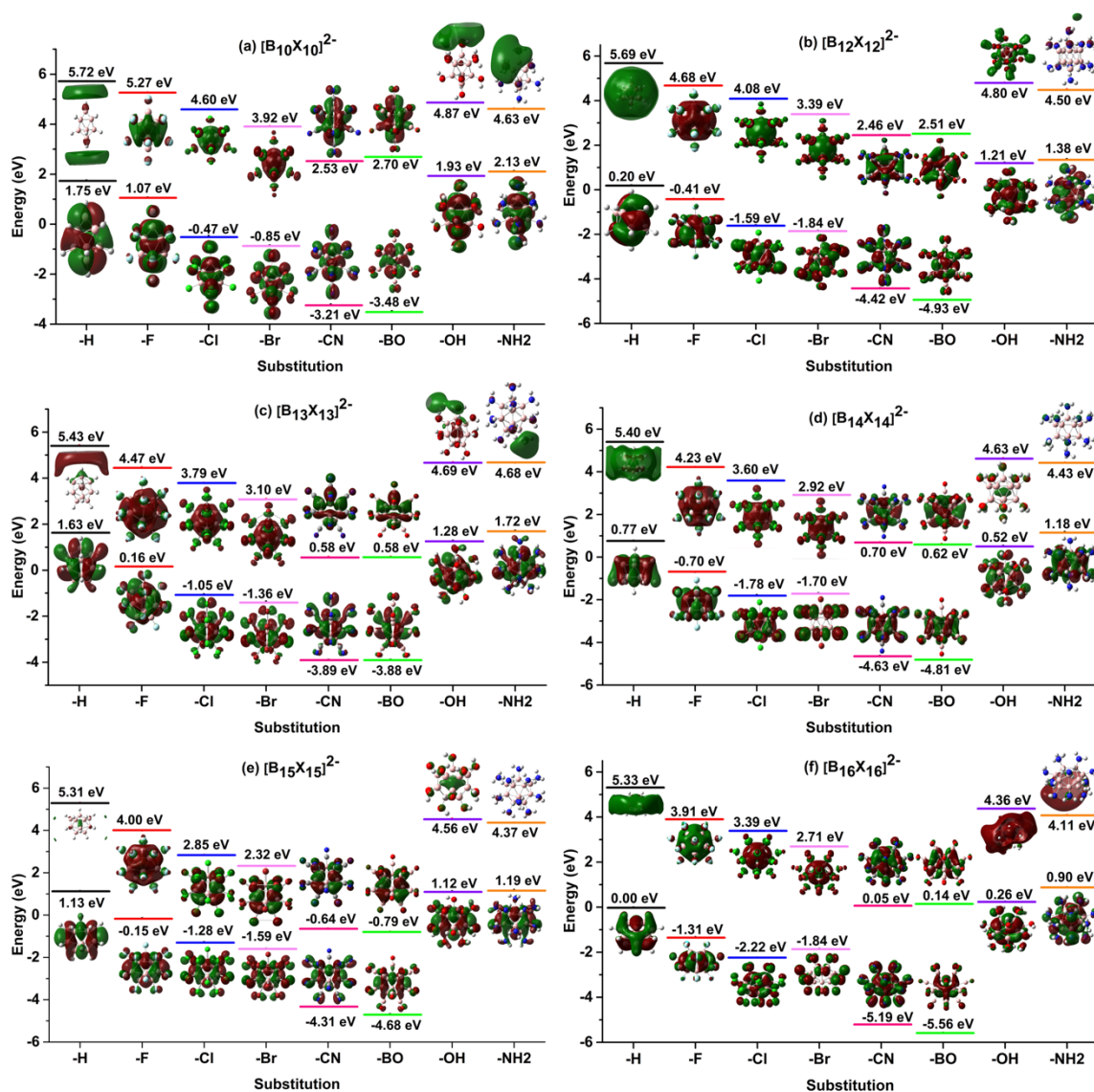


**Figure 3.4** HOMO-LUMO levels of (a)  $[B_{10}X_{10}]^{2-}$ , (b)  $[B_{12}X_{12}]^{2-}$ , (c)  $[B_{13}X_{13}]^{2-}$ , (d)  $[B_{14}X_{14}]^{2-}$ , (e)  $[B_{15}X_{15}]^{2-}$  and (f)  $[B_{16}X_{16}]^{2-}$  clusters calculated with PBE0/6-311++G\*\*.

In all cases of clusters regardless to their size or symmetry, the highest stabilization for both HOMO and LUMO levels is seen for the cases of isoelectronic BO and CN substitution, as a result of large -M (mesomeric) effect on the boron cage. Interestingly, this stabilization appears to be higher in amount than that of  $[B_{12}X_{12}]^{2-}$  for all the others. In comparison, OH substitution generally exhibits a large destabilization for HOMO and LUMO levels as a result of +M effect. It should be noted that the substituent effects on

HOMO and LUMO energies of all clusters largely resemble the mesomeric ( $\pm M$ ) and inductive ( $\pm I$ ) effects observed in  $\pi$ -conjugated systems[225–227] as illustrated in Figure 3.5 for the 9, 10-substitution of anthracene. In that regard, we expect that substitution effects on boron-containing clusters should generally follow the trends that are obtained for a large set of  $\pi$ -conjugated systems in the literature.

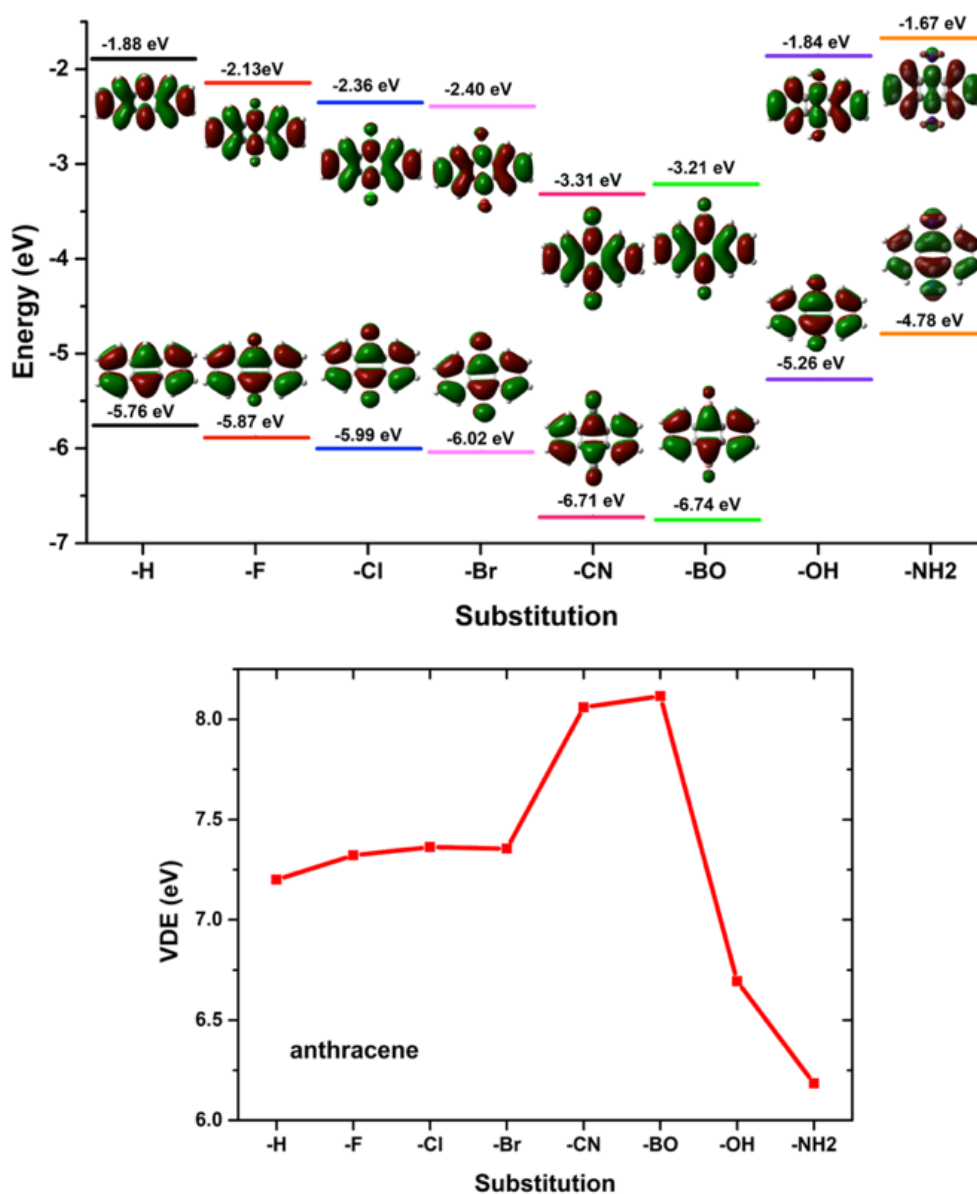


**Figure 3.5** a) HOMO-LUMO levels with pictorial representation of orbitals and, b) VDEs of 9, 10-substituted anthracene  $C_{14}H_8X_2$  ( $X= H, F, Cl, Br, CN, BO, OH$  and  $NH_2$ ) calculated with PBE0/6-311++G\*\*

For the investigated systems, the positive HOMO energies can be interpreted to indicate unstable charge for the dianion clusters, while this can also be a result of the

employed theoretical methodology. For instance, the positive HOMO energy of the  $[B_{12}H_{12}]^{2-}$  molecule in the gas phase, which was proven to be stable[55], is shown to be slightly positive with PBE0 functional while the same HOMO energy is determined to be negative with M06-2X functional. It should be noted that the percentage of exact Hartree-Fock (HF) exchange in the level of theory can be significant for such predictions as illustrated for  $[B_{12}H_{12}]^{2-}$  in Figure 3.6. In comparison, *hypercloso*- $[B_{12}OH_{12}]$  was found to have a positive reduction potential in solution, while it was also reported that the electronic stability decreases upon substitution with the hydroxyl group compared to the case with other functional groups[208]. As for the stability in the gas phase, it is quite clear that  $[B_{12}(OH)_{12}]^{2-}$  or  $[B_{12}(NH_2)_{12}]^{2-}$  molecules with significantly higher HOMO values, is most likely not electronically stable, which is supported by the negative adiabatic electron detachment energies (ADEs) as well (*vide infra*). We also note that the energy of the frontier orbitals for the case of OH or  $NH_2$  substitution monotonically decrease with the cluster size for even numbered clusters. In fact, the difference in the energy of HOMO between  $[B_{12}H_{12}]^{2-}$  and  $[B_{12}OH_{12}]^{2-}$  is predicted to be 1.01 eV whereas the same difference in the case of  $[B_{16}X_{16}]^{2-}$  is only 0.26 eV. Interestingly, for  $[B_{13}X_{13}]^{2-}$  and  $[B_{14}X_{14}]^{2-}$ , HOMO even becomes more stable for the case of OH substitution compared to the case where  $X=H$ . This is most likely the result of the fact that large +M effects induced by OH or  $NH_2$  groups, which increase the  $\pi$  electron density on the boron cage significantly, can be compensated more easily in the case of larger clusters.

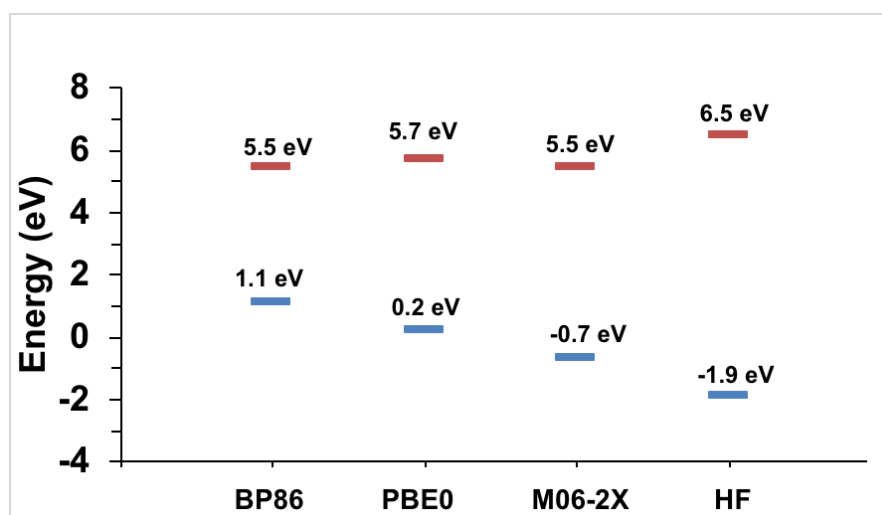


**Figure 3.6** Comparison of HOMO and LUMO levels for  $[B_{12}H_{12}]^{2-}$  cluster calculated with different density functionals of varying exact exchange along with Hartree-Fock (HF) theory.

In addition to the electronic structure, both VDEs and ADEs were calculated with different DFT functionals, and the results were given in Table 3.1 and 3.2 for  $[B_{12}X_{12}]^{2-}$  clusters, respectively.

**Table 3. 1** Vertical detachment energies (VDEs) in eV calculated at different levels of theory for  $[B_{12}X_{12}]^{2-}$  (The values in the parenthesis are VDE values with Zero Point Energy (ZPE) correction)

	<b>BP86</b>	<b>B3LYP</b>	<b>PBE0</b>	<b>M06-2X</b>
$[B_{12}H_{12}]^{2-}$	1.17 (1.03)	1.21 (1.07)	1.28 (1.14)	1.45 (1.31)
$[B_{12}F_{12}]^{2-}$	1.46 (1.37)	1.97 (1.88)	2.01 (1.92)	2.38 (2.29)
$[B_{12}Cl_{12}]^{2-}$	2.28 (2.20)	2.72 (2.64)	2.79 (2.71)	3.25 (3.16)
$[B_{12}Br_{12}]^{2-}$	2.43 (2.35)	2.85 (2.76)	2.94 (2.85)	3.46 (3.38)
$[B_{12}(CN)_{12}]^{2-}$	4.98 (4.84)	5.44 (5.30)	5.56 (5.42)	6.08 (5.94)
$[B_{12}(BO)_{12}]^{2-}$	5.24 (5.09)	5.91 (5.75)	6.07 (5.92)	6.71 (6.55)
$[B_{12}(OH)_{12}]^{2-}$	-0.22 (-0.26)	0.17 (0.13)	0.17 (0.13)	0.53 (0.49)
$[B_{12}(NH_2)_{12}]^{2-}$	-0.47 (-0.51)	-0.16 (-0.20)	-0.15 (-0.19)	0.21 (0.18)

**Table 3.2** Adiabatic detachment energies (ADEs) in eV calculated at different levels of theory for  $[B_{12}X_{12}]^{2-}$  (The values in the parenthesis are ADE values with ZPE correction)

	<b>BP86</b>	<b>B3LYP</b>	<b>PBE0</b>	<b>M06-2X</b>
$[B_{12}H_{12}]^{2-}$	0.83 (0.69)	0.92 (0.78)	0.96 (0.81)	1.12 (0.98)
$[B_{12}F_{12}]^{2-}$	1.31 (1.22)	1.64 (1.55)	1.62 (1.53)	1.99 (1.90)
$[B_{12}Cl_{12}]^{2-}$	2.21 (2.12)	2.58 (2.50)	2.59 (2.50)	3.05 (2.97)
$[B_{12}Br_{12}]^{2-}$	2.38 (2.30)	2.78 (2.70)	2.80 (2.72)	3.32 (3.24)
$[B_{12}(CN)_{12}]^{2-}$	4.87 (4.73)	5.33 (5.19)	5.46 (5.32)	6.01 (5.87)
$[B_{12}(BO)_{12}]^{2-}$	5.24 (5.21)	5.91 (5.75)	6.07 (5.92)	6.71 (6.55)
$[B_{12}(OH)_{12}]^{2-}$	-0.50 (-0.54)	-0.34 (-0.38)	-0.31 (-0.35)	0.03 (-0.01)
$[B_{12}(NH_2)_{12}]^{2-}$	-0.92 (-0.95)	-0.77 (-0.81)	-0.75 (-0.78)	-0.36 (-0.40)

PBE0 functional which was recommended by previous studies[55,206] as a cost-effective alternative to CCSD(T) method was used as reference method in this study. Note that this functional was shown to yield reliable results for VDEs of H and F substituents, but it underestimates the VDE values for Cl and Br substituted dianions[55,59]. It should also be mentioned that the BP86 functional with no exact HF exchange highly underestimates the VDEs compared to the case with PBE0, while approximate results were obtained with B3LYP as expected, which has similar HF exchange contribution. On the other hand, M06-2X overestimates the VDEs due to the high ratio of HF exchange in

the functional. The VDEs given in Figure 3.7 show a quite similar trend for all cluster sizes, except for the Br substituent. Unlike the others, VDE value of  $[\text{B}_{14}\text{Br}_{14}]^{2-}$  and  $[\text{B}_{16}\text{Br}_{16}]^{2-}$  is lower than those of Cl substituted ones. Notice that a similar discrepancy between 14- and 16-vertex clusters and the others has been found for the HOMO levels as well. Both results account for a decrease in the electronic stability in  $[\text{B}_{14}\text{Br}_{14}]^{2-}$  and  $[\text{B}_{16}\text{Br}_{16}]^{2-}$ , which is due to the lack of mixing between Br and B p orbitals. Since VDE is a parameter which is directly related to the electronic stability of the molecule, it can be said that the highest stability for  $[\text{B}_n\text{X}_n]^{2-}$  dianions was found for the BO substituent followed by CN substituent, as also stated for  $[\text{B}_{12}\text{X}_{12}]^{2-}$  clusters in previous studies[54,206]. Figure 3.7 also shows that the energy required to eject an electron from the dianions is not directly related to the cluster size. VDEs of only  $[\text{B}_{16}\text{X}_{16}]^{2-}$  and some derivatives of  $[\text{B}_{14}\text{X}_{14}]^{2-}$  lie above the icosahedral boron cluster, which may indicate higher stability for these clusters.

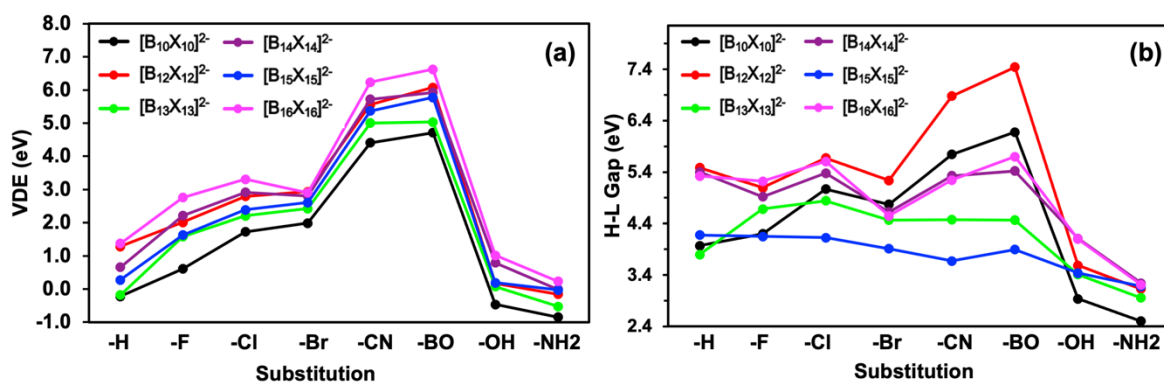


**Figure 3.7** Comparison of calculated (a) VDE values and (b) H-L gaps for the clusters with different substituents using PBE0/6-311++G\*\* level of theory.

### 3.3.3 Reaction Energies

In addition to the electronic structure analysis, we have performed an investigation for the formation enthalpies ( $\Delta H_{\text{add}}$ ) of larger borane clusters from icosahedral  $[\text{B}_{12}\text{X}_{12}]^{2-}$  with a focus on the effect of substitution on icosahedral barrier. The single step reaction has been adapted from the seminal work of Schleyer et al.[64], which has been employed in following studies investigating borane and carborane clusters[223,224]. The results for the  $[\text{B}_n\text{X}_n]^{2-}$  are summarized for PBE0/6-311++G\*\* level of theory, and the same values are also tabulated for B3LYP and M06-2X for comparison in Table 3.3. We note that while calculated  $\Delta H_{\text{add}}$  with PBE0 and M06-2X functionals show a good agreement,

$\Delta H_{\text{add}}$  values obtained with B3LYP are somewhat larger, especially for the cases of  $n=15$  and 16. In comparison, all functionals yield similar trends with respect to the substitution effect on the  $\Delta H_{\text{add}}$ .

**Table 3.3** Calculated formation enthalpies ( $\Delta H_{\text{add}}$ )\* of perfunctionalized borane clusters,  $[\text{B}_n\text{X}_n]^{2-}$ , from icosahedral  $[\text{B}_{12}\text{X}_{12}]^{2-}$  with different level of theories

Clusters	$\Delta H$ (kcal/mol)							
	H	F	Cl	Br	CN	BO	OH	NH <sub>2</sub>
<u>PBE0/6-311++G**</u>								
$[\text{B}_{13}\text{X}_{13}]^{2-}$	42.33	46.06	53.43	56.12	46.53	40.37	35.10	27.01
$[\text{B}_{14}\text{X}_{14}]^{2-}$	3.43	17.70	26.92	32.33	13.26	3.35	3.01	-15.62
$[\text{B}_{15}\text{X}_{15}]^{2-}$	3.72	31.03	44.12	52.73	20.65	3.87	24.26	-23.84
$[\text{B}_{16}\text{X}_{16}]^{2-}$	-16.02	20.62	39.10	52.00	9.57	-14.46	22.60	-41.97
<u>B3LYP/6-311++G**</u>								
$[\text{B}_{13}\text{X}_{13}]^{2-}$	43.67	46.50	54.60	57.47	48.32	42.69	30.98	16.20
$[\text{B}_{14}\text{X}_{14}]^{2-}$	10.20	24.00	34.20	40.27	21.15	11.66	0.09	-32.02
$[\text{B}_{15}\text{X}_{15}]^{2-}$	14.13	40.38	55.38	65.01	32.67	16.52	19.45	-48.03
$[\text{B}_{16}\text{X}_{16}]^{2-}$	-2.82	32.62	53.78	68.06	25.14	2.17	15.93	-74.12
<u>M06-2X/6-311++G**</u>								
$[\text{B}_{13}\text{X}_{13}]^{2-}$	44.72	46.20	56.57	60.19	48.50	42.75	33.76	23.37
$[\text{B}_{14}\text{X}_{14}]^{2-}$	4.11	17.33	27.72	33.91	12.10	2.33	-3.67	-28.75
$[\text{B}_{15}\text{X}_{15}]^{2-}$	4.24	30.04	44.93	54.98	18.46	2.03	14.08	-44.10
$[\text{B}_{16}\text{X}_{16}]^{2-}$	-15.79	18.44	39.37	53.50	5.56	-17.81	9.03	-68.71

\* The  $\Delta H_{\text{add}}$  values are calculated based on the addition reaction  $[\text{B}_{12}\text{X}_{12}]^{2-} + (n-12)\text{B}_6\text{X}_6\text{H}_4 \rightarrow [\text{B}_n\text{X}_n]^{2-} + (n-12)\text{B}_5\text{X}_5\text{H}_4$  where  $n=13, 14, 15$  and 16.

As shown by Schleyer et al.[64] and later confirmed in other works[223], there is a large gain in stability for the formation of  $[\text{B}_{12}\text{H}_{12}]^{2-}$  cluster with respect to neighboring clusters in size. This is also seen in our investigation as the calculated  $\Delta H_{\text{add}}$  for  $[\text{B}_{13}\text{H}_{13}]^{2-}$  cluster is quite large (42.33 kcal/mol), while  $\Delta H_{\text{add}}$  for the formation of  $[\text{B}_{12}\text{H}_{12}]^{2-}$  from  $[\text{B}_{10}\text{H}_{10}]^{2-}$  is calculated to be -91.45 kcal/mol. This exceptional stability of  $[\text{B}_{12}\text{H}_{12}]^{2-}$  is often associated with the icosahedral barrier. We note that icosahedral barrier in this context does not refer to an actual energy barrier between two minima and the transition state, however, one should still expect a large energy barrier for the formation of  $[\text{B}_{13}\text{H}_{13}]^{2-}$  from  $[\text{B}_{12}\text{H}_{12}]^{2-}$  as a result of Hammond's postulate. The  $\Delta H_{\text{add}}$  values are also positive for  $n=14$  and 15 cases, whereas it finally becomes negative for the case of  $[\text{B}_{16}\text{H}_{16}]^{2-}$ , which is also in agreement with the previous work[64]. To understand the effect of substitution more clearly, we illustrated the change in calculated  $\Delta H_{\text{add}}$  for each

cluster relative to the case where X=H respectively in Figure 3.8a. For all clusters, it is seen that the energy barrier becomes larger with the halogen substitution with an increasing trend as F→Cl→Br. The larger energy barriers are also obtained for X=CN cases with respect to X=H, however, calculated  $\Delta H_{\text{add}}$  are not as large as the halogen substitution for almost all cases. A further reduction is seen with BO substitution, which shows very similar results with the unsubstituted borane clusters for the calculated  $\Delta H_{\text{add}}$ . These results are most likely related to the increasing -M effect with CN and BO substitution compared to the halogens. In comparison, the most intriguing results are obtained for the energy barriers when *substituents with strong +M effects* are introduced. In the case of OH substitution,  $\Delta H_{\text{add}}$  is reduced by  $\sim 7$  kcal/mol compared to the X=H case for  $[\text{B}_{13}\text{X}_{13}]^{2-}$ , whereas this reduction further increases to  $\sim 15$  kcal/mol with  $\text{NH}_2$  substitution. For larger clusters such as  $[\text{B}_{15}\text{X}_{15}]^{2-}$  and  $[\text{B}_{16}\text{X}_{16}]^{2-}$ , however, OH substitution shows an increase in the  $\Delta H_{\text{add}}$  whereas  $\text{NH}_2$  substitution still shows substantial decrease in the calculated  $\Delta H_{\text{add}}$  compared to the case where X=H, which most likely results from stronger +M effects of  $\text{NH}_2$  group.

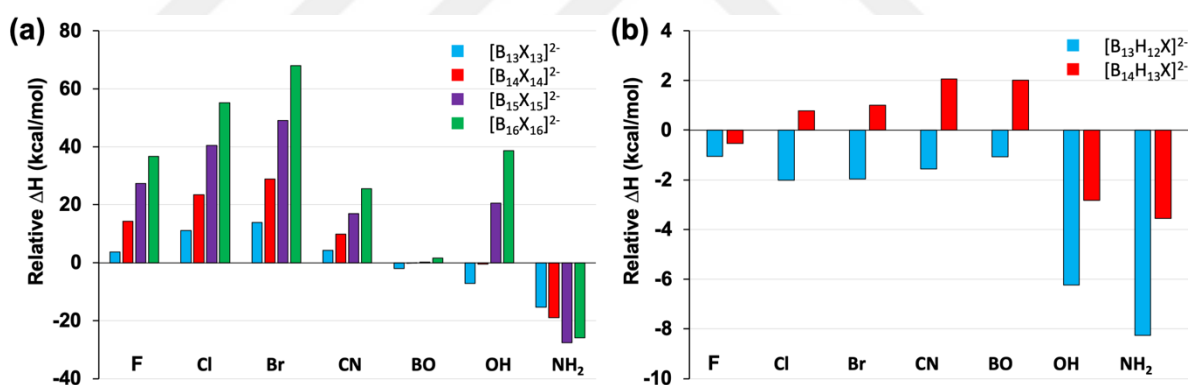


**Figure 3.8 a)** Calculated relative  $\Delta H_{\text{add}}$  values for the formation of perfunctionalized boron clusters based on the reaction  $[\text{B}_{12}\text{X}_{12}]^{2-} + (n-12)\text{B}_6\text{X}_6\text{H}_4 \rightarrow [\text{B}_n\text{X}_n]^{2-} + (n-12)\text{B}_5\text{X}_5\text{H}_4$  ( $n=13, 14, 15$  and  $16$ ), and **b)** calculated relative  $\Delta H_{\text{add}}$  values for the formation of single-substituted boron clusters based on the reaction  $[\text{B}_{12}\text{H}_{11}\text{X}]^{2-} + (n-12)\text{B}_6\text{H}_{10} \rightarrow [\text{B}_n\text{H}_{n-1}\text{X}]^{2-} + (n-12)\text{B}_5\text{H}_9$  ( $n=13$  and  $14$ ). For all substitution,  $\Delta H_{\text{add}}$  are scaled relative to the case where X=H. All values are obtained with PBE0/ 6-311++G\*\* level of theory.

In order to evaluate the effect of single substitution instead of perfunctionalization,  $\Delta H_{\text{add}}$  was also calculated for the formation of 13- and 14-vertex clusters based on the addition reaction (Eq. 2). As shown in Figure 3.8b and Table 3.4, single substitution for

the 13-vertex cluster exhibits quite different results for the calculated  $\Delta H_{\text{add}}$  compared to the case of perfunctionalization. For the single substitution of 13-vertex cluster, all functional groups result in lowering the  $\Delta H_{\text{add}}$  values compared to the non-substituted case. This result most likely originates from the reduced symmetries in the case of single-substituted clusters. We note that  $[\text{B}_{12}\text{H}_{12}]^{2-}$  cluster exhibits the *highest symmetry* ( $I_h$  point group) whereas  $[\text{B}_{13}\text{H}_{13}]^{2-}$  exhibits the *lowest symmetry* ( $C_{2v}$  point group) among the investigated systems (Figure 3.1). This is also the case for the perfunctionalized clusters except for OH and  $\text{NH}_2$  substitution as discussed previously (Figure 3.2). For this reason, the effect of reduced symmetry on the stability of the clusters is expected to be largest for the 12-vertex cluster, while it is expected to be lowest for the 13-vertex cluster. It should also be noted that while there is a reduction in the icosahedral barrier for all single-substituted systems of  $[\text{B}_{13}\text{H}_{12}\text{X}]^{2-}$ , this reduction is further pronounced for OH and  $\text{NH}_2$  substitution due to strong +M effects as expected from the results of perfunctionalized systems. In the case of  $[\text{B}_{14}\text{H}_{13}\text{X}]^{2-}$ , the effect of reduced symmetry on the stabilities of the parent  $[\text{B}_{12}\text{H}_{12}]^{2-}$  ( $I_h$  point group) and  $[\text{B}_{14}\text{H}_{14}]^{2-}$  ( $D_{6d}$  point group) clusters are expected to be similar as both clusters are highly symmetric. In this case, icosahedral barrier is *still reduced* with OH and  $\text{NH}_2$  substitution as a result of electronic effects, while Cl, Br, CN and BO substitution shows an increase in the  $\Delta H_{\text{add}}$  values compared to non-substituted clusters.



**Table 3.4** Calculated formation enthalpies ( $\Delta H_{\text{add.}}$ )<sup>\*</sup> of  $[\text{B}_n\text{H}_{n-1}\text{X}]^{2-}$  clusters from icosahedral  $[\text{B}_{12}\text{H}_{11}\text{X}]^{2-}$ 

Clusters	$\Delta H$ (kcal/mol)							
	H	F	Cl	Br	CN	BO	OH	NH <sub>2</sub>
<u>PBE0/6-311++G**</u>								
$[\text{B}_{13}\text{H}_{12}\text{X}]^{2-}$	42.33	41.27	40.32	40.37	40.77	41.26	36.09	34.07
$[\text{B}_{14}\text{H}_{13}\text{X}]^{2-}$	3.43	2.90	4.21	4.44	5.49	5.44	0.61	-0.12
<u>B3LYP /6-311++G**</u>								
$[\text{B}_{13}\text{H}_{12}\text{X}]^{2-}$	43.67	42.42	41.27	41.19	41.91	42.45	37.29	35.25
$[\text{B}_{14}\text{H}_{13}\text{X}]^{2-}$	10.20	9.66	11.03	11.24	12.34	12.34	7.46	6.73
<u>M06-2X/6-311++G**</u>								
$[\text{B}_{13}\text{H}_{12}\text{X}]^{2-}$	44.72	43.65	43.14	43.39	43.74	44.23	38.67	36.83
$[\text{B}_{14}\text{H}_{13}\text{X}]^{2-}$	4.11	3.74	4.98	5.35	6.30	6.34	1.57	0.95

\* The  $\Delta H_{\text{add.}}$  Values are calculated based on the addition reaction  $[\text{B}_{12}\text{H}_{11}\text{X}]^{2-} + (n-12)\text{B}_6\text{H}_{10} \rightarrow [\text{B}_n\text{H}_{n-1}\text{X}]^{2-} + (n-12)\text{B}_5\text{H}_9$  where  $n=13, 14$ .

**Table 3.5** Calculated formation enthalpies ( $\Delta H_{\text{add.}}$ )<sup>\*</sup> of  $[\text{C}_2\text{B}_{n-1}\text{H}_{n-2}\text{X}]^{2-}$  clusters from icosahedral  $[\text{C}_2\text{B}_{10}\text{H}_{11}\text{X}]^{2-}$  using PBE0

Clusters	$\Delta H$ (kcal/mol)							
	H	F	Cl	Br	CN	BO	OH	NH <sub>2</sub>
$[\text{C}_2\text{B}_{11}\text{H}_{12}\text{X}]^{2-}$	31.17	30.40	30.19	29.81	29.51	29.30	28.74	27.68
$[\text{C}_2\text{B}_{12}\text{H}_{13}\text{X}]^{2-}$	17.70	16.20	16.95	17.15	17.97	18.58	13.84	14.68

\* The  $\Delta H_{\text{add.}}$  Values are calculated based on the addition reaction  $[\text{C}_2\text{B}_{12}\text{H}_{11}\text{X}]^{2-} + (n-12)\text{B}_6\text{H}_{10} \rightarrow [\text{C}_2\text{B}_{n-2}\text{H}_{n-1}\text{X}]^{2-} + (n-12)\text{B}_5\text{H}_9$  where  $n=13$  and  $14$ . X is bonded the boron atom which is the neighbor of two C atoms.

In addition to borane clusters, we also explored the effect of single substitution on the formation of 13- and 14-vertex carborane clusters in a similar manner as shown in Figure 3.9 and Table 3.5. We note that the icosahedral barrier is also present for carboranes, however, it is calculated to be substantially lower compared to the case in borane clusters[223]. As shown in Figure 3.9, the effect of single substitution on the energetics of icosahedral barrier for carboranes also follows a similar trend compared the case of boranes (Figure 3.8b). For carboranes, however, the reduction in the barrier with OH and NH<sub>2</sub> substitution is not as high, which most likely results from the fact that the symmetry is already reduced for the parent  $\text{C}_2\text{B}_{10}\text{H}_{12}$  cluster compared to  $[\text{B}_{12}\text{H}_{12}]^{2-}$ . In general, our findings indicate that both symmetry and electronic effects can play an important role in reducing the icosahedral barrier for the investigated systems. As mentioned earlier, this barrier mainly originates from exceptional stability of 12-vertex

cluster clusters. Through substitution, it can be substantially reduced, especially for the 12-vertex to 13-vertex transition, by *destabilizing the 12-vertex clusters* with functional groups exhibiting *strong +M effects*, and *reducing the symmetry* with bulky ligands.

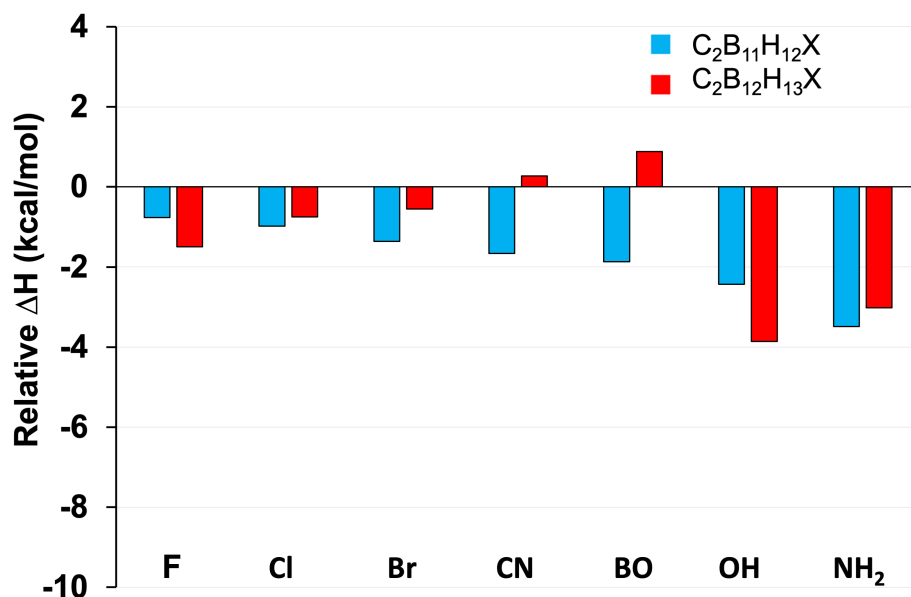


**Figure 3.9** Calculated relative  $\Delta H_{\text{add}}$  values for the formation of single-substituted carborene clusters based on the reaction  $C_2B_{10}H_{11}X + (n-12)B_6X_6H_4 \rightarrow C_2B_{n-2}H_{n-1}X + (n-12)B_5X_5H_4$  ( $n=13, 14$ ). For all substitution,  $\Delta H_{\text{add}}$  are scaled relative to the case where  $X=H$ . All values are obtained with PBE0/ 6-311++G\*\* level of theory.

### 3.3.4 Population Analysis

Charge distribution through the clusters can provide a deeper understanding about where the electron loss is occurred from, and how the stabilities are connected to the charge distribution. Therefore, we utilized two methods to obtain the atomic partial charges: NPA and CHELPG. While the NPA charge is derived from the summation over all-natural atomic orbitals (NAOs) of a given atom, the atomic charges are fitted to reproduce the molecular electrostatic potential (MEP) at a number of points around the molecule in the latter method[218,222]. NPA and CHELPG charges are represented as the summed-up charges for equivalent atoms in the core and surrounding substituent regions in Figure 3.10 and Figure 3.11, respectively.

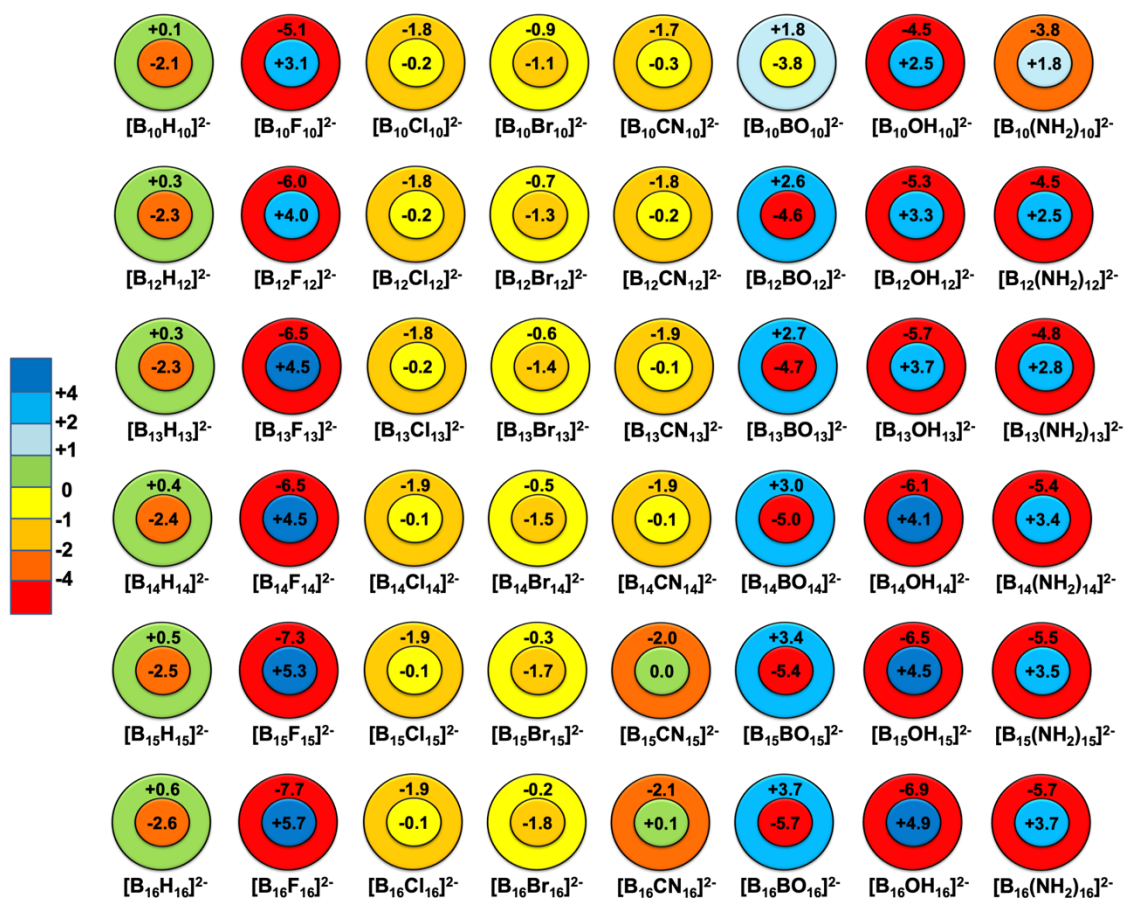


**Figure 3.10** Schematic representation of the NPA charge distribution in the dianions in terms of an inner core ( $B_{10}/B_{12}/B_{13}/B_{14}/B_{15}/B_{16}$ ) and an outer shell ( $X_{10}/X_{12}/X_{13}/X_{14}/X_{15}/X_{16}$ ). The same charge distribution with CHELPG method is illustrated in Figure 3.11.

Although the magnitudes of the charges vary depending on the population analysis method, both give similar results for all clusters except the ones with  $X=H$ . Unlike for other derivatives, NPA and CHELPG methods give opposite results for all dianions for this case as the negative partial charges appear on B atoms, and H atoms have positive partial charges with the NPA method, whereas the opposite is true in the case of CHELPG method. This discrepancy has also been previously reported for (car)borane studies[55,228]. Even though there is still a debate on the reliability of population methods for the calculated H partial charges in (car)boranes, CHELPG method is likely to produce a more accurate description, since the electronegativity difference between B and H, as well as the previous experimental evidence[228–233], suggest more negative H atoms and more positive B atoms for these systems.

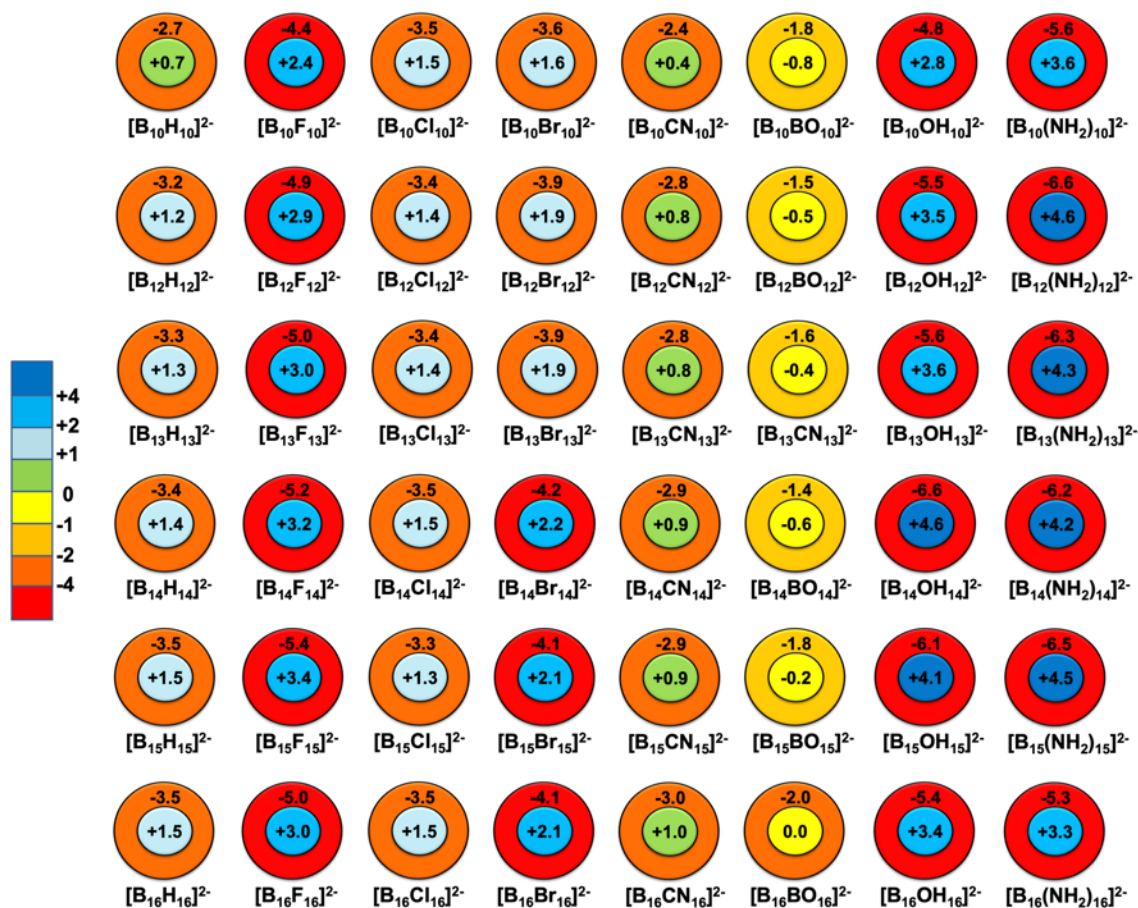


**Figure 3.11** Schematic representation of the ESP (CHELPG) charge distribution the dianions in terms of an inner core (B<sub>10</sub>/B<sub>12</sub>/B<sub>13</sub>/B<sub>14</sub>/B<sub>15</sub>/B<sub>16</sub>) and an outer shell (X<sub>10</sub>/X<sub>12</sub>/X<sub>13</sub>/X<sub>14</sub>/X<sub>15</sub>/X<sub>16</sub>).

For all fluorinated clusters, the boron cage is positively charged while surrounded by the highly negative F substituent shell, and it becomes much more positive with increasing cluster size. Switching to the less electronegative Cl substituent, the shell regions of the clusters are still more negative than the core part, but the differences between two regions are less than the F substitution, and the substituents seem not to have a considerable effect on the charge distribution. With the Br substituent, the charges are more uniformly distributed throughout the smaller dianions and the charge difference between inner and outer shells are small, while boron cage appears to become more negative region unlike the case in X=Cl and X=F, with an increasing strength via increasing cluster size. In the previous work with halogen-substituted [B<sub>12</sub>X<sub>12</sub>]<sup>2-</sup> clusters, Warneke et. al[59], showed that the electron detachment, which is determined by the HOMO position, occurs from the more positively charged region of the molecule. As a result, a decrease in the stability of the clusters for X=I and X=At substituents was shown

to originate from the fact that HOMO level mainly originates from the electrons of the substituent with significant reduction in the contribution of the core atoms. This is also the case in stability of  $[B_{14}Br_{14}]^{2-}$  and  $[B_{16}Br_{16}]^{2-}$  in this study, which was predicted to exhibit a more negative core compared to the substituent shell. For diatomic substituents, the charge on the boron cage also depends on the electronegativity of the atom which is directly bonded to the cage. For  $X=CN$ , the total partial charge on the boron cage in all clusters is quite small, while very positive and very negative charges are predicted for  $X=OH/NH_2$  and  $X=BO$  cases respectively.

### 3.4 Conclusions

In this work, we have performed a benchmark study for the electronic structure and relative stability of  $[B_nX_n]^{2-}$  clusters ( $X=H, F, Cl, Br, CN, BO, OH, NH_2$ ) with respect to substituent effects. In the case of electronic structure,  $BO$  and  $CN$  substitution showed a large stabilization for the HOMO/LUMO and electron detachment energies as a result of large  $-M$  effect while  $OH$  and  $NH_2$  substitution resulted in the opposite due to  $+M$  effect on the boron cage. For halogen substitution, the inductive effects of the substituents became more dominant than their mesomeric effect and electronic stabilization was provided by  $-I$  effect on the boron cage. For all cases, substitution effects on the electronic structure of boron clusters showed a striking resemblance to the  $\pm M$  and  $\pm I$  effects observed for the  $\pi$ -conjugated systems.

In addition to the effects on electronic structure, we have examined the substituent effect on the formation enthalpies for larger boron clusters with the addition of  $BX$  groups to  $[B_{12}X_{12}]^{2-}$ . For halogen and  $CN$  substitutions, the icosahedral barrier showed an increase compared to  $X=H$  case whereas functionalization with substituents with  $+M$  effect such as  $OH$  and  $NH_2$  showed a considerable reduction the icosahedral barrier. Similar results were also found for selective carborane clusters. In general, our results showed that the icosahedral barrier can be reduced through substitution by destabilizing the  $[B_{12}X_{12}]^{2-}$  cluster with symmetry-reducing ligands or ligands with  $+M$  effects rather than stabilizing the larger clusters. To the best of our knowledge, benchmarking the functionalized closo-borane dianions through their electronic structures and stability relations on the basis of formation reactions have not been discussed previously. In that

regard, we hope that this study can be a useful guide for future experimental and theoretical investigations for such systems.



# Chapter 4

## Fluorescence Quenching in Carborane-Fluorophore Systems

### 4.1 Introduction

Fluorescent  $\pi$ -conjugated molecules have attracted tremendous interest in the last few decades as functional materials for both fundamental photophysical studies and in new-generation light-emitting and sensing applications ranging from life sciences to optoelectronics.[234–238] Especially, the ability to engineer fluorescent  $\pi$ -frameworks by electron-accepting and -donating substituents or (hetero)aromatic building blocks has enabled unprecedented diversity and fine-tuning ability in chemical structures and optoelectronic/sensing characteristics.[239–241] To this end, one of the unconventional approaches include carboranes, which are non-classically bonded clusters of boron, carbon, and hydrogen atoms. Among carboranes, icosahedral closo-carborane ( $C_2B_{10}H_{12}$ ) stands out as a highly stable neutral framework as described by Wade-Mingos rules.[42,44,242] In icosahedral closo-carboranes, three isomeric forms showing different polarities[82] and electronic acceptor capabilities (para < meta << ortho)[83,84] are plausible (1,2- $C_2B_{10}H_{12}$  (*o*-carborane), 1,7- $C_2B_{10}H_{12}$  (*m*-carborane), and 1,12- $C_2B_{10}H_{12}$  (*p*-carborane)). Among them, *o*-carborane containing two adjacent carbon atoms is the most studied cluster based on its facile reaction with varied  $\pi$ -systems to yield chemically and thermally stable molecules with potential applications in catalysis, electronics, energy storage, and medicine.[48,88–95]

More recently, *o*-carborane has drawn attention as a building block to modify the chemical structures and to tune the fluorescence properties of  $\pi$ -conjugated fluorophores.[93,129,131–143,243–245] *o*-carborane shows distinct electron

delocalization via three-center two-electron bonds, which, along with the presence of boron atoms, gives strong electron-withdrawing ability to this cluster framework.[131] Therefore, when *o*-carborane is tethered to a relatively  $\pi$ -electron rich fluorophore at one of its carbon positions via a C-C single bond, donor-acceptor type electronic structures with tunable intramolecular charge transfer (ICT) characteristics could be realized.[143,246] While the *o*-carborane-fluorophore adducts typically exhibit low photoluminescence quantum yields in varied solutions, a unique enhanced emission behavior can be observed in the solid-state (i.e., aggregation-induced emission (AIE)).[136,141,247–249] This has been discussed in the previous literature that restricting the undesired vibrations of *o*-carborane's "C-C" bond in the aggregate state leads to enhanced photoluminescence quantum yields. In addition, it has been shown that the enhancement in emission could also be achieved in solution phase via structural modifications on the *o*-carborane to limit *o*-carborane's "C-C" bond elongation that play a critical role in emission quenching mechanisms.[141,148,248] It is also noteworthy that the dihedral angle between the *o*-carborane's "C-C" bond and the fluorophore is another key parameter affecting the emission properties and tuning dual emission characteristics.[247,250–254]

Among *o*-carborane-fluorophore adducts studied to date, *o*-carborane-anthracene (*o*-CB-*Ant*) molecule and its derivatives have attracted significant attention both for theoretical and synthetic studies since the seminal works by Chujō and co-workers.[243,244] In solution, *o*-CB-*Ant* shows dual emissions with low quantum yields, where the high-energy  $S_1 \rightarrow S_0$  transition has a local excited state (LE) character on anthracene whereas the low-energy transition shows twisted intramolecular charge transfer (TICT). The TICT state mainly arises from the strong interaction between the *o*-carborane's "C-C" bond and the anthracene's  $\pi$ -conjugated system, along with the perpendicular rearrangement of C-C bond with respect to the plane of anthracene.[149] This TICT emission can be maintained even in aggregated or crystal states due to the presence of sufficient space for rotations as a result of *o*-CB's compact spherical structure.[149,243,247] On the other hand, the photophysical properties of *o*-CB-*Ant* system can be manipulated via functionalization or substitution of the adjacent C atoms on the *o*-carborane. For example, while only high energy TICT state with a low quantum yield is observed in solution with methyl or phenyl groups, a substitution with bulky groups (e.g., trimethylsilyl (TMS)) leads to a significant increase in the quantum yield.[94] More recently, Duan et al. have investigated the *o*-CB-*Ant* derivatives using



quantum mechanical and molecular dynamics simulations, based on which the elongation of C-C bond is suggested to lead to bathochromically shifted emissions with an increased CT character for the  $S_1 \rightarrow S_0$  transition.[149]

In light of these recent studies, it has been mostly suggested that the *o*-carborane's "C-C" bond elongation and the relative orientations of fluorophore *vs.* *o*-carborane moieties govern the electronic interaction and, hence, the photophysical properties of *o*-CB-*fluorophore* systems. However, a complete theoretical understanding is still lacking in the literature for the interplay of excited-state nature/energetics and potential energy surfaces (PESs) with regards to emissive transitions and quenching mechanisms. Thus, it is still of great importance to pursue theoretical investigations on novel *o*-CB-*fluorophore* systems with the motivations of revealing the key effects of structural modifications and providing a better understanding for the photophysical properties. To this end, we herein perform a detailed investigation for the PESs of the  $S_1$  state for *o*-CB-*Ant*. Furthermore, we investigate the role of different substituents (F, Cl, CN, OH) on the *o*-CB cluster along with a  $\pi$ -extended acene-based fluorophore, pentacene, (*o*-CB-*Pnt*) on the energetics and the nature of  $S_1 \rightarrow S_0$  transitions for different conformations. Our results indicate the presence of a non-emissive CT state for *o*-CB-*Ant* as a result of significant C-C bond elongation in *o*-CB, which is suggested to play an important role for emission quenching as this state also corresponds to the lowest-energy excited state on the  $S_1$  PES in our investigation. Our results also show that the relative energy of this non-emissive CT state and energy barriers on the  $S_1$  PES can be modulated with respect to substituents or fluorophore energy levels, which can guide future experimental work in terms of emission tuning and enhancement for *o*-CB-*fluorophore* systems.

## 4.2 Computational Details

All computations were performed using the Gaussian09[211] program package. The ground state geometries of the investigated *o*-CB-*Ant*, substituted *o*-CB-*Ant* and *o*-CB-*Pnt* systems were optimized at M06-2X/6-31G\* level of theory. No imaginary frequencies were found for the optimized molecules. An integral equation formalism variant of the polarizable continuum model (IEFPCM)[181–185] was employed using THF as the solvent for both ground state and excited state computations. The MO diagrams were visualized by using GaussView[212] and orbital contributions were

generated on GaussSum[255] packages. Excited states computations were performed using TDDFT formalism as implemented in Gaussian09. Multiwfn program[256] was employed to calculate the charge separation parameter ( $\Delta r$ ) for the excited states, degree of overlap ( $\Lambda$ ) indexes of hole and electron wave functions, and the heat maps of transition density matrices (TDMs). Energy barriers for the excited-state PESs were examined both by alteration of the dihedral angle ( $\varphi$ ) with fixed C-C bond length and by C-C bond elongation with fixed  $\varphi$ .

As shown in previous work,[243] there are two main degrees of freedom for the geometry of the *o*-CB-*Ant* system: the dihedral angle ( $\varphi$  for  $(C_1-C_2)-(C_3-C_4)$ ) between the carborane and anthracene moieties and the  $C_1-C_2$  bond length in the *o*-carborane cluster as shown with green and red arrows, respectively, along with numbering of C atoms in Figure 4.1. Two conformations of this system for the  $S_1$  state have been explored previously.[243] These two conformations are shown in Figure 4.4, and they correspond to the local excited (LE) and the hybridized local and charge-transfer (HLCT) excited states, respectively. We note that the second conformation has often been referred to as twisted-intramolecular charge transfer (TICT) state in earlier studies; however, our investigation reveals that this excited state shows a good mixture of both LE and CT characters and, thus, it is referred to as HLCT excited state in our work. In addition, in our analysis of the  $S_1$  state, a new conformation corresponding to a pure CT character (the rightmost conformation in Figure 4.4) is revealed (*vide infra*) for the first time in the literature, as a result of further elongation of the  $C_1-C_2$  bond.

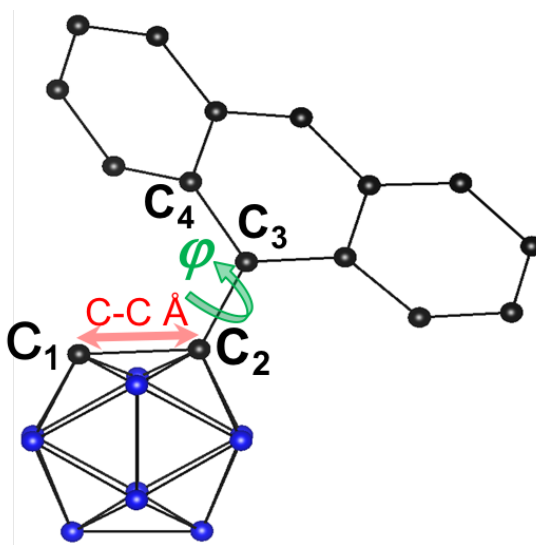


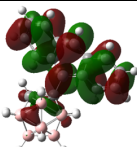
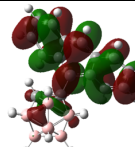
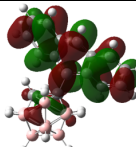
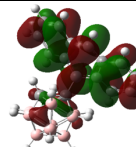
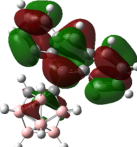
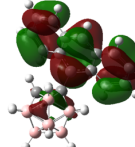
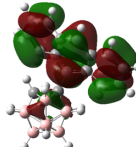
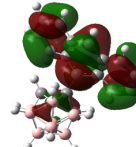
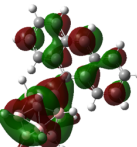
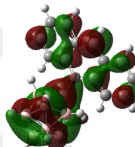
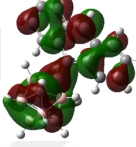
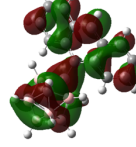
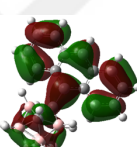
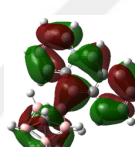
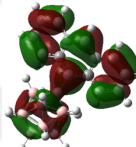
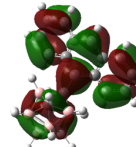
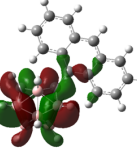
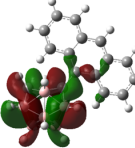
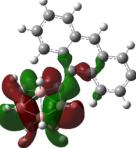
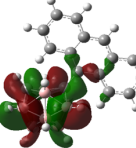
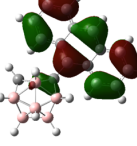
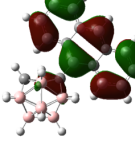
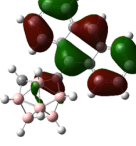
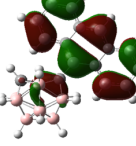
**Figure 4. 1** The illustration of important geometric parameters for excited-state geometries of *o*-CB-*Ant* along with numbering of C atoms used in the text.

Different functionals (BP86[215,216] (GGA), B3LYP[217] (hybrid), CAM-B3LYP[171] (range-separated), and M06-2X[172] (meta-hybrid)) were employed for the TDDFT optimization of three main excited-state conformations for benchmarking purposes. We note that B3LYP has been widely preferred for the excited-state investigation of *o*-CB-*Ant* as well as other carborane-fluorophore systems.[131–136,143,243,247,251,257–259] In general, this functional shows good agreement for the absorption and emission energies of these systems. However, one should also note that it can sometimes be problematic for pure CT states, as it is shown to underestimate the excited-state energies for such transitions.[174,260–263]

**Table 4. 1** Benchmark results for the emission and absorption energies in eV (emission wavelengths in parenthesis) for different XC-functionals from the three different conformers in comparison with the experimental results.

S <sub>1</sub> state	Emission Energies (eV)				
	Experiment[243]	BP86	B3LYP	CAM-B3LYP	M06-2X
LE	2.76 (450)	2.20 (564)	2.39 (519)	2.59 (479)	2.61 (476)
HLCT	2.07 (600)	1.74 (713)	1.94 (639)	2.18 (570)	2.25 (551)
CT	NA	0.33 (3781)	0.74 (1670)	1.40 (887)	1.31 (947)
S <sub>1</sub> state	Absorption Energies (eV)				
	Experiment[243]	BP86	B3LYP	CAM-B3LYP	M06-2X
LE	3.10 (400)	2.62 (474)	2.95 (420)	3.35 (370)	3.35 (370)

**Table 4. 2** Pictorial frontier orbitals of the three conformations for S<sub>1</sub> state along with the orbital contributions from *o*-CB and Ant moieties calculated with different XC functionals.

S <sub>1</sub> state	BP86	B3LYP	CAM-B3LYP	M06-2X
LUMO				
LE	CB: 8%, Ant: 92%	CB: 8%, Ant: 92%	CB: 7%, Ant: 93%	CB: 7%, Ant: 93%
HOMO				
	CB: 6%, Ant: 92%	CB: 6%, Ant: 94%	CB: 6%, Ant: 94%	CB: 6%, Ant: 94%
LUMO				
HLCT	CB: 62%, Ant: 38%	CB: 60%, Ant: 40%	CB: 48%, Ant: 52%	CB: 43%, Ant: 57%
HOMO				
	CB: 13%, Ant: 87%	CB: 14%, Ant: 86%	CB: 15%, Ant: 85%	CB: 13%, Ant: 87%
LUMO				
CT	CB: 96%, Ant: 4%	CB: 96%, Ant: 4%	CB: 96%, Ant: 4%	CB: 96%, Ant: 4%
HOMO				
	CB: 5%, Ant: 95%	CB: 5%, Ant: 95%	CB: 6%, Ant: 94%	CB: 7%, Ant: 93%

**Table 4. 3**  $\Delta r$  and  $\Lambda$  values for the excited states of *o*-CB-*Ant* system with different XC functionals.

	BP86		B3LYP		CAM-B3LYP		M06-2X	
	$\Delta r$ (Å)	$\Lambda$	$\Delta r$ (Å)	$\Lambda$	$\Delta r$ (Å)	$\Lambda$	$\Delta r$ (Å)	$\Lambda$
LE	0.28	0.83	0.23	0.84	0.21	0.84	0.20	0.84
HLCT	1.78	0.65	1.68	0.67	1.06	0.71	0.92	0.73
CT	4.18	0.22	4.14	0.22	3.89	0.24	3.85	0.25

In Table 4.1, 4.2, 4.3 and Figure 4.2, we compare the results of our benchmark calculations. As shown in the table, BP86 significantly underestimates the experimental results as expected. In comparison, B3LYP shows some improvements towards experimental values as the predicted energies of the vertical  $S_0 \rightarrow S_1$  and  $S_1 \rightarrow S_0$  transitions of LE and HLCT states are 0.19-0.33 eV higher than those with BP86. Overall, the performances of M06-2X and CAM-B3LYP functionals are better when compared with B3LYP functional, especially for the  $S_1 \rightarrow S_0$  transitions of the LE state. However, the largest deviation ( $\sim 0.6$  eV) between B3LYP and M06-2X/CAM-B3LYP is seen for the  $S_1 \rightarrow S_0$  transition energy of the CT state as expected. BP86 and B3LYP functionals are also found to overestimate the degree of charge transfer, particularly for HLCT and CT states (Figure 4.2). Therefore, we concluded that both BP86 and B3LYP functionals are not suitable for the investigation of the excited-state PES, due to the involvement of pure CT character for certain geometry conformations. Meanwhile, the difference between the predicted transition energies via M06-2X and CAM-B3LYP are within 0.1 eV for all states. There is also a good agreement for the predicted  $\Delta r$  and  $\Lambda$  parameters for these functionals. We note that M06-2X functional has been shown to perform better for cluster systems compared to other functionals in terms of bonding and structure predictions.[264,265] In addition, this functional generally showed more stable excited-state geometry optimizations when constraints were involved in our test calculations as compared to CAM-B3LYP. Therefore, we used M06-2X/6-31G\* level of theory for the rest of our investigation.

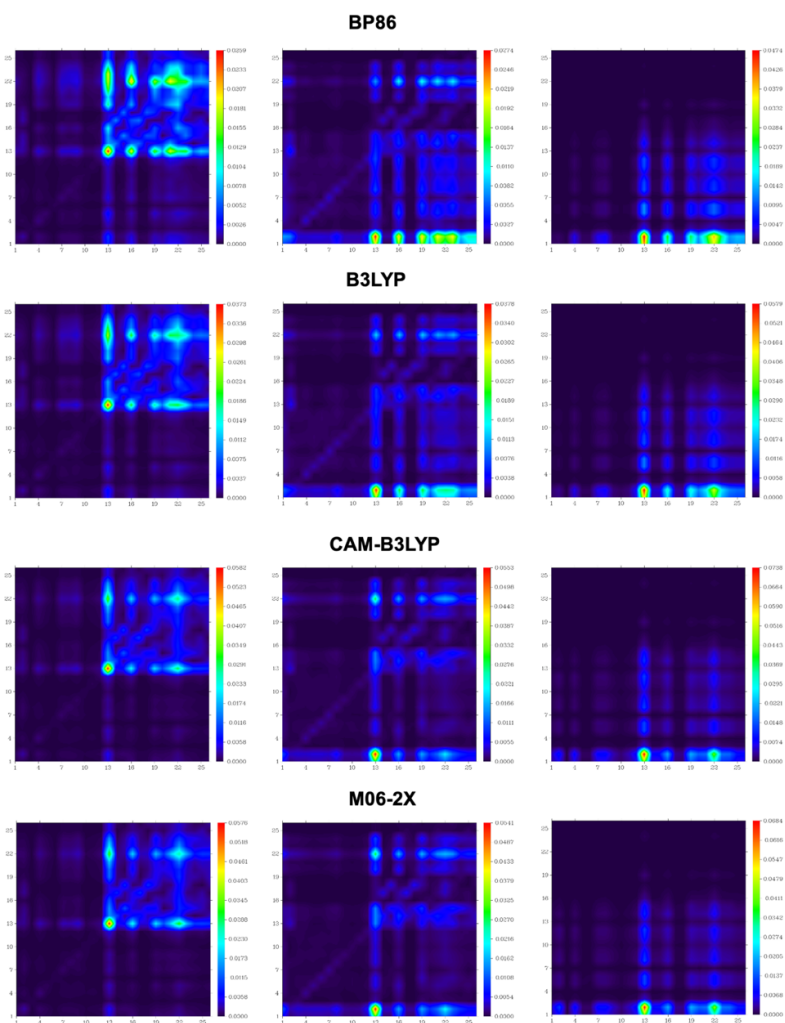


**Figure 4. 2** Heat maps of transition density matrix (TDM) graphs for  $S_1$  states of a) LE b) HLCT and c) CT states calculated with different XC functionals.

## 4.3 Results and Discussion

### 4.3.1 *o*-CB-*Ant* System

In Figure 4.4, we summarize the energetics, excited-state geometries, along with the excited-state characteristics for the vertical  $S_0 \rightarrow S_1$  transition (absorption), and the possible  $S_1 \rightarrow S_0$  pathways (emission) for *o*-CB-*Ant* system. In the case of vertical  $S_0 \rightarrow S_1$  transition and the  $S_1 \rightarrow S_0$  transition in the LE conformation, the excited states mainly originate from the  $\pi$ - $\pi^*$  transition localized on the anthracene  $\pi$ -system, and the calculated oscillator strengths are similar ( $f = 0.22$  vs.  $0.25$ ). The transition energies for vertical  $S_0 \rightarrow S_1$  ( $E_{0 \rightarrow 1}$ ) and  $S_1 \rightarrow S_0$  ( $E_{1 \rightarrow 0}$ ) in the LE state are calculated to be 3.32 eV and 2.61 eV, respectively. On the other hand, as a result of the  $C_1$ - $C_2$  bond elongation ( $1.66 \text{ \AA} \rightarrow 2.25$

Å) and the alteration of the dihedral angle ( $-13.0^\circ \rightarrow -86.5^\circ$ ) as shown in Figure 4.4, another possible  $S_1 \rightarrow S_0$  pathway is predicted with an HLCT character, a reduced transition energy ( $E_{1 \rightarrow 0} = 2.25$  eV), and an increased oscillator strength ( $f = 0.49$ ). At this point, two important parameters play major roles for the electronic structures and the resulting excited-state energetics/characteristics. Firstly, the energy of the LUMO level for *o*-carborane moiety can be altered significantly with the  $C_1$ - $C_2$  bond length as this level shows a large antibonding character between  $C_1$  and  $C_2$ . The comparison of the frontier orbital energy levels for varying  $C_1$ - $C_2$  bond lengths is shown in Figure 4.3. Secondly, the degree of orbital mixing between anthracene and *o*-carborane LUMO levels can be altered with  $\varphi$ , where, unlike traditional push-pull systems;  $\varphi = -90^\circ$  corresponds to a maximum coupling between these orbitals while  $\varphi = 0^\circ$  corresponds to a minimum coupling. As a result, elongated  $C_1$ - $C_2$  bond length (2.25 Å) and the large  $\varphi$  ( $-87^\circ$ ) induces a strong orbital mixing between *o*-carborane and anthracene originated levels for the electron wavefunction of the HLCT state as shown in Figure 4.4. It should be noted that our findings are in good agreement with the previous findings by Chujo and coworkers[243] as the emission ( $S_1 \rightarrow S_0$ ) is experimentally shown to be possible from both LE and HLCT states.

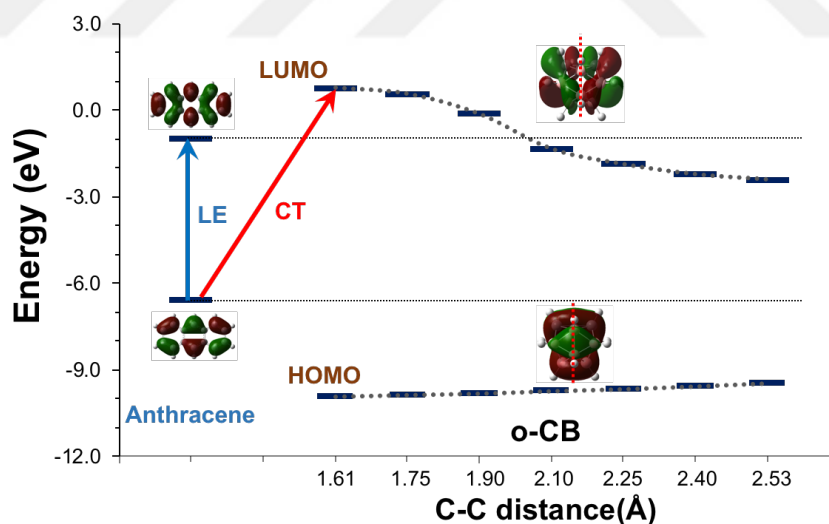


**Figure 4. 3** Relative energies of the frontier levels for *o*-CB and Ant moieties with respect to  $C_1$ - $C_2$  distance on *o*-CB.

As shown in Figure 4.3, it is possible for the *o*-carborane LUMO level to be considerably lower in energy than that of anthracene with elongation of the  $C_1$ - $C_2$  bond. This is indeed the case for the formation of pure CT state of *o*-CB-*Ant* where  $C_1$ - $C_2$  bond length increases to 2.53 Å. In addition, since  $\varphi$  becomes  $0^\circ$ , the orbital mixing between

*o*-carborane- and anthracene-based levels is restricted by symmetry. As a result, the corresponding  $S_1 \rightarrow S_0$  transition in this conformation is of strong CT character with a vanishing oscillator strength, where hole and electron are spatially separated and localized on the anthracene and the *o*-carborane moieties, respectively. The energy of the  $S_0$  state for the CT state geometry is calculated to be much higher ( $\Delta E_0 = 1.48$  eV) than that of the ground-state geometry. In comparison, the same energy differences for HLCT and LE states are 0.71 and 0.36 eV, respectively. Despite this large deviation from the minimum  $S_0$ , the adiabatic energy of the excited state ( $E_{S_1}$ ) for the CT state is 2.79 eV, which is not only lower than both LE and HLCT states but also the predicted minimum energy on the  $S_1$  PES in our investigation. This is, of course, related to the fact that  $E_{1 \rightarrow 0}$  becomes significantly smaller (1.31 eV), indicating an energetically close point between  $S_1$  and  $S_0$  surfaces.

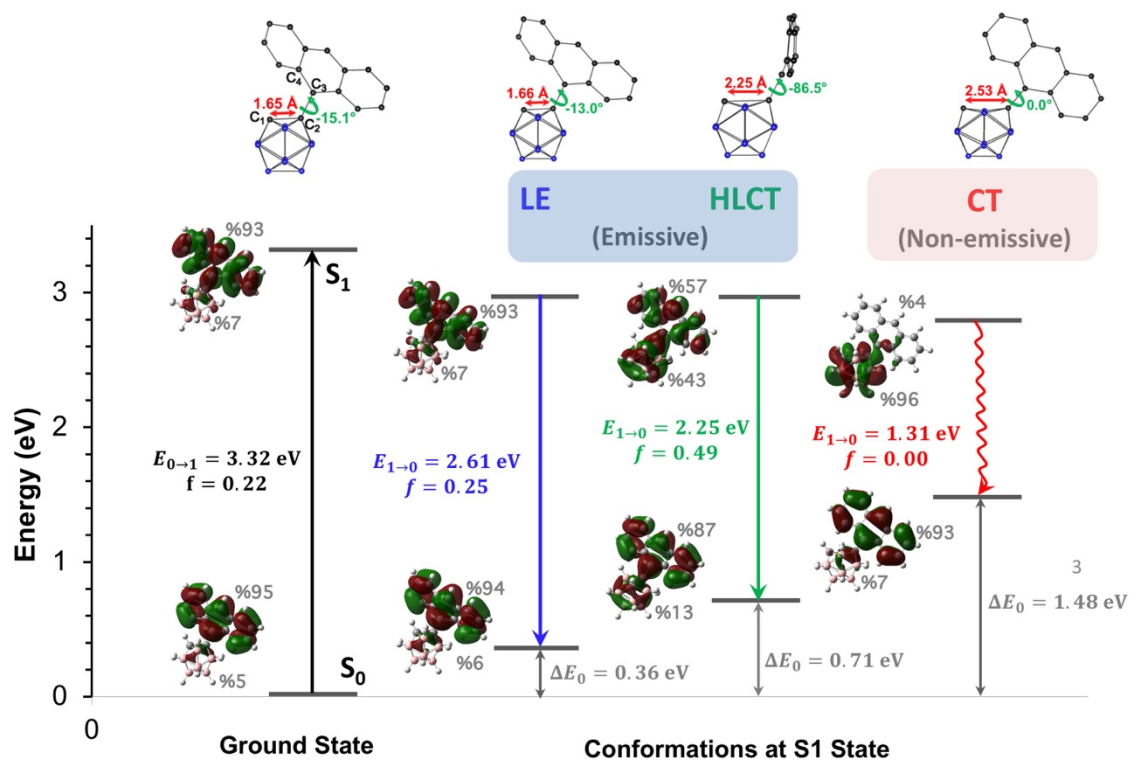


**Figure 4. 4** Illustration of the absorption and potential emission paths along with the corresponding geometries of the *o*-CB-*Ant* system. Transition energies ( $E_{0 \rightarrow 1}/E_{1 \rightarrow 0}$ ) and the oscillator strengths ( $f$ ) are shown for each process. Adiabatic  $S_1$  state energies ( $E_{S_1}$ ) were calculated by the addition of  $E_{0 \rightarrow 1}/E_{1 \rightarrow 0}$  for the absorption and emissive/non-emissive processes to the ground state energies ( $\Delta E_0$ ) at corresponding geometric conformations. These three conformations correspond to the minimum energy points on the excited state ( $S_1$ ) potential energy surface. % contribution of anthracene and *o*-CB based orbitals to HOMO and LUMO for each transition are shown on the orbital pictures.



The excited-state optimization of *o*-CB-*Ant* reveals three critical C<sub>1</sub>-C<sub>2</sub> bond lengths. While the CT state exhibits the minimum energy for S<sub>1</sub>, it is also important to understand the energy barriers on PESs and the excited-state characteristics of S<sub>1</sub> state for different conformations. In Figure 4.5, we show the PESs for the S<sub>1</sub> state with respect to  $\varphi$  for fixed C<sub>1</sub>-C<sub>2</sub> bond lengths (Figure 4.5a-c), calculated TDMs for selective S<sub>1</sub> states on this surface (Figure 4.5d-f), and oscillator strengths for the corresponding S<sub>1</sub> → S<sub>0</sub> transitions (Figure 4.5g-i). When C<sub>1</sub>-C<sub>2</sub> bond length is 1.66 Å, the energy of S<sub>1</sub> is minimum for  $\varphi = -13^\circ$  (LE state), while there is a local minimum at  $-90^\circ$  with a very similar energy. It is seen that there is a rotational barrier ( $\sim 0.3$  eV) with changing  $\varphi$  where the maximum energy is calculated for the conformation where  $\varphi = -45^\circ$ . For this surface, S<sub>1</sub> → S<sub>0</sub> transitions mainly originate from the  $\pi$ - $\pi^*$  transitions of anthracene for all conformations, regardless of  $\varphi$ . As a result, the calculated oscillator strengths along with  $\Lambda$  and  $\Delta r$  parameters (Table 4.4) are quite similar and show strong LE characteristics for all  $\varphi$  values.

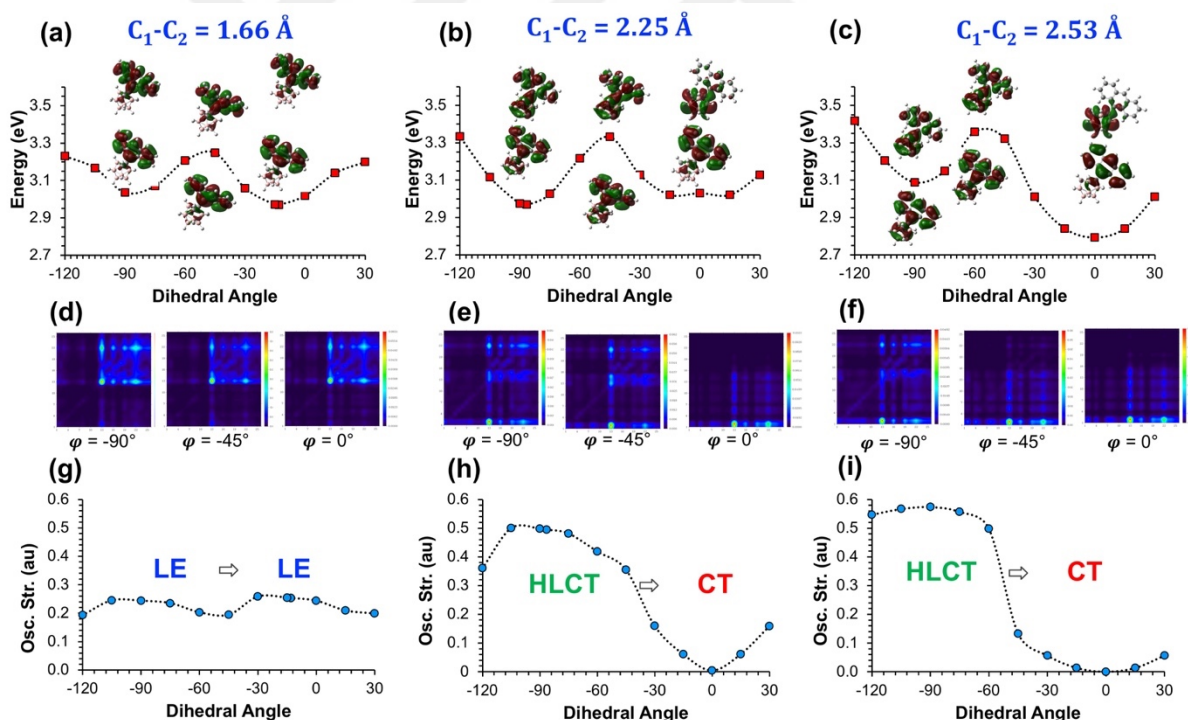


**Figure 4. 5** (a-c) Potential energy surfaces (PESs) for the adiabatic excited-state energies ( $E_{S_1}$ ) with respect to  $\varphi$  at fixed C<sub>1</sub>-C<sub>2</sub> bond lengths, (d-f) heat maps of transition density matrix (TDM) graphs for selective S<sub>1</sub> states calculated with M06-2X/6-31G\* ( $\Delta r$  and  $\Lambda$  indexes are given in Table 4.4), and (g-i) calculated oscillator strengths for the corresponding S<sub>1</sub> → S<sub>0</sub> transitions. Frontier orbital pictures are also given for some specific conformations on PES diagrams to show the excited state character change. Atom numbering for the TDM plots is given in Figure 4.6.

**Table 4. 4**  $\Delta r$  and  $\Lambda$  values for the TDMs given in Figure 4.5 for selective  $S_1 \rightarrow S_0$  transitions on the PESs with respect to  $\varphi$  at fixed  $C_1-C_2$  bond lengths.

	$C_1-C_2 = 1.60 \text{ \AA}$		$C_1-C_2 = 2.25 \text{ \AA}$		$C_1-C_2 = 2.53 \text{ \AA}$	
	$\Delta r (\text{ \AA})$	$\Lambda$	$\Delta r (\text{ \AA})$	$\Lambda$	$\Delta r (\text{ \AA})$	$\Lambda$
$\varphi = 0^\circ$	0.2	0.83	3.7	0.28	3.9	0.25
$\varphi = -45^\circ$	0.2	0.82	0.8	0.75	3.1	0.47
$\varphi = -90^\circ$	0.2	0.83	0.9	0.73	1.4	0.69

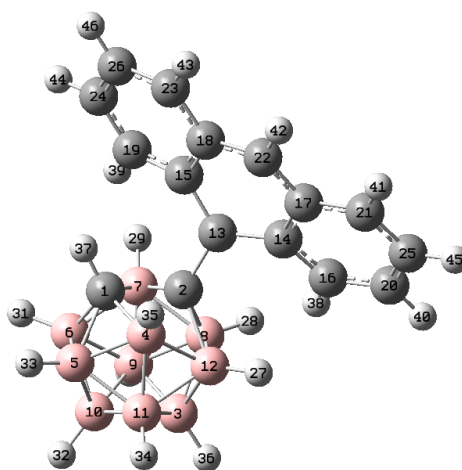


**Figure 4. 6** Atomic labels for the heat maps of TDM (H atoms are not given in the heat maps). *o*-CB atoms are numbered as 1-12 (left and down in TDM plots) whereas *Ant* atoms are numbered as 13-26. (right and up in TDM plots)

When the  $C_1-C_2$  bond partially stretches to  $2.25 \text{ \AA}$ , the minimum  $E_{S_1}$  ( $2.97 \text{ eV}$ ) corresponds to the twisted conformation with  $\varphi = -87^\circ$ . Similar to the case where the  $C_1-C_2$  bond length is  $1.66 \text{ \AA}$ , there is a rotational barrier with a slightly increased energy of  $\sim 0.4 \text{ eV}$  and the conformation with  $\varphi = -45^\circ$  corresponds to the local maximum (energy =  $3.33 \text{ eV}$ ). In this case, however, the nature of the  $S_1 \rightarrow S_0$  transitions show a significant alteration with  $\varphi$ , as indicated in the oscillator strengths trend (Figure 4.7h), along with calculated TDMs (Figure 4.7e), and  $\Lambda$  or  $\Delta r$  parameters (Table 4.4). When  $\varphi$  is close to  $-90^\circ$ , the  $S_1 \rightarrow S_0$  transition exhibits HLCT character where hole wave function is mainly localized on anthracene while electron wave function extends to both *o*-carborane and anthracene moieties. As a result,  $\Delta r$  index shows a significant increase for this transition

compared to the LE case, while  $\Lambda$  shows a slight decrease. In addition, CT character becomes more dominant as  $\varphi$  changes from  $-90^\circ$  to  $0^\circ$ . At  $\varphi = 0^\circ$ , the total energy of  $S_1$  (3.02 eV) is comparable to that with the  $\varphi = -87^\circ$ ; however, the calculated oscillator strength for the  $S_1 \rightarrow S_0$  transition vanishes as a result of the strong CT character at this point. For this case, TDM and MO analysis reveal that the electron wave function is localized on the *o*-carborane cluster while the hole wave function is localized on the anthracene moiety.

For conformations where the  $C_1$ - $C_2$  bond is fully elongated to 2.53 Å, the origin of the  $S_1 \rightarrow S_0$  transition with respect to  $\varphi$  shows a similar trend to the case where the  $C_1$ - $C_2$  bond is 2.25 Å as illustrated by calculated oscillator strengths and TDMs in Figure 4.5. As to the other PESs, there is a rotational barrier with a local maximum located at between  $-45^\circ$  and  $-60^\circ$ . In general, the CT character for the  $S_1 \rightarrow S_0$  transitions on this surface is more pronounced compared to the other cases due to increasing contribution from the *o*-carborane-based orbitals to the electron wave function. Another important point is that the minimum point (2.79 eV) occurs at  $\varphi = 0^\circ$  (CT state), with a significantly lower energy than the local minima at  $\varphi = -90^\circ$  (3.09 eV) and the other minima (LE and HLCT states) in previous PESs (2.97 eV). As mentioned earlier, this conformation corresponds to the global minimum for the calculated  $E_{S_1}$  in our investigation.

Similar to our analysis with  $\varphi$ , Figure 4.7a-c shows the calculated PESs of  $S_1$  state for  $C_1$ - $C_2$  bond elongation for fixed  $\varphi$  values at  $-13^\circ$ ,  $-87^\circ$  and  $0^\circ$ , respectively. In addition, the TDMs for selected points (Figure 4.7d-f) and the calculated oscillator strengths (Figure 4.7g-i) are given to investigate the origin of the corresponding  $S_1 \rightarrow S_0$  transitions along these surfaces. It should be noted that the PESs and the oscillator strengths at  $\varphi = -13^\circ$  and  $\varphi = 0^\circ$  show a similar trend, which originates from the fact that orbital mixing between *o*-carborane and anthracene-based levels is similarly restricted for such small  $\varphi$  values. In both cases, the PESs show an energy barrier of  $\sim 0.3$  eV with bond elongations at a maximum point of  $\sim 2.0$  Å. Interestingly, this bond length also corresponds to the crossover point for  $S_1 \rightarrow S_0$  transitions from LE to CT character as indicated from the calculated oscillator strengths. This is, of course, related to the relative energies of the *o*-carborane-based and anthracene-based frontier orbitals for the unoccupied levels (Figure 4.3) in the electronic structure. When  $\varphi$  is  $-87^\circ$ , however, the calculated PES becomes quite flat indicating that  $C_1$ - $C_2$  bond elongation can occur on this surface without an energy penalty. Another important point is that  $S_1 \rightarrow S_0$  transition

becomes increasingly HLCT character with C<sub>1</sub>-C<sub>2</sub> elongation as shown by the increase of the corresponding oscillator strengths (Figure 4.7h) and TDMs (Figure 4.7e).

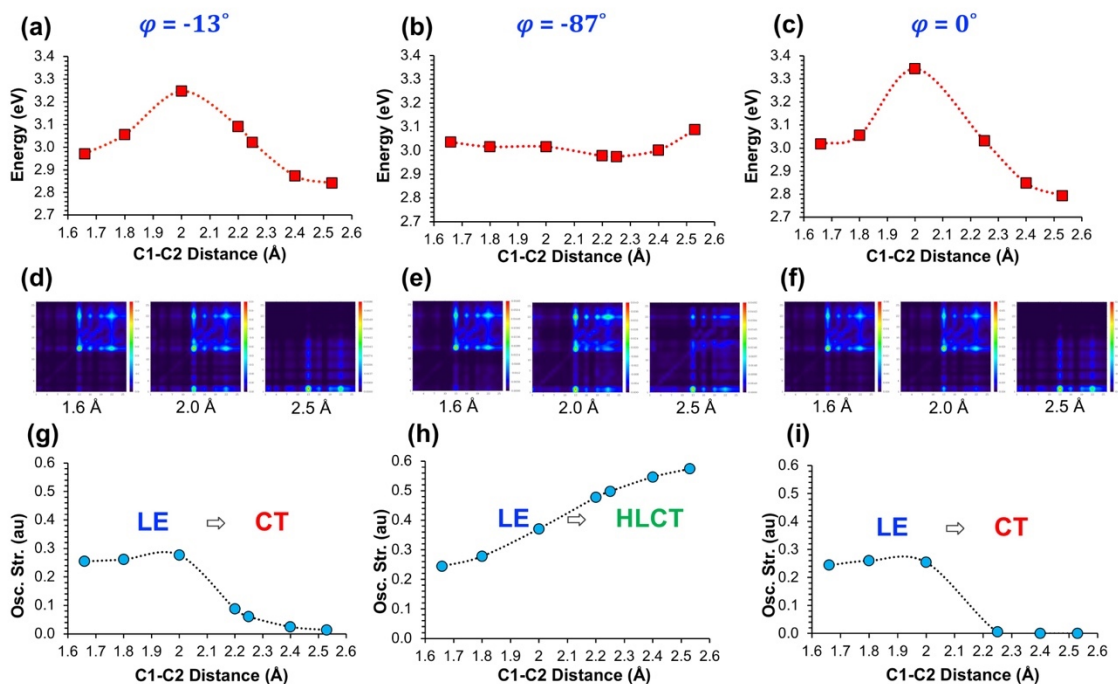


**Figure 4. 7** (a-c) Potential energy surfaces (PESs) for the adiabatic excited-state energies ( $E_{S_1}$ ) with respect to C<sub>1</sub>-C<sub>2</sub> bond lengths at fixed  $\varphi$ , (d-f) TDMs for selective S<sub>1</sub> states ( $\Delta r$  and  $\Lambda$  indexes are given in Table 4.5), and (g-i) calculated oscillator strengths for the corresponding S<sub>1</sub>  $\rightarrow$  S<sub>0</sub> transitions. Atom numbering for the TDM plots are given in Figure 4.6.

**Table 4. 5**  $\Delta r$  and  $\Lambda$  values for the TDMs given in Figure 4.7 for selective S<sub>1</sub>  $\rightarrow$  S<sub>0</sub> transitions on the PESs with respect to C<sub>1</sub>-C<sub>2</sub> bond lengths at fixed  $\varphi$ .

	$\varphi = -13^\circ$		$\varphi = -87^\circ$		$\varphi = 0^\circ$	
	$\Delta r$ (Å)	$\Lambda$	$\Delta r$ (Å)	$\Lambda$	$\Delta r$ (Å)	$\Lambda$
C <sub>1</sub> -C <sub>2</sub> = 1.60Å	0.2	0.84	0.2	0.83	0.2	0.83
C <sub>1</sub> -C <sub>2</sub> = 2.00Å	0.4	0.81	0.4	0.80	0.3	0.82
C <sub>1</sub> -C <sub>2</sub> = 2.50Å	3.8	0.31	1.4	0.69	3.9	0.25

Previous experimental and theoretical work on *o*-CB-*Ant* and its derivatives have shown that these systems can facilitate dual emission in solution and solid state through LE and HLCT (or TICT) states as a result of intramolecular rotation upon photoexcitation. In addition, these systems generally exhibit low quantum yields in solution, which is often associated with the vibrational motion of the C<sub>1</sub>-C<sub>2</sub> bond. More recently, Ochi et

al.[147,148] have demonstrated that for carbon–boron fused carboranes, C<sub>1</sub>-C<sub>2</sub> bond elongation can cause emission quenching without an intramolecular rotation. In our investigation for the S<sub>1</sub> state of *o*-CB-*Ant*, it is revealed that C<sub>1</sub>-C<sub>2</sub> bond elongation to 2.53 Å leads to a non-emissive S<sub>1</sub> → S<sub>0</sub> transition with a strong CT character and a vanishing oscillator strength, which also corresponds to the lowest-energy point on the S<sub>1</sub> PES. While this conformation exhibits a highly-energetic S<sub>0</sub> point (1.48 eV as shown in Figure 4.4), the calculated energy barriers on the S<sub>1</sub> surfaces are quite reasonable (0.3-0.4 eV) suggesting that the molecule can reach to this geometry via electronic-vibronic couplings upon photoexcitation. We also note that the energy gap between the S<sub>0</sub> and the S<sub>1</sub> surfaces becomes quite small around this point, which can further increase the nonradiative decay rate according to the energy gap law. These findings along with previous experimental evidence suggest that the CT state resulting from fully elongated C<sub>1</sub>-C<sub>2</sub> bond could be an important pathway on the fluorescence quenching of *o*-CB-*Ant* and its derivatives.

### 4.3.2 Substitution Effect

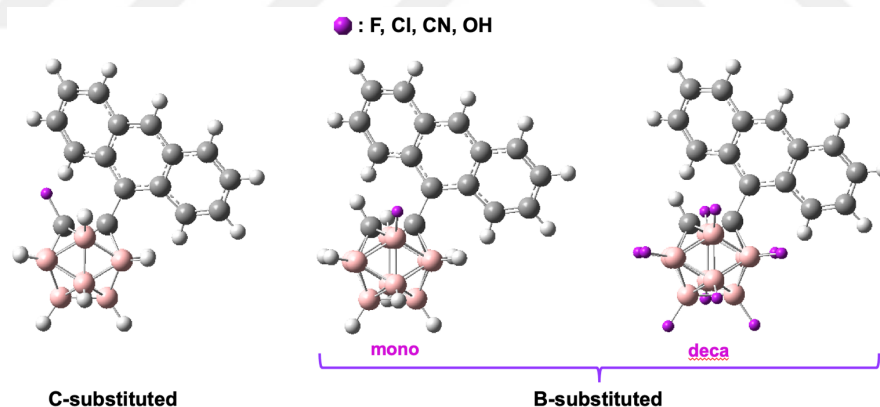


**Figure 4. 8** Positions of substituents for *o*-CB-*Ant* derivatives (X: F, Cl, CN and OH).

On the basis of our findings, the LUMO energy level of *o*-CB and its response to structural changes in excited state (e.g., C<sub>1</sub>-C<sub>2</sub> bond elongation or intramolecular twist) plays a key role in determining the nature and energetics of S<sub>1</sub> → S<sub>0</sub> transitions, and, in principle, it could be tuned by substituting different elements or groups on the carbon or boron atoms. Thus, we envisioned to investigate varied substituents (-F, -Cl, -CN, and -OH) in the current *o*-CB-*Ant* system. It has been previously shown that different

substituents on (car)borane clusters can induce strong mesomeric ( $\pm M$ ) and inductive ( $\pm I$ ) effects on the frontier energy levels of these clusters.[266] In this regard, we investigated how substitution may affect the photophysical properties of *o*-CB-*Ant* by altering the LUMO energy level of the *o*-carborane cluster. In Table 4.6, the effects on the excited-state geometries and the transition energies are given for *o*-CB-*Ant* derivatives with different substitutions on one of the carbon atoms (see Figure 4.8 for the geometries of substituted derivatives).

**Table 4. 6** Transition energies ( $E_{0\rightarrow 1}$  or  $E_{1\rightarrow 0}$ ), oscillator strengths ( $f$ ), adiabatic  $S_1$  state energies ( $E_{S1}$ ),  $C_1$ - $C_2$  lengths and dihedral angles ( $\varphi$ ) for ground state and three main  $S_1$  state conformations of *o*-CB-*Ant*. (Energies are given in eV.)

Substitution	$S_{0,min}$					LE State				
	$E_{0\rightarrow 1}$	$f$	$E_{S1}$	$C_1$ - $C_2$	$\varphi$	$E_{1\rightarrow 0}$	$f$	$E_{S1}$	$C_1$ - $C_2$	$\varphi$
H	3.37	0.22	3.37	1.65	-15	2.61	0.25	2.97	1.66	-13
F	3.31	0.23	3.31	1.69	-21	2.51	0.25	2.90	1.69	-19
Cl	3.23	0.22	3.23	1.73	-27	2.24 <sup>(a)</sup>	0.21	2.77	1.73	-25
CN	3.23	0.22	3.23	1.70	-23	2.26 <sup>(a)</sup>	0.21	2.78	1.70	-26
OH	3.30	0.22	3.30	1.76	-22	2.50	0.25	2.89	1.75	-21
	HLCT State					CT State				
	$E_{1\rightarrow 0}$	$f$	$E_{S1}$	$C_1$ - $C_2$	$\varphi$	$E_{1\rightarrow 0}$	$f$	$E_{S1}$	$C_1$ - $C_2$	$\varphi$
H	2.25	0.49	2.97	2.25	-86	1.31	0.00	2.79	2.53	0
F	2.24	0.50	2.61	2.25	-87	1.21	0.00	2.36	2.51	0
Cl	2.17	0.49	2.18	2.27	-87	1.04	0.00	2.00	2.56	0
CN	2.02	0.50	2.08	2.32	-87	0.90	0.00	1.81	2.54	0
OH	2.37	0.40	2.57	2.13	-86	1.18	0.00	2.49	2.55	0

<sup>(a)</sup> LE geometry calculations for Cl and CN substituted molecules were performed with fixed  $C_1$ - $C_2$  bond since they tend towards to the formation of HLCT state for these derivatives

For the vertical  $S_0 \rightarrow S_1$  transitions (i.e., optical absorption), it is seen that substitution causes only a slight energetic red-shift for all systems as compared to that with -H substituents. The reason is that these transitions mainly maintain the  $\pi \rightarrow \pi^*$  character localized on the anthracene unit. The red-shift is 0.06-0.07 eV for -F and -OH substitutions, while the same red-shift with -Cl and -CN substitutions are slightly more pronounced (0.14 eV). Similarly, the  $S_1 \rightarrow S_0$  transition (i.e., optical emission) shows a local  $\pi \rightarrow \pi^*$  character for all substitutions in the case of LE state as well. However, in this case the red-shifts with respect to that with -H substituents are significantly higher

with -Cl and -CN substitutions ( $\sim 0.35$  eV). A similar shift is also calculated for the adiabatic excited-state energies ( $E_{S1}$ ) as well. In comparison, for the twisted conformation where  $\varphi = -86^\circ$  or  $-87^\circ$ , the substitution shows a more pronounced stabilization effect on the calculated  $E_{S1}$ . In the case of unsubstituted *o*-CB-*Ant*, there is no energy difference for  $E_{S1}$  values between HLCT and the LE states. On the other hand, HLCT state becomes significantly more stable upon substitution. This stabilization mainly originates from the fact that the energy difference between the minimum  $S_0$  geometry and the twisted-conformation  $S_0$  geometry ( $\Delta E_0$ ) becomes much smaller upon substitution. The stabilization of HLCT state when compared to the LE state is more pronounced with substitutions showing strong -M effect (0.70 eV for -CN), while -OH and -F substitutions show  $\sim 0.3$  eV decreases for the  $E_{S1}$  of the twisted conformation compared to the LE conformations. We note that the CT state remains the global minimum with all substituents. For the unsubstituted system, the energy difference between CT and HLCT states is calculated to be 0.18 eV. With substitution, this energy difference becomes largest for the case of -CN (0.27 eV), while it decreases by 0.08 eV for -OH substitution.

In addition to the geometric parameters of fully optimized excited-state geometries, we have also scanned the PESs of the  $S_1$  state with respect to  $\varphi$  for fixed  $C_1$ - $C_2$  bond lengths for each substituted-*o*-CB-*Ant*. The comparison of  $E_{S1}$ 's is given in Figure 4.9a and 4.9b for fixed  $C_1$ - $C_2$  bond length of partially ( $C_1$ - $C_2 = 2.32$ - $2.13$  Å) and fully-stretched ( $C_1$ - $C_2 = 2.51$ - $2.56$  Å) conformations of each system, respectively. Figure 4.9c and 4.9d show the corresponding oscillator strengths for these  $S_1 \rightarrow S_0$  transitions. When the  $C_1$ - $C_2$  bond lengths are partially stretched (those corresponding to the twisted conformations for each system), the calculated PESs (Figure 4.9a) with -Cl and -F substitutions show a similar trend to the unsubstituted case. With the -CN substitution, however, HLCT state ( $\varphi = -87^\circ$ ) does not correspond to the minimum point for this PES anymore, as the CT state ( $\varphi = 0^\circ$ ) is predicted to be 0.16 eV more stable compared to the HLCT state. This stabilization results from the strong -M effect and longer  $C_1$ - $C_2$  bond length induced by the -CN substituents, which strongly stabilizes the *o*-carborane-based orbital energy levels. In the case of -OH substitution, the HLCT state is predicted to be more stable, while the CT state is predicted to be strongly destabilized as shown in Figure 4.9a. For fully stretched conformations ( $C_1$ - $C_2 = 2.51$ - $2.56$  Å, Figure 4.9b), all substituents show a similar PES and oscillator strength trends compared to the unsubstituted *o*-CB-*Ant*. In all cases, CT state with  $\varphi = 0^\circ$  is predicted to be the minimum, while there is another local



minimum having HLCT character predicted for  $\varphi = \sim 90^\circ$ . The energy difference between the CT and HLCT states on this PES is calculated to be the largest with -CN substitution (0.37 eV) and smallest with -OH substitution (0.28 eV).

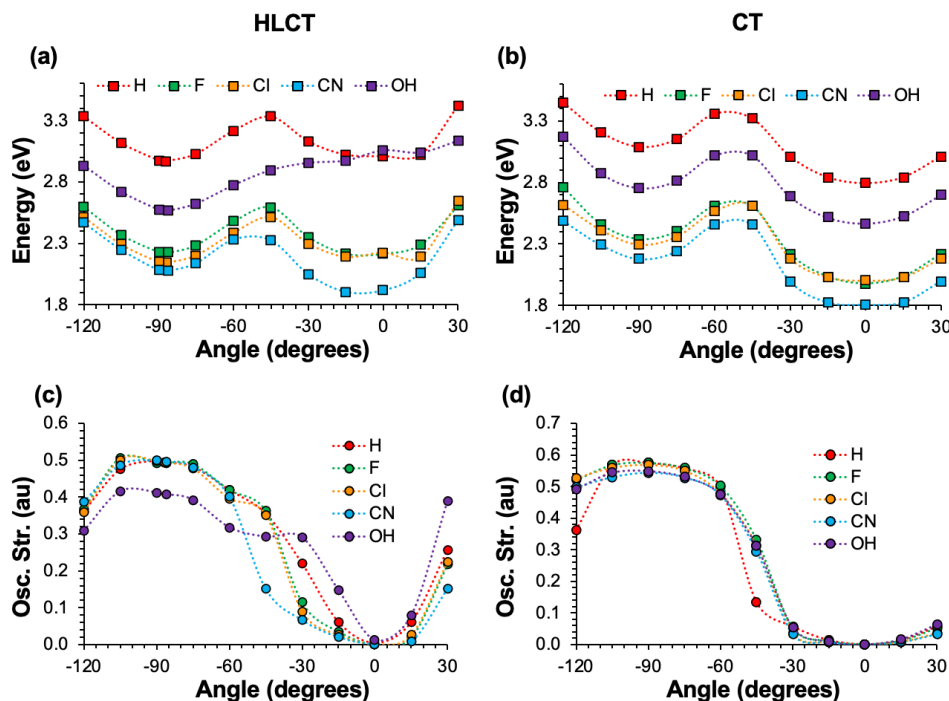


**Figure 4. 9** Potential energy diagrams for the rotation at fixed  $C_1$ - $C_2$  bond lengths of a) HLCT state and b) CT state for the C-substituted derivatives of the *o*-CB-*Ant* dyad with their corresponding oscillator strengths (c-d)

Similar to the carbon-substituted molecules, we investigate the PESs of  $S_1$  states for boron-substituted-*o*-CB-*Ant* with mono- and deca-substitution (Figure 4.10 and 4.11). As shown in Figure 4.10a and 4.10a, the effect of boron substitution on the calculated  $E_{S_1}$  values is significantly less pronounced compared to the case with carbon substitutions, as the effect of boron substitution on calculated  $\Delta E_0$  is much smaller compared to the case with carbon substitutions. In general, both the PESs and the oscillator strengths show a similar trend for boron-substituted-*o*-CB-*Ant* compared to the unsubstituted system. We also note that the CT state ( $\varphi = 0^\circ$ ) is slightly more stabilized compared to the HLCT state ( $\varphi = -87^\circ$ ) with -F, -Cl, and -CN substitutions. As a result, the CT state becomes energetically more favorable even for the partially elongated  $C_1$ - $C_2$  bond lengths (Figure 4.10a) with -Cl and -CN substitutions. In comparison, the energy of the CT state shows a slight increase with -OH substitution for both PESs. We also note that substituent effects, as expected, are significantly larger with deca-substitution as illustrated for the F-



substituted system (Figure 4.10c, d and Figure 4.11c, d). Based on our results with carbon and boron substitutions, it is revealed that both CT and HLCT states become energetically more stable compared to LE state when the substituent shows “-M effect” (e.g., -CN), whereas substituents showing “+M effects” (e.g., -OH) can result in an energy increase for the CT state, especially for partially stretched  $C_1-C_2$  bond lengths.

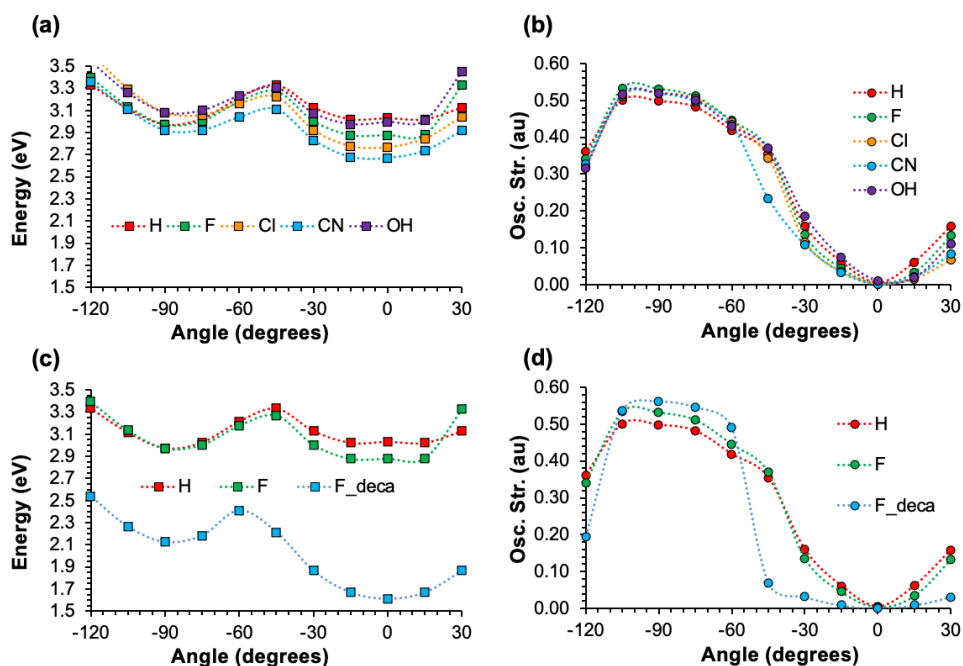


**Figure 4. 10** Potential energy surfaces with respect to  $\varphi$  for partially stretched and fixed  $C_1-C_2$  bond lengths for the B-substituted derivatives of the *o*-CB-Ant. For these surfaces,  $\varphi = -90^\circ$  corresponds to the HLCT state for each system.

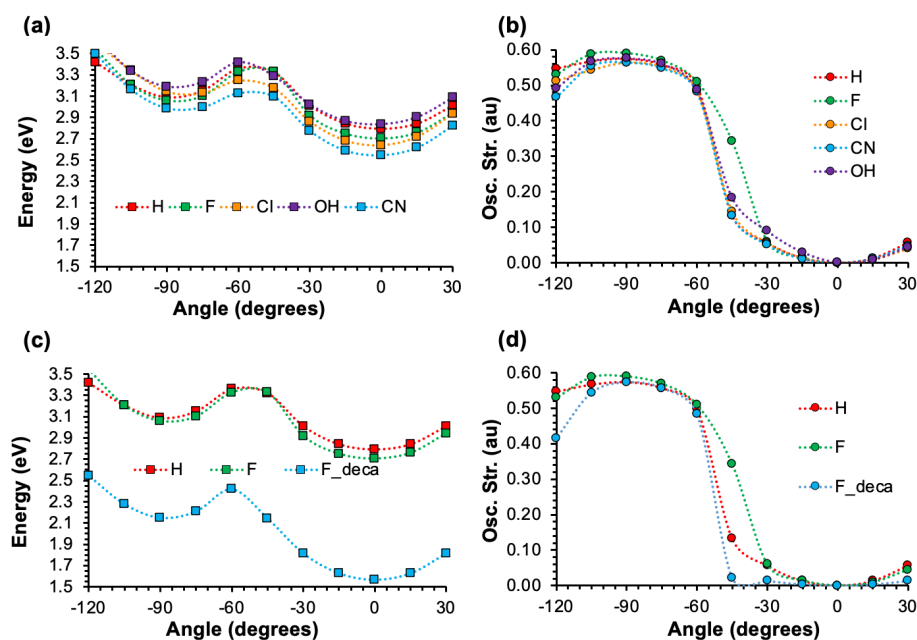


**Figure 4.11** Potential energy surfaces with respect to  $\varphi$  for fully stretched and fixed  $C_1$ - $C_2$  bond lengths for the B-substituted derivatives of the *o*-CB-Ant. For these surfaces,  $\varphi = 0^\circ$  corresponds to the CT state for each system.

### 4.3.3 Effect of the fluorophore

To investigate how the energy levels of the conjugated  $\pi$ -system may affect the photoexcitation processes for *o*-CB-fluorophore systems, anthracene unit was replaced with a  $\pi$ -extended fused acene molecule, pentacene. Energies of the vertical  $S_0 \rightarrow S_1$  transition, and possible  $S_1 \rightarrow S_0$  pathways for *o*-CB-Pentacene (*o*-CB-*Pnt*) molecule are summarized along with the excited-state characteristics in Figure 4.12. As expected, both the vertical  $S_0 \rightarrow S_1$  and  $S_1 \rightarrow S_0$  transitions in the LE state occur via  $\pi \rightarrow \pi^*$  transitions. In addition, the LE state exhibits a very similar geometry compared to the ground state conformation. To see the effect of partially elongated  $C_1$ - $C_2$  bond length and twisted geometry, we perform an excited-state geometry optimization with constrains ( $C_1$ - $C_2 = 2.25 \text{ \AA}$  and  $\varphi = -87^\circ$ ), which corresponds to the local minimum conformation for the HLCT state of *o*-CB-*Ant*. A moderate increase in the oscillator strength is observed for the  $S_1 \rightarrow S_0$  transition for this conformer, however, unlike the case in the *o*-CB-*Ant* system, adiabatic energy of the excited state ( $E_{S_1}$ ) for this conformation shows an increase compared to the same energy for the LE state ( $1.88 \text{ eV} \rightarrow 2.08 \text{ eV}$ ) in the case of *o*-CB-*Pnt*. In this twisted conformation, the contribution of the *o*-carborane-based orbitals only slightly increases, in a similar extent for both HOMO and LUMO levels. As a result, the

$S_1 \rightarrow S_0$  transition shows an LE dominant HLCT character for this conformation in contrast to the twisted conformer of *o*-CB-*Ant*. We should note that this HLCT state shown in Figure 4.12 does not correspond to the minimum point on the  $S_1$  PES for twisted conformations ( $\varphi \approx -90^\circ$ ) as shown in PES in Figure 4.14 (*vide infra*). In fact, the  $C_1$ - $C_2$  bond length was found to be 1.71 Å as a result of the full  $S_1$  optimization of the *o*-CB-*Pnt* with an initial twisted geometry, which also exhibits strong LE character with the similar orbital contributions compared to the conformer of the LE state shown in Figure 4.12. Here, it is clearly seen that the longer  $\pi$ -conjugation and, consequently, the lower LUMO energy of pentacene (Figure 4.13) does not allow an efficient mixing between *o*-CB and pentacene orbitals, resulting in an absence of emission from the HLCT state. Further elongation of  $C_1$ - $C_2$  bond length up to 2.50 Å, along with small  $\varphi$ , results in a third local minimum point having a pure CT character with vanishing oscillator strength for *o*-CB-*Pnt* as well. Similar to the case in *o*-CB-*Ant*, the CT state shows the minimum transition energy (0.88 eV) among the three excited-state conformers. However, unlike the case in *o*-CB-*Ant*, this conformation has a significantly larger  $E_{S_1}$  compared to the other two possible conformations, showing that the relative energy of CT, HLCT, and LE states depend strongly on the energy of the fluorophore LUMO level for such systems.

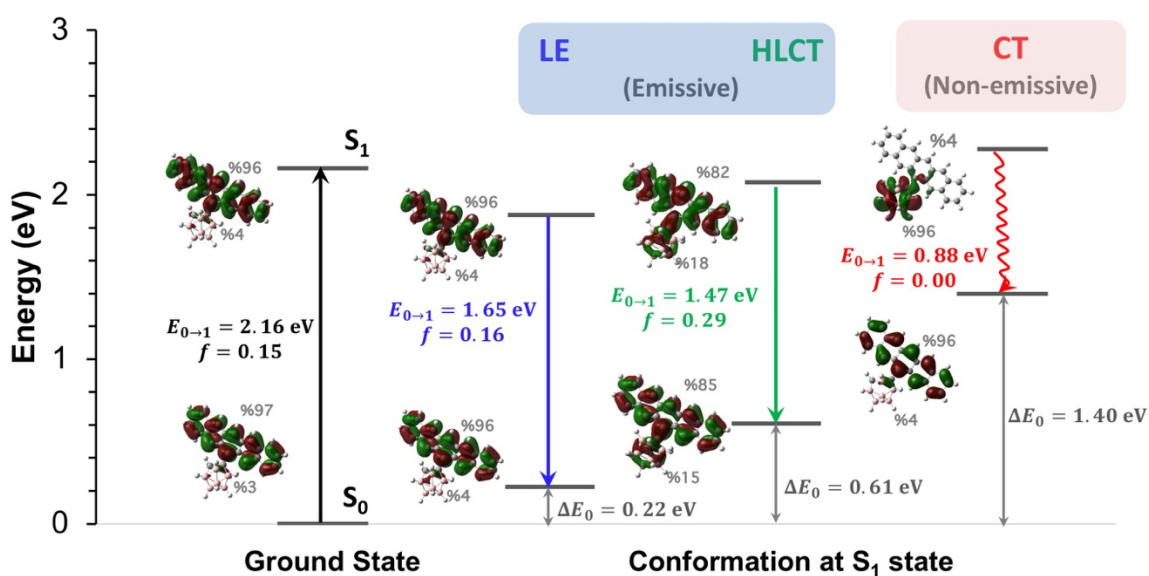


**Figure 4. 12** Illustration of the absorption and potential emission paths along with the corresponding geometries of the *o*-CB-*Pnt* system. The conformations for LE and CT states correspond to the minimum energy points on the  $S_1$  potential energy surface, while the HLCT state is obtained with excited-state geometry optimization with constrains ( $C_1$ - $C_2 = 2.25$  Å and  $\varphi = -87^\circ$ ). % contribution of pentacene and *o*-CB based orbitals to HOMO and LUMO for each transition are shown on the orbital pictures.

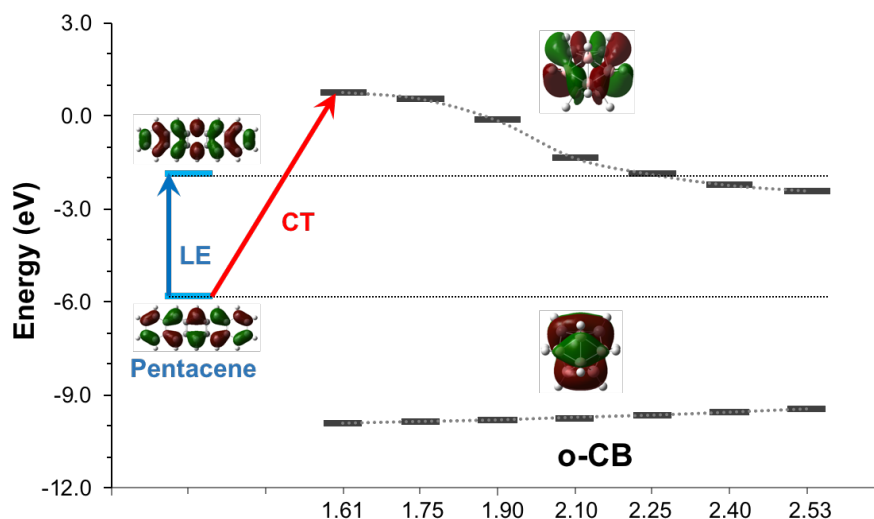


**Figure 4.13** Relative energies of the frontier levels for *o*-CB and Pent moieties with respect to  $C_1$ - $C_2$  distance on *o*-CB.

Finally, Figure 4.14 shows the PESs for the  $S_1$  state of *o*-CB-*Pnt* with respect to changing  $\varphi$  values (Figure 4.14a-c) and  $C_1$ - $C_2$  bond lengths (Figure 4.14g-l), along with the corresponding oscillator strengths for the  $S_1 \rightarrow S_0$  transitions (Figure 4.14d-f and Figure 4.14j-l respectively). For  $C_1$ - $C_2$ =1.65 Å, it is seen that the calculated PES and excited-state character of  $S_1 \rightarrow S_0$  transitions with respect to changing  $\varphi$  values are quite similar to the case in *o*-CB-*Ant*. Similar to the *o*-CB-*Ant* system,  $S_1 \rightarrow S_0$  transitions mainly originate from the  $\pi$ - $\pi^*$  transition on the pentacene  $\pi$ -system for this PES; therefore, the excited state characters and the oscillator strengths do not exhibit a large change through the rotation at this bond length. Interestingly,  $S_1 \rightarrow S_0$  transitions mainly stay as a LE dominant HLCT transition when  $C_1$ - $C_2$  bond length is 2.25 Å, except for  $\varphi = 0^\circ$ . For  $\varphi = 0^\circ$ , the excited state character shows a sharp LE to CT transition, however, calculated  $E_{S_1}$  do not show a local minimum around this  $\varphi$  value. These differences between the calculated PESs of *o*-CB-*Ant* and *o*-CB-*Pnt* originate from the fact that the mixing of pentacene and *o*-carborane-based levels for the LUMO still remains energetically unfavorable for this  $C_1$ - $C_2$  bond length, unlike the case in *o*-CB-*Ant*. On the other hand, when  $C_1$ - $C_2$  is 2.50 Å, the pentacene and carborane-based levels show significant mixing for the LUMOs. For this bond length, the calculated PES and the oscillator strengths show a somewhat similar profile to the case in *o*-CB-*Ant*, except for the fact that even with the elongated  $C_1$ - $C_2$  bond, the CT state does not become the single energy-minimum point for this PES.

Similar to the change in  $\varphi$ 's, the calculated PESs and the oscillator strengths in *o*-CB-*Pnt* with respect to changing C<sub>1</sub>-C<sub>2</sub> bond lengths also exhibit critical differences compared to the same case in *o*-CB-*Ant* (Figure 4.14g-1 and Figure 4.14j-1). For  $\varphi = 87^\circ$ , S<sub>1</sub> state shows an increasing HLCT character with increasing C<sub>1</sub>-C<sub>2</sub> bond length as evident from the calculated oscillator strengths. However, the calculated E<sub>S1</sub> exhibits a continuous increase with increasing C<sub>1</sub>-C<sub>2</sub> bond length whereas the same PES remains rather flat for *o*-CB-*Ant*. As expected from the MO analysis (Figure 4.13), LE → CT transition occurs in longer bond lengths for *o*-CB-*Pnt* when  $\varphi$  is closer to 0°. Interestingly, the energy of the S<sub>1</sub> state decreases with C<sub>1</sub>-C<sub>2</sub> bond elongation after the LE → CT transition is much less pronounced for *o*-CB-*Pnt*, as compared to the case in *o*-CB-*Ant* (Figure 4.7c). As a result, there is a ~0.4 eV difference between the minimum points of LE and CT states, where the LE state is energetically more favorable. Considering the aforementioned importance of CT conformation on emission quenching, it is likely that a larger quantum yield might be expected for the *o*-CB-*Pnt* system due to the energy penalty for the CT state formation in this system.

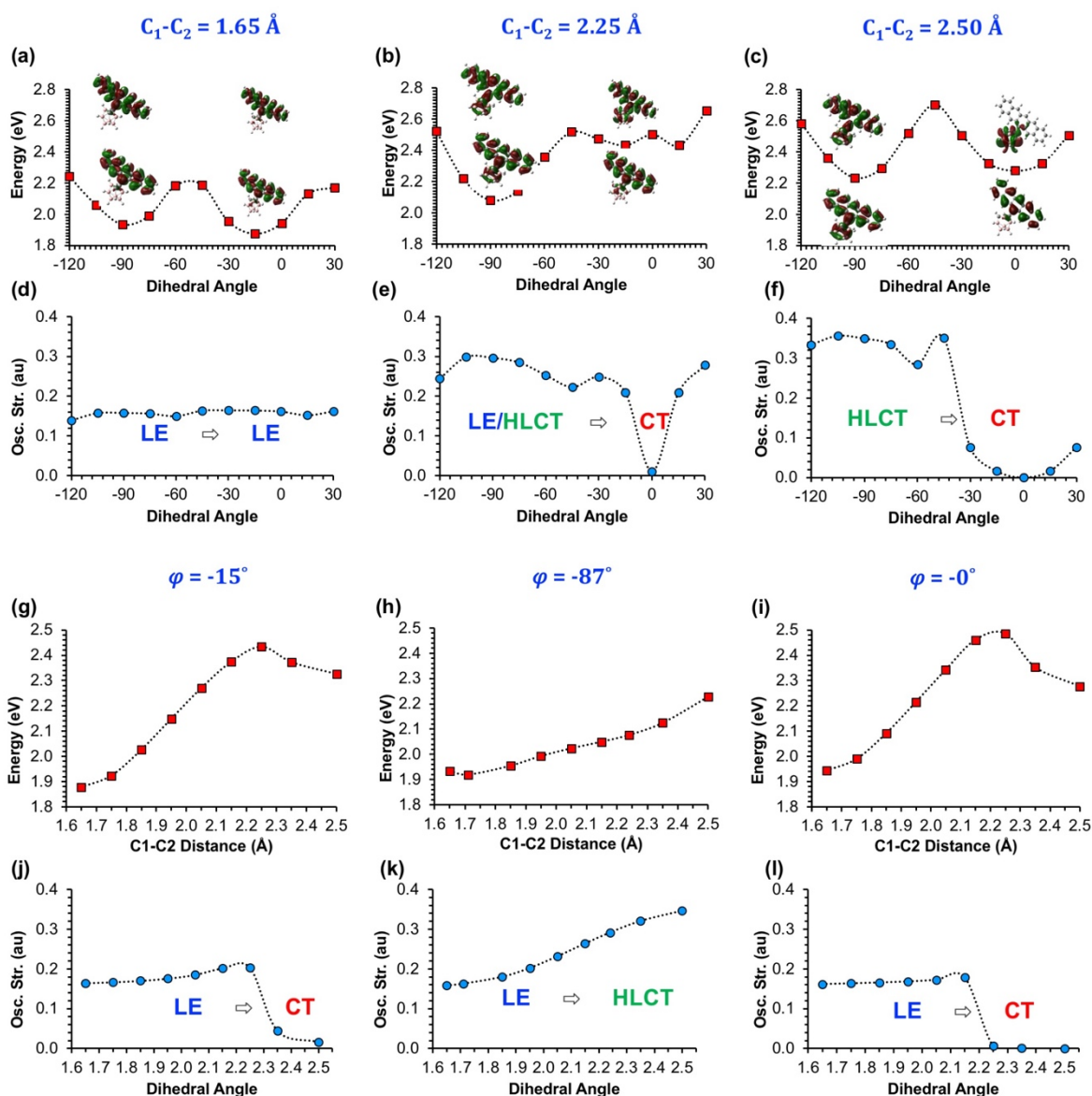


**Figure 4. 14** Potential energy surfaces (PESs) for the adiabatic excited-state energies ( $E_{S1}$ ) with respect to  $\varphi$  at fixed  $C_1$ - $C_2$  bond lengths, (a-c) and calculated oscillator strengths for the corresponding  $S_1 \rightarrow S_0$  (d-f). The same PESs (g-i) and oscillator strengths (j-l) are given with respect to  $C_1$ - $C_2$  bond lengths at fixed  $\varphi$  as well.

## 4.4 Conclusions

In summary, we have studied the PES of the  $S_1$  state for *o*-carborane-anthracene (*o*-CB-*Ant*) using TDDFT methods, with a focus on the nature and energetics of  $S_1 \rightarrow S_0$  transitions with respect to  $C_1$ - $C_2$  bond length in *o*-CB and dihedral angle between *o*-CB and *Ant* moieties. Furthermore, we have evaluated the effect of different substituents (F,

Cl, CN, OH) attached to carbon or boron atoms in *o*-CB, along with a  $\pi$ -extended acene-based fluorophore, pentacene, on the S<sub>1</sub> PES and the resulting photophysical properties. In addition to the emissive LE and HLCT states which correspond to local minimum conformations on S<sub>1</sub> PES, our results show the presence of a dark CT state for *o*-CB-*Ant* as a result of significant C<sub>1</sub>-C<sub>2</sub> bond elongation (C<sub>1</sub>-C<sub>2</sub> = 2.53 Å) in the *o*-CB moiety, which also corresponds to the lowest-energy excited state on the S<sub>1</sub> PES in our investigation. Calculated energy barriers with respect to twist angle ( $\varphi$ ) or C<sub>1</sub>-C<sub>2</sub> bond length are within 0.3-0.4 eV, and for the twisted conformations, C<sub>1</sub>-C<sub>2</sub> bond elongation is shown to occur without an energy penalty indicating that this CT state is energetically accessible on the S<sub>1</sub> surface. These results suggest that the CT state could be an important pathway on the fluorescence quenching mechanism of *o*-CB-*Ant*, and other *o*-CB-*fluorophore* systems with similar structures.

Upon carbon- or boron-substitution on *o*-CB with substituents showing strong -M effect such as -CN, both the CT and HLCT states become energetically even more favorable compared to the LE state; however, substituents showing “+M effects” (e.g., -OH) can result in an energy increase for the CT state, especially for partially stretched C<sub>1</sub>-C<sub>2</sub> bond lengths. This result mainly originates from tuning the LUMO energy level of *o*-CB, which affect the energetics of charge transfer between two moieties. Furthermore, it is shown that the LUMO energy of the fluorophore is also critical for the relative energies of CT, HLCT, and LE states and for the calculated energy barriers on the S<sub>1</sub> PES. When anthracene is replaced with  $\pi$ -extended pentacene as the fluorophore (*o*-CB-*Pnt*), CT state is no longer predicted as the minimum-energy point on S<sub>1</sub> PES as a result of the lower LUMO energy level of *Pnt*, and the calculated energy barriers for C<sub>1</sub>-C<sub>2</sub> bond elongation shows a considerable increase (0.5-0.6 eV). Our results clearly emphasize that the energetics of emissive and non-emissive transitions along with the energy barriers on the S<sub>1</sub> PES can be tuned with respect to substituents or fluorophore energy levels in *o*-CB-*fluorophore* systems, which is expected to guide future experimental work in emissive *o*-CB-*fluorophore* systems and their sensing/optoelectronic applications.

# Chapter 5

## Conclusions and Future Prospects

### 5.1. Conclusions

In this thesis, DFT calculations were carried out to investigate the stability of different size polyhedral borane dianions and the photophysical properties of carborane-based luminescent systems.

In Chapter 3, a theoretical evaluation of relative stabilities and electronic structure for  $[B_nX_n]^{2-}$  clusters ( $n = 10, 12, 13, 14, 15, 16$ ) were presented. Structural and electronic characteristics of  $[B_nX_n]^{2-}$  clusters were examined by comparison with the  $[B_{12}X_{12}]^{2-}$  counterparts with a focus on the substituent effects ( $X = H, F, Cl, Br, CN, BO, OH, NH_2$ ) on the electronic structure, electron detachment energies, formation enthalpies, and charge distributions. Our findings indicate that higher stabilization in terms of HOMO/LUMO and electron detachment energies can be provided by substitution with CN and BO substituents due to strong -M effects. In the case of formation enthalpies for larger boron clusters ( $n \geq 13$ ), the icosahedral barrier was shown to increase with the halogen and CN substitution, whereas it is possible to reduce the icosahedral barrier for the cases of  $X = OH$  and  $NH_2$ . Therefore, it is suggested that destabilizing the  $[B_{12}X_{12}]^{2-}$  cluster with electronic (+M) and symmetry effects induced can be considered as an approach for the synthesis of larger borane clusters.

In Chapter 4, we presented our results from a detailed investigation of the  $S_1$  potential energy surface (PES) of *o*-carborane-anthracene (*o*-CB-*Ant*) with respect to C-C bond length on *o*-CB, and the dihedral angle between *o*-CB and *Ant* moieties. The effects of different substituents (F, Cl, CN, OH) on carbon or boron-substituted *o*-CB, along with a  $\pi$ -extended acene-based fluorophore, pentacene, on the nature and energetics of  $S_1 \rightarrow S_0$  transitions were evaluated. Our results revealed the presence of a non-emissive  $S_1$  state with a pure charge transfer (CT) character for all systems as a result of significant



C-C bond elongation on *o*-CB. It was shown that the dark CT state becomes even more energetically favorable when the substituent shows -M effect (e.g., -CN), whereas substituents showing +M effects (e.g., -OH) can result in an energy increase for the CT state, especially for partially stretched C-C bond lengths. Our findings also demonstrate the dependence of relative energy of the CT state on the LUMO level of the fluorophore, as this state is found to be energetically less favorable compared to other conformations when anthracene is replaced with  $\pi$ -extended pentacene.

## 5.2 Societal Impact and Contribution to Global Sustainability

Materials science is an interdisciplinary field of understanding the structure and material properties as well as the discovery of novel materials. Experimental efforts constitute the center of the investigations since it is the only way to obtain tangible results. However, computational research is also of great importance to understand complex structures and mechanisms, to clarify the electronic features, and to obtain many related material properties as well as to better understand the dynamic response behaviors of the materials. In addition, it is possible to make reliable predictions and verifications of the experimental design beforehand by using computational investigation.

This thesis includes the computational studies of boron-based polyhedral clusters. In order to test, to understand, and to challenge the limits of boron chemistry, it is of great importance to search, and synthesize new stable structures. Previous theoretical studies indicate that there may be stable fullerene-like boron clusters of different sizes. Furthermore, it is also revealed that obtaining highly stable boron hydride dianions beyond the icosahedral borane is also possible. However, these structures have not been isolated yet. Understanding the origins behind this failure is important in terms of guiding new experimental processes. The study given in Chapter 3 is important in this sense.

A good understanding of the photophysical mechanisms is important for the development of new luminescent materials with desired properties. Carborane-fluorophore systems are interesting luminescent systems for many technological applications such as LEDs, lasers, probes, sensors, etc. due to their attractive emission properties; e.g., AIE, multiple emission, and TICT. The results of the study given in Chapter 4 provide an insight in the reasons of low emission efficiency of these systems

in solution state and the effects of some molecular modifications on their photophysical features are demonstrated and reported in an SCI-index journal.

The articles that emerged from the studies presented here are given in the “Curriculum Vitae” section at the end of the thesis.

### 5.3 Future Prospects

Polyhedral boron-based molecules have a quite broad field of research due to their rich chemistry and relatively recently discovered properties compared to carbon-based systems. They are intensively under investigation for a wide range of applications from medicine, catalysis and nonlinear optics to coordination polymers and luminescent materials. However, these studies are still in the expletory stage and there is still a lot to uncover in boron chemistry until their commercialization. For the development of boron chemistry and potential applications of polyhedral (car)boranes, the properties of these clusters need to be well understood. Within the focus of this thesis, the research topics can be extended in the following directions:

- The gas-phase stabilities of dianionic polyhedral boron hydrides were investigated and the possibilities were discussed to obtain larger clusters beyond the icosahedron. Solution state mechanisms can be investigated for the isolation of these larger boranes.
- Our study on the investigation of the photophysical characteristics of carborane-fluorophore systems was limited only to the anthracyl and pentacyl  $\pi$ -conjugated units. The excited state characteristics of other systems exhibiting a low quantum yield in the solutions can be investigated; the similarities and differences between various systems can be revealed.
- Although there are many experimental studies on carborane-based luminescent systems, the number of theoretical studies on the effects of structural modifications on photophysical properties is comparatively limited. Investigating and reporting the influences of different architectural variations on the emission characteristics of these systems will contribute to the formation of a guiding source for the experimental studies.
- Discussions on the carborane-based light-emitting systems are limited to the *ortho*-carborane in our study. Theoretical simulations can be extended to the fluorophore systems incorporating the *meta* and *para* isomers.

Additionally, experimental and computational studies feed off and guide each other. We expect that future experimental discoveries will lead to the expansion of theoretical studies in more diverse directions.



# BIBLIOGRAPHY

- [1] Etimine S.A., "ETİMADEN," <<http://www.etimine.com/>> (6 April 2022).
- [2] S. H. Bauer, "The Structure of Diborane," *Journal of American Chemical Society* **59**, 1096–1103 (1937).
- [3] W. N. Lipscomb and I. R. Epstein, "Boron Hydride Valence Structures. A Topological Approach," *Inorganic Chemistry* **21**, 846 (1982).
- [4] A. Kaczmarczyk, R. D. Dobrott, and W. N. Lipscomb, "REACTIONS OF B<sub>10</sub>H<sub>10</sub>-2 ION," *Proceedings of the National Academy of Sciences* **48**, 729–733 (1962).
- [5] W. N. Lipscomb, A. R. Pitochelli, and M. F. Hawthorne, "PROBABLE STRUCTURE OF THE B<sub>10</sub>H<sub>10</sub> -2 ION," *Journal of American Chemical Society* **81**, 5833–5834 (1959).
- [6] Vlasta. Bonacic-Koutecky, Piercarlo. Fantucci, and Jaroslav. Koutecky, "Quantum chemistry of small clusters of elements of groups Ia, Ib, and IIa: fundamental concepts, predictions, and interpretation of experiments," *Chemical Reviews* **91**, 1035–1108 (1991).
- [7] H. Kato, K. Yamashita, and K. Morokuma, "Ab initio MO study of neutral and cationic boron clusters," *Chemical Physics Letters* **190**, 361–366 (1992).
- [8] H. J. Zhai, L. S. Wang, A. N. Alexandrova, and A. I. Boldyrev, "Electronic structure and chemical bonding of B<sub>5</sub><sup>-</sup> and B<sub>5</sub> by photoelectron spectroscopy and ab initio calculations," *Journal of Chemical Physics* **117**, 7917–7924 (2002).
- [9] A. N. Alexandrova, A. I. Boldyrev, H. J. Zhai, L. S. Wang, E. Steiner, and P. W. Fowler, "Structure and bonding in B<sub>6</sub><sup>-</sup> and B<sub>6</sub>: Planarity and antiaromaticity," *Journal of Physical Chemistry A* **107**, 1359–1369 (2003).
- [10] H. J. Zhai, A. N. Alexandrova, K. A. Birch, A. I. Boldyrev, and L. S. Wang, "Hepta- and Octacoordinate Boron in Molecular Wheels of Eight- and Nine-Atom Boron Clusters: Observation and Confirmation," *Angewandte Chemie - International Edition* **42**, 6004–6008 (2003).
- [11] H. J. Zhai, B. Kiran, J. Li, and L. S. Wang, "Hydrocarbon analogues of boron clusters planarity, aromaticity and antiaromaticity," *Nature Materials* **2**, 827–833 (2003).
- [12] H. J. Zhai, L. S. Wang, A. N. Alexandrova, A. I. Boldyrev, and V. G. Zakrzewski, "Photoelectron Spectroscopy and ab Initio Study of B<sub>3</sub><sup>-</sup> and B<sub>4</sub><sup>-</sup> Anions and Their Neutrals," *Journal of Physical Chemistry A* **107**, 9319–9328 (2003).
- [13] A. N. Alexandrova, A. I. Boldyrev, H.-J. Zhai, and L.-S. Wang, "Electronic Structure, Isomerism, and Chemical Bonding in B<sub>7</sub><sup>-</sup> and B<sub>7</sub>," *The Journal of Physical Chemistry A* **108**, 3509–3517 (2004).
- [14] B. Kiran, S. Bulusu, H. J. Zhai, S. Yoo, X. C. Zeng, and L. S. Wang, "Planar-to-tubular structural transition in boron clusters: B<sub>20</sub> as the embryo of single-walled boron nanotubes," *Proc Natl Acad Sci U S A* **102**, 961–964 (2005).
- [15] A. N. Alexandrova, A. I. Boldyrev, H.-J. Zhai, and L.-S. Wang, "All-boron aromatic clusters as potential new inorganic ligands and building blocks in chemistry," *Coordination Chemistry Reviews* **250**, 2811–2866 (2006).

- [16] N. Gonzalez Szwacki, A. Sadrzadeh, and B. I. Yakobson, "B80 Fullerene: An Ab Initio Prediction of Geometry, Stability, and Electronic Structure," *Physical Review Letters* **98**, 166804 (2007).
- [17] E. Oger, N. R. M. Crawford, R. Kelting, P. Weis, M. M. Kappes, and R. Ahlrichs, "Boron cluster cations: Transition from planar to cylindrical structures," *Angewandte Chemie - International Edition* **46**, 8503–8506 (2007).
- [18] L.-L. Pan, J. Li, and L.-S. Wang, "Low-lying isomers of the B<sub>9</sub><sup>-</sup> boron cluster: The planar molecular wheel versus three-dimensional structures," *The Journal of Chemical Physics* **129**, 024302 (2008).
- [19] A. P. Sergeeva, D. Yu. Zubarev, H.-J. Zhai, A. I. Boldyrev, and L.-S. Wang, "A Photoelectron Spectroscopic and Theoretical Study of B<sub>16</sub><sup>-</sup> and B<sub>16</sub>(2-): An All-Boron Naphthalene," *Journal of American Chemical Society* **130**, 7244–7246 (2008).
- [20] W. Huang, A. P. Sergeeva, H. J. Zhai, B. B. Averkiev, L. S. Wang, and A. I. Boldyrev, "A concentric planar doubly  $\pi$ -aromatic B<sub>19</sub> cluster," *Nature Chemistry* **2**, 202–206 (2010).
- [21] A. P. Sergeeva, B. B. Averkiev, H.-J. Zhai, A. I. Boldyrev, and L.-S. Wang, "All-boron analogues of aromatic hydrocarbons: B<sub>17</sub><sup>-</sup> and B<sub>18</sub><sup>-</sup>," *The Journal of Chemical Physics* **134**, 224304 (2011).
- [22] Z. A. Piazza, W.-L. Li, C. Romanescu, A. P. Sergeeva, L.-S. Wang, and A. I. Boldyrev, "A photoelectron spectroscopy and *ab initio* study of B<sub>21</sub><sup>-</sup>: Negatively charged boron clusters continue to be planar at 21," *The Journal of Chemical Physics* **136**, 104310 (2012).
- [23] A. P. Sergeeva, Z. A. Piazza, C. Romanescu, W. L. Li, A. I. Boldyrev, and L. S. Wang, "B<sub>22</sub><sup>-</sup> and B<sub>23</sub><sup>-</sup>: All-boron analogues of anthracene and phenanthrene," *Journal of American Chemical Society* **134**, 18065–18073 (2012).
- [24] I. A. Popov, Z. A. Piazza, W.-L. Li, L.-S. Wang, and A. I. Boldyrev, "A combined photoelectron spectroscopy and *ab initio* study of the quasi-planar B<sub>24</sub><sup>-</sup> cluster," *The Journal of Chemical Physics* **139**, 144307 (2013).
- [25] Z. A. Piazza, I. A. Popov, W.-L. Li, R. Pal, X. Cheng Zeng, A. I. Boldyrev, and L.-S. Wang, "A photoelectron spectroscopy and *ab initio* study of the structures and chemical bonding of the B<sub>25</sub><sup>-</sup> cluster," *The Journal of Chemical Physics* **141**, 034303 (2014).
- [26] W.-L. Li, R. Pal, Z. A. Piazza, X. C. Zeng, and L.-S. Wang, "B<sub>27</sub><sup>-</sup>: Appearance of the smallest planar boron cluster containing a hexagonal vacancy," *The Journal of Chemical Physics* **142**, 204305 (2015).
- [27] Y.-J. Wang, Y.-F. Zhao, W.-L. Li, T. Jian, Q. Chen, X.-R. You, T. Ou, X.-Y. Zhao, H.-J. Zhai, et al., "Observation and characterization of the smallest borospherene, B<sub>28</sub><sup>-</sup> and B<sub>28</sub>," *The Journal of Chemical Physics* **144**, 064307 (2016).
- [28] X. M. Luo, T. Jian, L. J. Cheng, W. L. Li, Q. Chen, R. Li, H. J. Zhai, S. D. Li, A. I. Boldyrev, et al., "B<sub>26</sub><sup>-</sup>: The smallest planar boron cluster with a hexagonal vacancy and a complicated potential landscape," *Chemical Physics Letters* **683**, 336–341 (2017).
- [29] L.-S. Wang, "Photoelectron spectroscopy of size-selected boron clusters: from planar structures to borophenes and borospherenes," *International Reviews in Physical Chemistry* **35**, 69–142 (2016).

- [30] T. B. Tai, N. M. Tam, and M. T. Nguyen, "Structure of boron clusters revisited, B<sub>n</sub> with n=14–20," *Chemical Physics Letters* **530**, 71–76 (2012).
- [31] T. B. Tai, N. M. Tam, and M. T. Nguyen, "The Boron conundrum: the case of cationic clusters B<sub>n</sub><sup>+</sup> with n = 2–20," *Theoretical Chemistry Accounts* **131**, 1241 (2012).
- [32] Z. A. Piazza, H.-S. Hu, W.-L. Li, Y.-F. Zhao, J. Li, and L.-S. Wang, "Planar hexagonal B<sub>36</sub> as a potential basis for extended single-atom layer boron sheets," *Nature Communications* **5**, 3113 (2014).
- [33] W. L. Li, Q. Chen, W. J. Tian, H. Bai, Y. F. Zhao, H. S. Hu, J. Li, H. J. Zhai, S. D. Li, et al., "The B<sub>35</sub> cluster with a double-hexagonal vacancy: A new and more flexible structural motif for borophene," *Journal of American Chemical Society* **136**, 12257–12260 (2014).
- [34] Q. Chen, W. J. Tian, L. Y. Feng, H. G. Lu, Y. W. Mu, H. J. Zhai, S. D. Li, and L. S. Wang, "Planar B<sub>38</sub><sup>-</sup> and B<sub>37</sub><sup>-</sup> clusters with a double-hexagonal vacancy: molecular motifs for borophenes," *Nanoscale* **9**, 4550–4557 (2017).
- [35] Q. Chen, W. L. Li, X. Y. Zhao, H. R. Li, L. Y. Feng, H. J. Zhai, S. D. Li, and L. S. Wang, "B<sub>33</sub><sup>-</sup> and B<sub>34</sub><sup>-</sup>: Aromatic Planar Boron Clusters with a Hexagonal Vacancy," *European Journal of Inorganic Chemistry* **2017**, 4546–4551 (2017).
- [36] A. B. Rahane and V. Kumar, "B<sub>84</sub>: a quasi-planar boron cluster stabilized with hexagonal holes," *Nanoscale* **7**, 4055–4062 (2015).
- [37] H. J. Zhai, Y. F. Zhao, W. L. Li, Q. Chen, H. Bai, H. S. Hu, Z. A. Piazza, W. J. Tian, H. G. Lu, et al., "Observation of an all-boron fullerene," *Nature Chemistry* **6**, 727–731 (2014).
- [38] J. Zhao, L. Wang, F. Li, and Z. Chen, "B<sub>80</sub> and Other Medium-Sized Boron Clusters: Core–Shell Structures, Not Hollow Cages," *The Journal of Physical Chemistry A* **114**, 9969–9972 (2010).
- [39] A. Quandt and I. Boustani, "Boron Nanotubes," *ChemPhysChem* **6**, 2001–2008 (2005).
- [40] D. Yu. Zubarev and A. I. Boldyrev, "Comprehensive analysis of chemical bonding in boron clusters," *Journal of Computational Chemistry* **28**, 251–268 (2007).
- [41] D. Yu. Zubarev and A. I. Boldyrev, "Developing paradigms of chemical bonding: adaptive natural density partitioning," *Physical Chemistry Chemical Physics* **10**, 5207 (2008).
- [42] K. Wade, "The structural significance of the number of skeletal bonding electron-pairs in carboranes, the higher boranes and borane anions, and various transition-metal carbonyl cluster compounds," *Journal of the Chemical Society D: Chemical Communications* **9**, 792 (1971).
- [43] K. Wade, "Structural and Bonding Patterns in Cluster Chemistry," in *Advances in Inorganic Chemistry and Radiochemistry* **18** (1976).
- [44] D. M. P. Mingos, "Polyhedral Skeletal Electron Pair Approach," *Accounts of Chemical Research* **17**, 311–319 (1984).
- [45] A. Masago, K. Shirai, and H. Katayama-Yoshida, "Crystal stability of  $\alpha$ - and  $\beta$ -boron," *Physical Review B* **73**, 104102 (2006).
- [46] R. N. Grimes, "Boron Clusters Come of Age," *Journal of Chemical Education* **81**, 657 (2004).

- [47] S. Körbe, P. J. Schreiber, and J. Michl, "Chemistry of the Carba-closo-dodecaborate(-) anion, CB<sub>11</sub>H<sub>12</sub>-," *Chemical Reviews* **106**, 5208–5249 (2006).
- [48] M. Scholz and E. Hey-Hawkins, "Carbaboranes as Pharmacophores: Properties, Synthesis, and Application Strategies," *Chemical Reviews* **111**, 7035–7062 (2011).
- [49] J. A. Wunderlich and W. N. Lipscomb, "STRUCTURE OF B<sub>12</sub>H<sub>12</sub> - 2 ION," *Journal of American Chemical Society* **82**, 4427–4428 (1960).
- [50] F. Klanberg, D. R. Eaton, L. J. Guggenberger, and E. L. Muetterties, "Chemistry of boranes. XXVIII. New polyhedral borane anions, B<sub>8</sub>H<sub>8</sub><sup>2-</sup>, B<sub>8</sub>H<sub>8</sub><sup>-</sup>, and B<sub>7</sub>H<sub>7</sub><sup>2-</sup>," *Inorganic Chemistry* **6**, 1271–1281 (1967).
- [51] F. Klanberg and E. L. Muetterties, "Chemistry of Boranes. XXVII. New Polyhedral Borane Anions, B<sub>9</sub>H<sub>9</sub><sup>2-</sup> and B<sub>11</sub>H<sub>11</sub><sup>2-</sup>," *Inorganic Chemistry* **5**, 1955–1960 (1966).
- [52] J. L. Boone, "Isolation of the Hexahydroclosohexaborate(2-) Anion, B<sub>6</sub>H<sub>6</sub><sup>2-</sup>," *Journal of American Chemical Society* **86**, 5036–5036 (1964).
- [53] M. L. McKee, Z. X. Wang, and P. von Ragué Schleyer, "Ab initio study of the hypercloso boron hydrides B(n)H(n) and B(n)H(n)<sup>-</sup>. Exceptional stability of neutral B<sub>13</sub>H<sub>13</sub>," *Journal of American Chemical Society* **122**, 4781–4793 (2000).
- [54] H. Zhao, J. Zhou, and P. Jena, "Stability of B<sub>12</sub>(CN)<sub>12</sub><sup>2-</sup>: Implications for Lithium and Magnesium Ion Batteries," *Angewandte Chemie - International Edition* **55**, 3704–3708 (2016).
- [55] E. Aprà, J. Warneke, S. S. Xantheas, and X.-B. Wang, "A benchmark photoelectron spectroscopic and theoretical study of the electronic stability of [B<sub>12</sub>H<sub>12</sub>]<sup>2-</sup>," *The Journal of Chemical Physics* **150**, 164306 (2019).
- [56] T. Peymann, A. Herzog, C. B. Knobler, and M. F. Hawthorne, "Aromatic Polyhedral Hydroxyborates: Bridging Boron Oxides and Boron Hydrides," *Angewandte Chemie International Edition* **38**, 1061–1064 (1999).
- [57] A. Maderna, C. B. Knobler, and M. F. Hawthorne, "Twelvefold Functionalization of an Icosahedral Surface by Total Esterification of [B<sub>12</sub>(OH)<sub>12</sub>]<sup>2-</sup>: 12(12)-Closomers," *Angewandte Chemie International Edition* **40**, 1661–1664 (2001).
- [58] E. L. Muetterties, J. H. Balthis, Y. T. Chia, W. H. Knoth, and H. C. Miller, "Chemistry of Boranes. VIII. Salts and Acids of B<sub>10</sub>H<sub>10</sub><sup>2-</sup> and B<sub>12</sub>H<sub>12</sub><sup>2-</sup>," *Inorganic Chemistry* **3**, 444–451 (1964).
- [59] J. Warneke, G. L. Hou, E. Aprà, C. Jenne, Z. Yang, Z. Qin, K. Kowalski, X. bin Wang, and S. S. Xantheas, "Electronic Structure and Stability of [B<sub>12</sub>X<sub>12</sub>]<sup>2-</sup> (X = F-At): A Combined Photoelectron Spectroscopic and Theoretical Study," *Journal of American Chemical Society* **139**, 14749–14756 (2017).
- [60] D. v. Peryshkov, A. A. Popov, and S. H. Strauss, "Direct Perfluorination of K<sub>2</sub>B<sub>12</sub>H<sub>12</sub> in Acetonitrile Occurs at the Gas Bubble–Solution Interface and Is Inhibited by HF. Experimental and DFT Study of Inhibition by Protic Acids and Soft, Polarizable Anions," *Journal of American Chemical Society* **131**, 18393–18403 (2009).
- [61] M. R. Fagiani, L. Liu Zeonjuk, T. K. Esser, D. Gabel, T. Heine, K. R. Asmis, and J. Warneke, "Opening of an icosahedral boron framework: A combined infrared spectroscopic and computational study," *Chemical Physics Letters* **625**, 48–52 (2015).

- [62] J. A. Dopke, D. R. Powell, and D. F. Gaines, "Synthesis and Characterization of New 19-Vertex Macropolyhedral Boron Hydrides," *Inorganic Chemistry* **39**, 463–467 (2000).
- [63] J. Bicerano, D. S. Marynick, and W. N. Lipscomb, "Molecular orbital studies on large closo boron hydrides," *Inorganic Chemistry* **17**, 3443–3453 (1978).
- [64] P. R. von Schleyer, K. Najafian, and A. M. Mebel, "The Large closo-Borane Dianions,  $B_nH_n^{2-}$  ( $n = 13-17$ ) Are Aromatic, Why Are They Unknown?," *Inorganic Chemistry* **37**, 6765–6772 (American Chemical Society, 1998).
- [65] L. D. Brown and W. N. Lipscomb, "Closo boron hydrides with 13 to 24 boron atoms," *Inorganic Chemistry* **16**, 2989–2996 (1977).
- [66] A. Burke, D. Ellis, B. T. Giles, B. E. Hodson, S. A. Macgregor, G. M. Rosair, and A. J. Welch, "Beyond the Icosahedron: The First 13-Vertex Carborane," *Angewandte Chemie International Edition* **42**, 225–228 (2003).
- [67] A. S. F. Boyd, A. Burke, D. Ellis, D. Ferrer, B. T. Giles, M. A. Laguna, R. McIntosh, S. A. Macgregor, D. L. Ormsby, et al., "Supraicosahedral (metalla) carboranes," *Pure and Applied Chemistry* **75**, 1325–1333 (2003).
- [68] F. Zheng, T. H. Yui, J. Zhang, and Z. Xie, "Synthesis and X-ray characterization of 15- and 16-vertex closo-carboranes," *Nature Communications* **11**, 5943 (2020).
- [69] D. K. Roy, S. Ghosh, and J.-F. Halet, "Beyond the Icosahedron: The Quest for High-Nuclearity Supraicosahedral Metallaboranes," *Journal of Cluster Science* **25**, 225–237 (2014).
- [70] D. K. Roy, B. Mondal, P. Shankhari, R. S. Anju, K. Geetharani, S. M. Mobin, and S. Ghosh, "Supraicosahedral Polyhedra in Metallaboranes: Synthesis and Structural Characterization of 12-, 15-, and 16-Vertex Rhodaboranes," *Inorganic Chemistry* **52**, 6705–6712 (2013).
- [71] D. K. Roy, S. K. Bose, R. S. Anju, B. Mondal, V. Ramkumar, and S. Ghosh, "Boron Beyond the Icosahedral Barrier: A 16-Vertex Metallaborane," *Angewandte Chemie International Edition* **52**, 3222–3226 (2013).
- [72] J. Zhang and Z. Xie, "Recent Progress in the Chemistry of Supercarboranes," *Chemistry - An Asian Journal* **5**, 1742–1757 (2010).
- [73] J. Zhang, L. Deng, H.-S. Chan, and Z. Xie, "Role of C,C'-Linkage in the Formation and Stabilization of Supercarboranes. Synthesis and Structure of Carbon-Atoms-Apart 13-Vertex Carborane and 14-Vertex Metallocarborane," *Journal of American Chemical Society* **129**, 18–19 (2007).
- [74] L. Deng, H.-S. Chan, and Z. Xie, "Synthesis, Reactivity, and Structural Characterization of a 14-Vertex Carborane," *Angewandte Chemie International Edition* **44**, 2128–2131 (2005).
- [75] J. Zhang, F. Zheng, and Z. Xie, "Synthesis and Characterization of 14-Vertex Carboranes," *Organometallics* **32**, 7399–7406 (2013).
- [76] D. Ellis, M. E. Lopez, R. McIntosh, G. M. Rosair, and A. J. Welch, "Fourteen-vertex homo- and heterobimetallic metallocarboranes," *Chemical Communications*, 1917 (2005).
- [77] R. D. McIntosh, D. Ellis, G. M. Rosair, and A. J. Welch, "A 15-Vertex Heteroborane," *Angewandte Chemie* **118**, 4419–4422 (2006).
- [78] L. Deng, J. Zhang, H.-S. Chan, and Z. Xie, "Synthesis and Structure of 14- and 15-Vertex Ruthenacarboranes," *Angewandte Chemie International Edition* **45**, 4309–4313 (2006).



- [79] X. Zhao, Z. Yang, H. Chen, Z. Wang, X. Zhou, and H. Zhang, "Progress in three-dimensional aromatic-like closo-dodecaborate," *Coordination Chemistry Reviews* **444**, 214042 (2021).
- [80] R. N. Grimes, "Icosahedral Carboranes: Closo-CB11 Clusters," in *Carboranes* (Elsevier, 2016).
- [81] C. Douvris and J. Michl, "Update 1 of: Chemistry of the Carba- closo - dodecaborate(-) Anion,  $\text{CB}_{11}\text{H}_{12}^-$ ," *Chemical Reviews* **113**, PR179–PR233 (2013).
- [82] A. V. Okotrub, L. G. Bulusheva, and V. V. Volkov, "Electron interactions in the closo-carboranes 1,2- and 1,7-C<sub>2</sub>B<sub>10</sub>H<sub>12</sub>," *Journal of Molecular Structure* **520**, 33–38 (2000).
- [83] N. Tsuboya, M. Lamrani, R. Hamasaki, M. Ito, M. Mitsuishi, T. Miyashita, and Y. Yamamoto, "Nonlinear optical properties of novel carborane-ferrocene conjugated dyads. Electron-withdrawing characteristics of carboranes," *Journal of Materials Chemistry* **12**, 2701–2705 (2002).
- [84] O. Crespo, M. C. Gimeno, A. Laguna, I. Ospino, G. Aullón, and J. M. Oliva, "Organometallic gold complexes of carborane. Theoretical comparative analysis of ortho, meta, and para derivatives and luminescence studies," *Dalton Transactions*, 3807 (2009).
- [85] A. Weller, "The two faces of carboranes," *Nature Chemistry* **3**, 577–578 (2011).
- [86] R. N. Grimes, "Icosahedral Carboranes: 1,7-C<sub>2</sub>B<sub>10</sub>H<sub>12</sub> and 1,12-C<sub>2</sub>B<sub>10</sub>H<sub>12</sub>," in *Carboranes* (Elsevier, 2016).
- [87] R. N. Grimes, "Icosahedral Carboranes: 1,2-C<sub>2</sub>B<sub>10</sub>H<sub>12</sub>," in *Carboranes* (Elsevier, 2016).
- [88] Hosmane Narayan S., *Boron Science*, N. S. Hosmane, Ed. (CRC Press, 2012).
- [89] A. F. Armstrong and J. F. Valliant, "The bioinorganic and medicinal chemistry of carboranes: From new drug discovery to molecular imaging and therapy," *Dalton Transactions*, 4240–4251 (2007).
- [90] Grimes Russel N., *Carboranes*, 3rd ed. (Academic Press, 2016).
- [91] R. N. Grimes, "Carboranes in the chemist's toolbox," *Dalton Transactions* **44**, 5939–5956 (2015).
- [92] R. F. Barth, P. Mi, and W. Yang, "Boron delivery agents for neutron capture therapy of cancer," *Cancer Communications* **38**, 1–15 (2018).
- [93] R. Núñez, M. Tarrés, A. Ferrer-Ugalde, F. F. de Biani, and F. Teixidor, "Electrochemistry and Photoluminescence of Icosahedral Carboranes, Boranes, Metallacarboranes, and Their Derivatives," *Chemical Reviews* **116**, 14307–14378 (2016).
- [94] H. Naito, K. Nishino, Y. Morisaki, K. Tanaka, and Y. Chujo, "Highly-efficient solid-state emissions of anthracene-o-carborane dyads with various substituents and their thermochromic luminescence properties," *Journal of Materials Chemistry C* **5**, 10047–10054 (2017).
- [95] J. C. Axtell, L. M. A. Saleh, E. A. Qian, A. I. Wixtrom, and A. M. Spokoyny, "Synthesis and Applications of Perfunctionalized Boron Clusters," *Inorganic Chemistry* **57**, 2333–2350 (2018).
- [96] M. Yoshida, D. J. Crowther, and R. F. Jordan, "Synthesis, Structure, and Reactivity of a Novel Hafnium Carboranyl Hydride Complex," *Organometallics* **16**, 1349–1351 (1997).

- [97] G. G. Hlatky, H. W. Turner, and R. R. Eckman, "Ionic, base-free zirconocene catalysts for ethylene polymerization," *Journal of American Chemical Society* **111**, 2728–2729 (1989).
- [98] D.-H. Kim, J. H. Won, S.-J. Kim, J. Ko, S. H. Kim, S. Cho, and S. O. Kang, "Dicarbollide Analogues of the Constrained-Geometry Polymerization Catalyst," *Organometallics* **20**, 4298–4300 (2001).
- [99] T. Dodge, M. A. Curtis, J. M. Russell, M. Sabat, M. G. Finn, and R. N. Grimes, "Titanium and Zirconium  $\text{Et}_2\text{C}_2\text{B}_4\text{H}_4$ -Metal-Phosphine Complexes: Synthesis, Characterization, and Ethylene Polymerization Activity<sup>1</sup>," *Journal of American Chemical Society* **122**, 10573–10580 (2000).
- [100] P. Altamura and A. Grassi, "Crystalline Alternating Sequences Identified in Ethylene-*co*-norbornene Polymers Produced by the  $(\eta^5\text{-C}_2\text{B}_9\text{H}_{11})\text{Zr}(\text{NEt}_2)_2(\text{NHEt}_2)\text{-Al}^i\text{Bu}_3$  Catalyst," *Macromolecules* **34**, 9197–9200 (2001).
- [101] X. Wen, K. Cao, J. Wu, C. Zhang, X. Li, L. Jiang, and J. Yang, "Free Radical Polymerization of *o*-Carborane Functionalized Styrene: Effect of Substitution Position at Carbon and Boron," *ChemistrySelect* **6**, 4491–4494 (2021).
- [102] O. Tutusaus, S. Delfosse, F. Simal, A. Demonceau, A. F. Noels, R. Núñez, C. Viñas, and F. Teixidor, "Half-sandwich ruthenium complexes for the controlled radical polymerisation of vinyl monomers," *Inorganic Chemistry Communications* **5**, 941–945 (2002).
- [103] J. F. Valliant, K. J. Guenther, A. S. King, P. Morel, P. Schaffer, O. O. Sogbein, and K. A. Stephenson, "The medicinal chemistry of carboranes," *Coordination Chemistry Reviews* **232**, 173–230 (2002).
- [104] I. B. Sivaev and V. v. Bregadze, "Polyhedral Boranes for Medical Applications: Current Status and Perspectives," *European Journal of Inorganic Chemistry* **2009**, 1433–1450 (2009).
- [105] T. Yamamoto, K. Nakai, and A. Matsumura, "Boron neutron capture therapy for glioblastoma," *Cancer Letters* **262**, 143–152 (2008).
- [106] N. B. Pepper, W. Stummer, and H. T. Eich, "The use of radiosensitizing agents in the therapy of glioblastoma multiforme—a comprehensive review," *Strahlentherapie und Onkologie* (2022).
- [107] R. F. Barth, J. A. Coderre, M. G. H. Vicente, and T. E. Blue, "Boron Neutron Capture Therapy of Cancer: Current Status and Future Prospects," *Clinical Cancer Research* **11**, 3987–4002 (2005).
- [108] Z. J. Leśnikowski, "Challenges and Opportunities for the Application of Boron Clusters in Drug Design," *Journal of Medicinal Chemistry* **59**, 7738–7758 (2016).
- [109] S. P. Fisher, A. W. Tomich, J. Guo, and V. Lavallo, "Teaching an old dog new tricks: New directions in fundamental and applied: Closo-carborane anion chemistry," *Chemical Communications* **55**, 1684–1701 (2019).
- [110] D. Aurbach, Z. Lu, A. Schechter, Y. Gofer, H. Gizbar, R. Turgeman, Y. Cohen, M. Moshkovich, and E. Levi, "Prototype systems for rechargeable magnesium batteries," *Nature* **407**, 724–727 (2000).
- [111] H. D. Yoo, I. Shterenberg, Y. Gofer, G. Gershinsky, N. Pour, and D. Aurbach, "Mg rechargeable batteries: an on-going challenge," *Energy & Environmental Science* **6**, 2265 (2013).

- [112] J. Muldoon, C. B. Bucur, A. G. Oliver, T. Sugimoto, M. Matsui, H. S. Kim, G. D. Allred, J. Zajicek, and Y. Kotani, "Electrolyte roadblocks to a magnesium rechargeable battery," *Energy & Environmental Science* **5**, 5941 (2012).
- [113] D. Aurbach, G. S. Suresh, E. Levi, A. Mitelman, O. Mizrahi, O. Chusid, and M. Brunelli, "Progress in Rechargeable Magnesium Battery Technology," *Advanced Materials* **19**, 4260–4267 (2007).
- [114] Scott. G. McArthur, L. Geng, J. Guo, and V. Lavallo, "Cation reduction and comproportionation as novel strategies to produce high voltage, halide free, carborane based electrolytes for rechargeable Mg batteries," *Inorganic Chemistry Frontiers* **2**, 1101–1104 (2015).
- [115] O. Tutusaus, R. Mohtadi, T. S. Arthur, F. Mizuno, E. G. Nelson, and Y. v. Sevryugina, "An Efficient Halogen-Free Electrolyte for Use in Rechargeable Magnesium Batteries," *Angewandte Chemie International Edition* **54**, 7900–7904 (2015).
- [116] R. Mohtadi and F. Mizuno, "Magnesium batteries: Current state of the art, issues and future perspectives," *Beilstein Journal of Nanotechnology* **5**, 1291–1311 (2014).
- [117] C. B. Bucur, T. Gregory, A. G. Oliver, and J. Muldoon, "Confession of a Magnesium Battery," *The Journal of Physical Chemistry Letters* **6**, 3578–3591 (2015).
- [118] B. P. Dash, R. Satapathy, J. A. Maguire, and N. S. Hosmane, "Polyhedral boron clusters in materials science," *New Journal of Chemistry* **35**, 1955 (2011).
- [119] D. G. Allis and J. T. Spencer, "Polyhedral-Based Nonlinear Optical Materials. 2. Theoretical Investigation of Some New High Nonlinear Optical Response Compounds Involving Polyhedral Bridges with Charged Aromatic Donors and Acceptors," *Inorganic Chemistry* **40**, 3373–3380 (2001).
- [120] D. M. Murphy, D. M. P. Mingos, and J. M. Forward, "Synthesis of icosahedral carboranes for second-harmonic generation. Part 1," *Journal of Materials Chemistry* **3**, 67 (1993).
- [121] D. M. Murphy, D. M. P. Mingos, J. L. Haggitt, H. R. Powell, S. A. Westcott, T. B. Marder, N. J. Taylor, and D. R. Kanis, "Synthesis of icosahedral carboranes for second-harmonic generation. Part 2," *Journal of Materials Chemistry* **3**, 139 (1993).
- [122] B. Grüner, Z. Janoušek, B. T. King, J. N. Woodford, C. H. Wang, V. Vřetečka, and J. Michl, "Synthesis of 12-Substituted 1-Carba-*closo*-dodecaborate Anions and First Hyperpolarizability of the 12-C<sub>7</sub>H<sub>6</sub><sup>+</sup>-CB<sub>11</sub>H<sub>11</sub> Ylide [*J. Am. Chem. Soc.* **1999**, *121*, 3122–3126].," *Journal of American Chemical Society* **122**, 11274–11274 (2000).
- [123] M. Lamrani, R. Hamasaki, Y. Yamamoto, M. Mitsuishi, and T. Miyashita, "Carborane–fullerene hybrids as a seemingly attractive–attractive dyad with high hyperpolarizability," *Chemical Communications*, 1595–1596 (2000).
- [124] R. Hamasaki, M. Ito, M. Lamrani, M. Mitsuishi, T. Miyashita, and Y. Yamamoto, "Nonlinear optical studies of fullerene–arylethyne hybrids," *J. Mater. Chem.* **13**, 21–26 (2003).
- [125] N. Tsuboya, M. Lamrani, R. Hamasaki, M. Ito, M. Mitsuishi, T. Miyashita, and Y. Yamamoto, "Nonlinear optical properties of novel carborane–

- ferrocene conjugated dyads. Electron-withdrawing characteristics of carboranes,” *J. Mater. Chem.* **12**, 2701–2705 (2002).
- [126] R. Bernard, D. Cornu, P. L. Baldeck, J. Čáslavský, J.-M. Létoffé, J.-P. Scharff, and P. Miele, “Synthesis, characterization and optical properties of  $\pi$ -conjugated systems incorporating closo-dodecaborate clusters: new potential candidates for two-photon absorption processes,” *Dalton Transactions*, 3065 (2005).
- [127] C. E. Housecroft, “Borane and Carbaborane Clusters Meet Coordination Polymers and Networks: In the Hole or in the Backbone?,” in *50th Anniversary of Electron Counting Paradigms for Polyhedral Molecules* (2021).
- [128] J. Yan, W. Yang, Q. Zhang, and Y. Yan, “Introducing borane clusters into polymeric frameworks: architecture, synthesis, and applications,” *Chemical Communications* **56**, 11720–11734 (2020).
- [129] A. Ferrer-Ugalde, A. González-Campo, C. Viñas, J. Rodríguez-Romero, R. Santillan, N. Farfán, R. Sillanpää, A. Sousa-Pedrares, R. Núñez, et al., “Fluorescence of new o-carborane compounds with different fluorophores: Can it be tuned?,” *Chemistry - A European Journal* **20**, 9940–9951 (2014).
- [130] S. Mukherjee and P. Thilagar, “Boron clusters in luminescent materials,” *Chemical Communications* **52**, 1070–1093 (2016).
- [131] G. F. Jin, Y. J. Cho, K. R. Wee, S. A. Hong, I. H. Suh, H. J. Son, J. D. Lee, W. S. Han, D. W. Cho, et al., “BODIPY functionalized o-carborane dyads for low-energy photosensitization,” *Dalton Transactions* **44**, 2780–2787 (2015).
- [132] M. Chaari, Z. Kelemen, D. Choquesillo-Lazarte, N. Gaztelumendi, F. Teixidor, C. Viñas, C. Nogués, and R. Núñez, “Efficient blue light emitting materials based on *m*-carborane–anthracene dyads. Structure, photophysics and bioimaging studies,” *Biomaterials Science* **7**, 5324–5337 (2019).
- [133] M. Chaari, Z. Kelemen, J. G. Planas, F. Teixidor, D. Choquesillo-Lazarte, A. ben Salah, C. Viñas, and R. Núñez, “Photoluminescence in *m*-carborane–anthracene triads: a combined experimental and computational study,” *Journal of Materials Chemistry C* **6**, 11336–11347 (2018).
- [134] M. Chaari, Z. Kelemen, D. Choquesillo-Lazarte, F. Teixidor, C. Viñas, and R. Núñez, “Anthracene–styrene-substituted *m*-carborane derivatives: insights into the electronic and structural effects of substituents on photoluminescence,” *Inorganic Chemistry Frontiers* **7**, 2370–2380 (2020).
- [135] M. Gon, K. Tanaka, and Y. Chujo, “Concept of Excitation-Driven Boron Complexes and Their Applications for Functional Luminescent Materials,” *Bull Chem Soc Jpn* **92**, 7–18 (2019).
- [136] D. K. You, J. H. Lee, B. H. Choi, H. Hwang, M. H. Lee, K. M. Lee, and M. H. Park, “Effects of Multi-Carborane Substitution on the Photophysical and Electron-Accepting Properties of o-Carboranylbenzene Compounds,” *European Journal of Inorganic Chemistry* **2017**, 2496–2503 (2017).
- [137] A. Ferrer-Ugalde, J. Cabrera-González, E. J. Juárez-Pérez, F. Teixidor, E. Pérez-Inestrosa, J. M. Montenegro, R. Sillanpää, M. Haukka, and R. Núñez, “Carborane–stilbene dyads: the influence of substituents and cluster isomers on photoluminescence properties,” *Dalton Transactions* **46**, 2091–2104 (2017).

- [138] M. Tominaga, H. Naito, Y. Morisaki, and Y. Chujo, "Control of the Emission Behaviors of Trifunctional *o*-Carborane Dyes," *Asian Journal of Organic Chemistry* **3**, 624–631 (2014).
- [139] A. González-Campo, A. Ferrer-Ugalde, C. Viñas, F. Teixidor, R. Sillanpää, J. Rodríguez-Romero, R. Santillan, N. Farfán, and R. Núñez, "A versatile methodology for the controlled synthesis of photoluminescent high-boron-content dendrimers," *Chemistry - A European Journal* **19**, 6299–6312 (2013).
- [140] K. Kokado and Y. Chujo, "Multicolor tuning of aggregation-induced emission through substituent variation of diphenyl-*o*-carborane," *Journal of Organic Chemistry* **76**, 316–319 (2011).
- [141] K. Kokado and Y. Chujo, "Emission via aggregation of alternating polymers with *o*-carborane and *p*-phenylene-ethynylene sequences," *Macromolecules* **42**, 1418–1420 (2009).
- [142] S. Y. Kim, Y. J. Cho, H. J. Son, D. W. Cho, and S. O. Kang, "Photoinduced Electron Transfer in a BODIPY- *ortho* -Carborane Dyad Investigated by Time-Resolved Transient Absorption Spectroscopy," *Journal of Physical Chemistry A* **122**, 3391–3397 (2018).
- [143] A. v. Marsh, M. J. Dyson, N. J. Cheetham, M. Bidwell, M. Little, A. J. P. White, C. N. Warriner, A. C. Swain, I. McCulloch, et al., "Correlating the Structural and Photophysical Properties of *Ortho*, *Meta*, and *Para*-Carboranyl–Anthracene Dyads," *Advanced Electronic Materials* **6** (2020).
- [144] A. M. Spokoyny, M. G. Reuter, C. L. Stern, M. A. Ratner, T. Seideman, and C. A. Mirkin, "Carborane-Based Pincers: Synthesis and Structure of SeBSe and SBS Pd(II) Complexes," *Journal of American Chemical Society* **131**, 9482–9483 (2009).
- [145] A. Ferrer-Ugalde, E. J. Juárez-Pérez, F. Teixidor, C. Viñas, R. Sillanpää, E. Pérez-Inestrosa, and R. Núñez, "Synthesis and characterization of new fluorescent styrene-containing carborane derivatives: The singular quenching role of a phenyl substituent," *Chemistry - A European Journal* **18**, 544–553 (2012).
- [146] Z. Wang, T. Wang, C. Zhang, and M. G. Humphrey, "N-Donor/Fluorenyl *o*-Carborane Fluorophores with Strong Crystallization-Induced Emission," *ChemPhotoChem* **2**, 369–379 (Wiley-VCH Verlag, 2018).
- [147] J. Ochi, K. Tanaka, and Y. Chujo, "Recent Progress in the Development of Solid-State Luminescent *o* -Carboranes with Stimuli Responsivity ," *Angewandte Chemie* **132**, 9925–9939 (2020).
- [148] J. Ochi, K. Tanaka, and Y. Chujo, "Experimental proof for emission annihilation through bond elongation at the carbon-carbon bond in: *O* -carborane with fused biphenyl-substituted compounds," *Dalton Transactions* **50**, 1025–1033 (2021).
- [149] Y. Duan, Q. Pan, Z. Zhao, Y. Gao, Y. Wu, L. Zhao, Y. Geng, M. Zhang, and Z. Su, "Theoretical Simulations of Thermochromic and Aggregation-Induced Emission Behaviors of a Series of Red-Light Anthracene- *o*-carborane Derivatives," *Chemistry – A European Journal* **27**, 9571–9579 (2021).
- [150] M. Born and R. Oppenheimer, "Zur Quantentheorie der Molekeln," *Ann Phys* **389**, 457–484 (1927).
- [151] A. Szabo and N. S. Ostlund, *Modern Quantum Chemistry: Introduction to Advanced Electronic Structure Theory*, Dover edition (1996).

- [152] C. C. J. Roothaan, “New Developments in Molecular Orbital Theory,” *Reviews of Modern Physics* **23**, 69–89 (1951).
- [153] N. H. March, “The Thomas-Fermi approximation in quantum mechanics,” *Advances in Physics* **6**, 1–101 (1957).
- [154] E. Fermi, “Eine statistische Methode zur Bestimmung einiger Eigenschaften des Atoms und ihre Anwendung auf die Theorie des periodischen Systems der Elemente,” *Zeitschrift für Physik* **48**, 73–79 (1928).
- [155] L. H. Thomas, “The calculation of atomic fields,” *Mathematical Proceedings of the Cambridge Philosophical Society* **23**, 542–548 (1927).
- [156] P. Hohenberg and W. Kohn, “Inhomogeneous Electron Gas,” *Physical Review* **136**, B864–B871 (1964).
- [157] W. Kohn and L. J. Sham, “Self-Consistent Equations Including Exchange and Correlation Effects,” *Physical Review* **140**, A1133–A1138 (1965).
- [158] The Nobel Prize in Chemistry 1998, “NobelPrize.org. Nobel Prize Outreach AB 2022. Wed. 13 Apr 2022. <<https://www.nobelprize.org/prizes/chemistry/1998/summary/>>,” 14 April 2022.
- [159] W. Koch and M. C. Holthausen, *A Chemist’s Guide to Density Functional Theory* (Wiley, 2001).
- [160] E. G. Lewars, *Computational Chemistry: Introduction to the Theory and Applications of Molecular and Quantum Mechanics*, 2nd ed. (Springer, 2011).
- [161] A. D. Becke, “Density-functional exchange-energy approximation with correct asymptotic behavior,” *Physical Review A* **38**, 3098–3100 (1988).
- [162] C. Lee, W. Yang, and R. G. Parr, “Development of the Colle-Salvetti correlation-energy formula into a functional of the electron density,” *Physical Review B* **37**, 785–789 (1988).
- [163] J. P. Perdew, “Density-functional approximation for the correlation energy of the inhomogeneous electron gas,” *Physical Review B* **33**, 8822–8824 (1986).
- [164] J. P. Perdew, “Erratum: Density-functional approximation for the correlation energy of the inhomogeneous electron gas,” *Physical Review B* **34**, 7406–7406 (1986).
- [165] P. Atkins and R. Friedman, *Molecular Quantum Mechanics*, 4th ed. (2005).
- [166] E. Runge and E. K. U. Gross, “Density-Functional Theory for Time-Dependent Systems,” *Physical Review Letters* **52**, 997–1000 (1984).
- [167] C. A. Ullrich, *Time-Dependent Density-Functional Theory* (2011).
- [168] M. E. CASIDA, “Time-Dependent Density Functional Response Theory for Molecules” (1995).
- [169] A. Dreuw and M. Head-Gordon, “Single-Reference ab Initio Methods for the Calculation of Excited States of Large Molecules,” *Chemical Reviews* **105**, 4009–4037 (2005).
- [170] J.-D. Chai and M. Head-Gordon, “Long-range corrected hybrid density functionals with damped atom–atom dispersion corrections,” *Physical Chemistry Chemical Physics* **10**, 6615 (2008).
- [171] T. Yanai, D. P. Tew, and N. C. Handy, “A new hybrid exchange–correlation functional using the Coulomb-attenuating method (CAM-B3LYP),” *Chemical Physics Letters* **393**, 51–57 (2004).
- [172] Y. Zhao and D. G. Truhlar, “The M06 suite of density functionals for main group thermochemistry, thermochemical kinetics, noncovalent interactions,

- excited states, and transition elements: two new functionals and systematic testing of four M06-class functionals and 12 other function,” *Theoretical Chemistry Accounts* **120**, 215–241 (2008).
- [173] Y. Zhao and D. G. Truhlar, “A new local density functional for main-group thermochemistry, transition metal bonding, thermochemical kinetics, and noncovalent interactions,” *The Journal of Chemical Physics* **125**, 194101 (2006).
- [174] M. J. G. Peach, P. Benfield, T. Helgaker, and D. J. Tozer, “Excitation energies in density functional theory: An evaluation and a diagnostic test,” *The Journal of Chemical Physics* **128**, 044118 (2008).
- [175] C. A. Guido, P. Cortona, B. Mennucci, and C. Adamo, “On the Metric of Charge Transfer Molecular Excitations: A Simple Chemical Descriptor,” *Journal of Chemical Theory and Computation* **9**, 3118–3126 (2013).
- [176] S. F. Boys, “Electronic wave functions - I. A general method of calculation for the stationary states of any molecular system,” *Proceedings of the Royal Society of London. Series A. Mathematical and Physical Sciences* **200**, 542–554 (1950).
- [177] M. M. Francl, W. J. Pietro, W. J. Hehre, J. S. Binkley, M. S. Gordon, D. J. DeFrees, and J. A. Pople, “Self-consistent molecular orbital methods. XXIII. A polarization-type basis set for second-row elements,” *The Journal of Chemical Physics* **77**, 3654–3665 (1982).
- [178] M. J. Frisch, J. A. Pople, and J. S. Binkley, “Self-consistent molecular orbital methods 25. Supplementary functions for Gaussian basis sets,” *The Journal of Chemical Physics* **80**, 3265–3269 (1984).
- [179] R. Krishnan, J. S. Binkley, R. Seeger, and J. A. Pople, “Self-consistent molecular orbital methods. XX. A basis set for correlated wave functions,” *The Journal of Chemical Physics* **72**, 650–654 (1980).
- [180] W. J. Hehre, L. Radom, P. von R. Schleyer, and J. Pople, *Ab INITIO Molecular Orbital Theory* (1986).
- [181] B. Mennucci, “Polarizable continuum model,” *WIREs Computational Molecular Science* **2**, 386–404 (2012).
- [182] J. Tomasi, B. Mennucci, and R. Cammi, “Quantum Mechanical Continuum Solvation Models,” *Chemical Reviews* **105**, 2999–3094 (2005).
- [183] E. Cancès and B. Mennucci, “Comment on ‘Reaction field treatment of charge penetration’ [J. Chem. Phys. 112, 5558 (2000)],” *The Journal of Chemical Physics* **114**, 4744 (2001).
- [184] J. L. Pascual-Ahuir, E. Silla, J. Tomasi, and R. Bonaccorsi, “Electrostatic interaction of a solute with a continuum. Improved description of the cavity and of the surface cavity bound charge distribution,” *Journal of Computational Chemistry* **8**, 778–787 (1987).
- [185] S. Miertuš, E. Scrocco, and J. Tomasi, “Electrostatic interaction of a solute with a continuum. A direct utilization of AB initio molecular potentials for the prevision of solvent effects,” *Chemical Physics* **55**, 117–129 (1981).
- [186] L. Cheng, “B 14 : An all-boron fullerene,” *The Journal of Chemical Physics* **136**, 104301 (2012).
- [187] Y. F. Shen, C. Xu, and L. J. Cheng, “Deciphering chemical bonding in B<sub>n</sub>H<sub>n</sub>2- (n = 2-17): Flexible multicenter bonding,” *RSC Advances* **7**, 36755–36764 (2017).
- [188] R. E. Williams, “The polyborane, carborane, carbocation continuum: architectural patterns,” *Chemical Reviews* **92**, 177–207 (1992).

- [189] D. Byun, S. Lee, S.-D. Hwang, Y.-F. Hu, G. M. Bancroft, J. A. Glass, J. Zhang, J. T. Spencer, J. Ma, et al., "Photoemission from gaseous and condensed molecular carborane cluster molecules," *Journal of Electron Spectroscopy and Related Phenomena* **69**, 111–116 (1994).
- [190] H. Fang and P. Jena, "Stable Tetra- and Penta-Anions in the Gas Phase," *Angewandte Chemie* **131**, 11370–11374 (2019).
- [191] M. Joshi and T. K. Ghanty, "Lanthanide and actinide doped B<sub>12</sub>H<sub>12</sub><sup>2-</sup> and Al<sub>12</sub>H<sub>12</sub><sup>2-</sup> clusters: new magnetic superatoms with f-block elements," *Physical Chemistry Chemical Physics* **21**, 23720–23732 (2019).
- [192] S. Lee, P. A. Dowben, A. T. Wen, A. P. Hitchcock, J. A. Glass, and J. T. Spencer, "Structures of selected boranes and carboranes," *Journal of Vacuum Science & Technology A: Vacuum, Surfaces, and Films* **10**, 881–885 (1992).
- [193] B. Pathak, D. Samanta, R. Ahuja, and P. Jena, "Borane derivatives: A new class of super- and hyperhalogens," *ChemPhysChem* **12**, 2423–2428 (2011).
- [194] R. Zahradník, V. Balaji, and J. Michl, "An SCF study of 10-vertex and 12-vertex boranes and heteroboranes," *Journal of Computational Chemistry* **12**, 1147–1156 (1991).
- [195] S. Giri, S. Behera, and P. Jena, "Superhalogens as Building Blocks of Halogen-Free Electrolytes in Lithium-Ion Batteries," *Angewandte Chemie International Edition* **53**, 13916–13919 (2014).
- [196] O. Tutusaus, R. Mohtadi, T. S. Arthur, F. Mizuno, E. G. Nelson, and Y. v. Sevryugina, "An Efficient Halogen-Free Electrolyte for Use in Rechargeable Magnesium Batteries," *Angewandte Chemie International Edition* **54**, 7900–7904 (2015).
- [197] M. Zhong, J. Zhou, H. Fang, and P. Jena, "Role of ligands in the stability of B<sub>n</sub>X<sub>n</sub> and CB<sub>n-1</sub>X<sub>n</sub> (n = 5–10; X = H, F, CN) and their potential as building blocks of electrolytes in lithium ion batteries," *Physical Chemistry Chemical Physics* **19**, 17937–17943 (2017).
- [198] G. Chen, T. Zhao, Q. Wang, and P. Jena, "Rational design of stable dianions and the concept of super-chalcogens," *Journal of Physical Chemistry A* **123**, 5753–5761 (2019).
- [199] J. Zhang and Z. Xie, "Synthesis, Structure, and Reactivity of 13- and 14-Vertex Carboranes," *Accounts of Chemical Research* **47**, 1623–1633 (2014).
- [200] L. Deng, H.-S. Chan, and Z. Xie, "Synthesis, Structure, and Reactivity of 13-Vertex Carboranes and 14-Vertex Metallocarboranes," *Journal of American Chemical Society* **128**, 5219–5230 (2006).
- [201] F. Zheng, T. H. Yui, J. Zhang, and Z. Xie, "Synthesis and X-ray characterization of 15- and 16-vertex closo-carboranes," *Nature Communications* **11**, 5943 (2020).
- [202] L. Deng and Z. Xie, "A Journey from 12-Vertex to 14-Vertex Carboranes and to 15-Vertex Metallocarboranes," *Organometallics* **26**, 1832–1845 (2007).
- [203] A. Dreuw, N. Zint, and L. S. Cederbaum, "Dianionic tetraborates do exist as stable entities," *Journal of American Chemical Society* **124**, 10903–10910 (2002).
- [204] N. Zint, A. Dreuw, and L. S. Cederbaum, "Gas-phase stability of derivatives of the closo-hexaborate dianion B<sub>6</sub>H<sub>6</sub><sup>2-</sup>," *Journal of American Chemical Society* **124**, 4910–4917 (2002).



- [205] L. A. Boyd, W. Clegg, R. C. B. Copley, M. G. Davidson, M. A. Fox, T. G. Hibbert, J. A. K. Howard, A. Mackinnon, R. J. Peace, et al., “Exo- $\pi$ -bonding to an ortho-carborane hypercarbon atom: Systematic icosahedral cage distortions reflected in the structures of the fluoro-, hydroxy- and amino-carboranes, 1-X-2-Ph-1,2-C<sub>2</sub>B<sub>10</sub>H<sub>10</sub> (X = F, OH or NH<sub>2</sub>) and related anions,” *Dalton Transactions*, 2786–2799 (2004).
- [206] J. Moon, H. Baek, and J. Kim, “Unusually high stability of B<sub>12</sub>(BO)<sub>12</sub>–achieved by boronyl ligand manipulation: Theoretical investigation,” *Chemical Physics Letters* **698**, 72–76 (2018).
- [207] R. T. Boeré, J. Derendorf, C. Jenne, S. Kacprzak, M. Keßler, R. Riebau, S. Riedel, T. L. Roemmele, M. Rühle, et al., “On the oxidation of the three-dimensional aromatics [B<sub>12</sub>X<sub>12</sub>]<sup>2-</sup> (X=F, Cl, Br, I),” *Chemistry - A European Journal* **20**, 4447–4459 (2014).
- [208] T. B. Lee and M. L. McKee, “Redox Energetics of Hypercloso Boron Hydrides B<sub>n</sub>H<sub>n</sub> (n = 6–13) and B<sub>12</sub>X<sub>12</sub> (X = F, Cl, OH, and CH<sub>3</sub>),” *Inorganic Chemistry* **51**, 4205–4214 (2012).
- [209] F. Teixidor and C. Viñas, “Halogenated Icosahedral Carboranes: A Platform for Remarkable Applications,” in *Handbook of Boron Science With Applications in Organometallics, Catalysis, Materials and Medicine* **1** (2018).
- [210] A. Avelar, F. S. Tham, and C. A. Reed, “Superacidity of Boron Acids H<sub>2</sub>(B<sub>12</sub>X<sub>12</sub>) (X=Cl, Br),” *Angewandte Chemie International Edition* **48**, 3491–3493 (2009).
- [211] M. J. Frisch, G. W. Trucks, H. B. Schlegel, G. E. Scuseria, M. A. Robb, J. R. Cheeseman, G. Scalmani, V. Barone, G. A. Petersson, et al., “Gaussian 09,” Gaussian 09 (Gaussian, Inc., Wallingford CT, 2016, 2010).
- [212] R. D. Dennington, T. A. Keith, and J. M. Millam, “GaussView,” GaussView 5 (Semichem, Inc., Wallingford CT, 2009, 2000).
- [213] J. P. Perdew, M. Ernzerhof, and K. Burke, “Rationale for mixing exact exchange with density functional approximations,” *The Journal of Chemical Physics* **105**, 9982–9985 (1996).
- [214] C. Adamo and V. Barone, “Toward reliable density functional methods without adjustable parameters: The PBE0 model,” *The Journal of Chemical Physics* **110**, 6158–6170 (1999).
- [215] J. P. Perdew, “Density-functional approximation for the correlation energy of the inhomogeneous electron gas,” *Physical Review B* **33**, 8822–8824 (1986).
- [216] A. D. Becke, “Density-functional exchange-energy approximation with correct asymptotic behavior,” *Physical Review A* **38**, 3098–3100 (1988).
- [217] A. D. Becke, “Density-functional thermochemistry. III. The role of exact exchange,” *The Journal of Chemical Physics* **98**, 5648–5652 (1993).
- [218] C. M. Breneman and K. B. Wiberg, “Determining atom-centered monopoles from molecular electrostatic potentials. The need for high sampling density in formamide conformational analysis,” *Journal of Computational Chemistry* **11**, 361–373 (1990).
- [219] J. P. Foster and F. Weinhold, “Natural hybrid orbitals,” *Journal of American Chemical Society* **102**, 7211–7218 (1980).
- [220] A. E. Reed and F. Weinhold, “Natural bond orbital analysis of near-Hartree–Fock water dimer,” *The Journal of Chemical Physics* **78**, 4066–4073 (1983).

- [221] A. E. Reed and F. Weinhold, "Natural localized molecular orbitals," *The Journal of Chemical Physics* **83**, 1736–1740 (1985).
- [222] A. E. Reed, R. B. Weinstock, and F. Weinhold, "Natural population analysis," *The Journal of Chemical Physics* **83**, 735–746 (1985).
- [223] J. Zhang, Z. Lin, and Z. Xie, "DFT Studies on Structures, Stabilities, and Electron Affinities of closo-Supercarboranes C<sub>2</sub>B<sub>(n-2)</sub>H<sub>n</sub> (n = 13–20)," *Organometallics* **34**, 5576–5588 (2015).
- [224] R. Liao, Y. Zhu, Q. Li, and R. Sa, "A topological pattern for understanding the structures of boranes and borane analog compounds," *Structural Chemistry* **26**, 353–364 (2015).
- [225] T. M. Krygowski and B. T. Stępień, "Sigma- and Pi-Electron Delocalization: Focus on Substituent Effects," *Chemical Reviews* **105**, 3482–3512 (2005).
- [226] T. M. Krygowski, H. Szatyłowicz, O. A. Stasyuk, J. Dominikowska, and M. Palusiak, "Aromaticity from the Viewpoint of Molecular Geometry: Application to Planar Systems," *Chemical Reviews* **114**, 6383–6422 (2014).
- [227] B. Milián Medina, D. Beljonne, H.-J. Egelhaaf, and J. Gierschner, "Effect of fluorination on the electronic structure and optical excitations of  $\pi$ -conjugated molecules," *The Journal of Chemical Physics* **126**, 111101 (2007).
- [228] J. Fanfrlík, M. Lepšík, D. Horinek, Z. Havlas, and P. Hobza, "Interaction of carboranes with biomolecules: Formation of dihydrogen bonds," *ChemPhysChem* **7**, 1100–1105 (2006).
- [229] W. T. Klooster, T. F. Koetzle, P. E. M. Siegbahn, T. B. Richardson, and R. H. Crabtree, "Study of the N–H···H–B Dihydrogen Bond Including the Crystal Structure of BH<sub>3</sub>NH<sub>3</sub> by Neutron Diffraction," *Journal of American Chemical Society* **121**, 6337–6343 (1999).
- [230] J. Li, F. Zhao, and F. Jing, "B–H[ $\delta^-$ ] $\sigma$  bond as dihydrogen bond acceptor: Some theoretical observations and predictions," *The Journal of Chemical Physics* **116**, 25 (2002).
- [231] K. A. Lyssenko and M. Yu. Antipin, "Nature of weak inter- and intramolecular interactions in crystals. 1. The F...O and F...H contacts in the crystal of 2-trifluoroacetyl-5-trifluoromethylpyrrole," *Russian Chemical Bulletin* **53**, 10–17 (2004).
- [232] J. G. Planas, C. Viñas, F. Teixidor, A. Comas-Vives, G. Ujaque, A. Lledós, M. E. Light, and M. B. Hursthouse, "Self-Assembly of Mercaptane–Metallacarborane Complexes by an Unconventional Cooperative Effect: A C–H···S–H···H–B Hydrogen/Dihydrogen Bond Interaction," *Journal of American Chemical Society* **127**, 15976–15982 (2005).
- [233] E. S. Shubina, N. v. Belkova, E. v. Bakhmutova, L. N. Saitkulova, A. v. Ionidis, and L. M. Epstein, "Problems of unusual hydrogen bonds between proton donors and transition metal hydrides and borohydrides," *Russian Chemical Bulletin* **47**, 817–822 (1998).
- [234] J. Mei, N. L. C. Leung, R. T. K. Kwok, J. W. Y. Lam, and B. Z. Tang, "Aggregation-Induced Emission: Together We Shine, United We Soar!," *Chemical Reviews* **115**, 11718–11940 (2015).
- [235] O. Ostroverkhova, "Organic Optoelectronic Materials: Mechanisms and Applications," *Chemical Reviews* **116**, 13279–13412 (2016).

- [236] Z. Lin, R. Kabe, K. Wang, and C. Adachi, "Influence of energy gap between charge-transfer and locally excited states on organic long persistence luminescence," *Nature Communications* **11**, 191 (2020).
- [237] D. Cao, Z. Liu, P. Verwilt, S. Koo, P. Jangjili, J. S. Kim, and W. Lin, "Coumarin-Based Small-Molecule Fluorescent Chemosensors," *Chemical Reviews* **119**, 10403–10519 (2019).
- [238] Y. Q. Dong, J. W. Y. Lam, and B. Z. Tang, "Mechanochromic Luminescence of Aggregation-Induced Emission Luminogens," *The Journal of Physical Chemistry Letters* **6**, 3429–3436 (2015).
- [239] S. Sasaki, G. P. C. Drummen, and G. Konishi, "Recent advances in twisted intramolecular charge transfer (TICT) fluorescence and related phenomena in materials chemistry," *Journal of Materials Chemistry C* **4**, 2731–2743 (2016).
- [240] H. Usta, D. Alimli, R. Ozdemir, S. Dabak, Y. Zorlu, F. Alkan, E. Tekin, and A. Can, "Highly Efficient Deep-Blue Electroluminescence Based on a Solution-Processable A- $\pi$ -D- $\pi$ -A Oligo(*p*-phenyleneethynylene) Small Molecule," *ACS Applied Materials & Interfaces* **11**, 44474–44486 (2019).
- [241] A. T. Phillips, Z. Yu, D. J. Stewart, T. M. Cooper, J. E. Haley, L.-S. Tan, and T. A. Grusenmeyer, "Influence of Structural Isomerism on the Photophysical Properties of a Series of Donor-Acceptor 1-Naphthalenecarbonitrile Derivatives Possessing Amine Substituents," *The Journal of Physical Chemistry A* **124**, 2113–2122 (2020).
- [242] A. J. Welch, "The significance and impact of Wade's rules," *Chemical Communications* **49**, 3615–3616 (2013).
- [243] H. Naito, K. Nishino, Y. Morisaki, K. Tanaka, and Y. Chujo, "Solid-State Emission of the Anthracene-*o*-Carborane Dyad from the Twisted-Intramolecular Charge Transfer in the Crystalline State," *Angewandte Chemie International Edition* **56**, 254–259 (2017).
- [244] H. Naito, Y. Morisaki, and Y. Chujo, "*o*-Carborane-Based Anthracene: A Variety of Emission Behaviors," *Angewandte Chemie International Edition* **54**, 5084–5087 (2015).
- [245] K. L. Martin, A. Krishnamurthy, J. Strahan, E. R. Young, and K. R. Carter, "Excited State Characterization of Carborane-Containing Poly(dihexyl fluorene)s," *The Journal of Physical Chemistry A* **123**, 1701–1709 (2019).
- [246] L. Weber, J. Kahlert, R. Brockhinke, L. Böhling, A. Brockhinke, H. G. Stammeler, B. Neumann, R. A. Harder, and M. A. Fox, "Luminescence properties of C-diazaborolyl-ortho-carboranes as donor-acceptor systems," *Chemistry - A European Journal* **18**, 8347–8357 (2012).
- [247] K. Nishino, H. Yamamoto, K. Tanaka, and Y. Chujo, "Development of Solid-State Emissive Materials Based on Multifunctional *o*-Carborane-Pyrene Dyads," *Organic Letters* **18**, 4064–4067 (2016).
- [248] K. Tanaka, K. Nishino, S. Ito, H. Yamane, K. Suenaga, K. Hashimoto, and Y. Chujo, "Development of solid-state emissive *o*-carboranes and theoretical investigation of the mechanism of the aggregation-induced emission behaviors of organoboron 'element-blocks,'" *Faraday Discussions* **196**, 31–42 (Royal Society of Chemistry, 2017).
- [249] R. Furue, T. Nishimoto, I. S. Park, J. Lee, and T. Yasuda, "Aggregation-Induced Delayed Fluorescence Based on Donor/Acceptor-Tethered Janus Carborane Triads: Unique Photophysical Properties of Nondoped OLEDs," *Angewandte Chemie International Edition* **55**, 7171–7175 (2016).

- [250] X. Wu, J. Guo, Y. Cao, J. Zhao, W. Jia, Y. Chen, and D. Jia, “Mechanically triggered reversible stepwise tricolor switching and thermochromism of anthracene-*o*-carborane dyad,” *Chemical Science* **9**, 5270–5277 (2018).
- [251] S. Kim, J. H. Lee, H. So, J. Ryu, J. Lee, H. Hwang, Y. Kim, M. H. Park, and K. M. Lee, “Spirobifluorene-Based *o*-Carboranyl Compounds: Insights into the Rotational Effect of Carborane Cages on Photoluminescence,” *Chemistry - A European Journal* **26**, 548–557 (Wiley-VCH Verlag, 2020).
- [252] K. R. Wee, Y. J. Cho, J. K. Song, and S. O. Kang, “Multiple photoluminescence from 1,2-dinaphthyl-ortho-carborane,” *Angewandte Chemie - International Edition* **52**, 9682–9685 (2013).
- [253] A. v. Marsh, N. J. Cheetham, M. Little, M. Dyson, A. J. P. White, P. Beavis, C. N. Warriner, A. C. Swain, P. N. Stavrinou, et al., “Carborane-Induced Excimer Emission of Severely Twisted Bis-*o*-Carboranyl Chrysene,” *Angewandte Chemie - International Edition* **57**, 10640–10645 (2018).
- [254] K. Nishino, H. Yamamoto, K. Tanaka, and Y. Chujo, “Solid-State Thermochromic Luminescence through Twisted Intramolecular Charge Transfer and Excimer Formation of a Carborane–Pyrene Dyad with an Ethynyl Spacer,” *Asian Journal of Organic Chemistry* **6**, 1818–1822 (2017).
- [255] N. M. O’boyle, A. L. Tenderholt, and K. M. Langner, “cclib: A library for package-independent computational chemistry algorithms,” *Journal of Computational Chemistry* **29**, 839–845 (2008).
- [256] T. Lu and F. Chen, “Multiwfn: A multifunctional wavefunction analyzer,” *Journal of Computational Chemistry* **33**, 580–592 (2012).
- [257] S. Kim, J. H. Lee, H. So, M. Kim, M. S. Mun, H. Hwang, M. H. Park, and K. M. Lee, “Insights into the effects of substitution position on the photophysics of mono-*o*-carborane-substituted pyrenes,” *Inorganic Chemistry Frontiers* **7**, 2949–2959 (2020).
- [258] N. Shida, S. Owaki, H. Eguchi, T. Nishikawa, I. Tomita, and S. Inagi, “Bis(pentafluorophenyl)-*o*-carborane and its arylthio derivatives: Synthesis, electrochemistry and optical properties,” *Dalton Transactions* **49**, 12985–12989 (2020).
- [259] J. Li, C. Yang, X. Peng, Y. Chen, Q. Qi, X. Luo, W.-Y. Lai, and W. Huang, “Stimuli-responsive solid-state emission from *o*-carborane–tetraphenylethene dyads induced by twisted intramolecular charge transfer in the crystalline state,” *Journal of Materials Chemistry C* **6**, 19–28 (2018).
- [260] J. Plötner, D. J. Tozer, and A. Dreuw, “Dependence of Excited State Potential Energy Surfaces on the Spatial Overlap of the Kohn–Sham Orbitals and the Amount of Nonlocal Hartree–Fock Exchange in Time-Dependent Density Functional Theory,” *Journal of Chemical Theory and Computation* **6**, 2315–2324 (2010).
- [261] R. Li, J. Zheng, and D. G. Truhlar, “Density functional approximations for charge transfer excitations with intermediate spatial overlap,” *Physical Chemistry Chemical Physics* **12**, 12697 (2010).
- [262] P.-F. Loos, M. Comin, X. Blase, and D. Jacquemin, “Reference Energies for Intramolecular Charge-Transfer Excitations,” *Journal of Chemical Theory and Computation* **17**, 3666–3686 (2021).
- [263] A. D. Laurent and D. Jacquemin, “TD-DFT benchmarks: A review,” *International Journal of Quantum Chemistry* **113**, 2019–2039 (2013).
- [264] M. Walker, A. J. A. Harvey, A. Sen, and C. E. H. Dessent, “Performance of M06, M06-2X, and M06-HF Density Functionals for Conformationally

- Flexible Anionic Clusters: M06 Functionals Perform Better than B3LYP for a Model System with Dispersion and Ionic Hydrogen-Bonding Interactions,” *The Journal of Physical Chemistry A* **117**, 12590–12600 (2013).
- [265] N. Mandal, A. K. Pal, P. Gain, A. Zohaib, and A. Datta, “Transition-State-like Planar Structures for Amine Inversion with Ultralong C–C Bonds in Diamino- *o* -carborane and Diamino- *o* -dodecahedron,” *Journal of American Chemical Society* **142**, 5331–5337 (2020).
- [266] D. Tahaoğlu, F. Alkan, and M. Durandurdu, “Theoretical investigation of substituent effects on the relative stabilities and electronic structure of  $[\text{B}_n\text{X}_n]^{2-}$  clusters,” *Journal of Molecular Modeling* **27**, 365 (2021).



# APPENDIX

## Appendix A. Optimized geometries of $[\text{B}_n\text{H}_n]^{2-}$ clusters (PBE0/6-311++G\*\*)

### $[\text{B}_{10}\text{H}_{10}]^{2-}$

B	0.0000000	1.2968840	0.7596370
B	0.9170350	0.9170350	-0.7596370
B	-0.9170350	-0.9170350	-0.7596370
B	0.9170350	-0.9170350	-0.7596370
B	1.2968840	0.0000000	0.7596370
B	0.0000000	-1.2968840	0.7596370
B	-0.9170350	0.9170350	-0.7596370
B	0.0000000	0.0000000	-1.8631770
B	0.0000000	0.0000000	1.8631770
B	-1.2968840	0.0000000	0.7596370
H	2.4370520	0.0000000	1.1622720
H	0.0000000	0.0000000	3.0675480
H	0.0000000	2.4370520	1.1622720
H	1.7232560	1.7232560	-1.1622720
H	-1.7232560	1.7232560	-1.1622720
H	-2.4370520	0.0000000	1.1622720
H	0.0000000	0.0000000	-3.0675480
H	1.7232560	-1.7232560	-1.1622720
H	0.0000000	-2.4370520	1.1622720
H	-1.7232560	-1.7232560	-1.1622720

### $[\text{B}_{12}\text{H}_{12}]^{2-}$

B	0.00065300	0.00274100	-1.69510100
B	-0.00065300	-0.00274000	1.69510400
B	0.23769000	1.49867000	-0.75556000
B	-1.35050500	0.68974000	-0.75747900
B	-1.07194300	-1.07069300	-0.76021800
B	0.68841100	-1.34977100	-0.75999200
B	1.49780800	0.23818200	-0.75711300
B	1.07194500	1.07069400	0.76021800
B	1.35050600	-0.68974000	0.75747900
B	-0.23768900	-1.49867100	0.75556000
B	-1.49780900	-0.23818300	0.75711200

B	-0.68841200	1.34977200	0.75999200
H	0.00111700	0.00469100	-2.90092700
H	-0.00111700	-0.00469000	2.90092900
H	0.40677200	2.56476100	-1.29303400
H	-2.31119700	1.18039200	-1.29631900
H	-1.83447900	-1.83234000	-1.30100700
H	1.17811700	-2.30994100	-1.30061900
H	2.56328600	0.40761500	-1.29569200
H	1.83448100	1.83234000	1.30100500
H	2.31119900	-1.18039200	1.29631800
H	-0.40677000	-2.56476300	1.29303300
H	-2.56328800	-0.40761700	1.29569000
H	-1.17811900	2.30994300	1.30061700

[B<sub>13</sub>H<sub>13</sub>]<sup>2-</sup>

B	0.00000000	0.00000000	2.11419400
B	0.00000000	1.38726000	1.27684500
B	0.00000000	-1.38726000	1.27684500
B	1.34195300	0.00000000	0.84082000
B	-1.34195300	0.00000000	0.84082000
B	0.87723000	1.49846400	-0.26734700
B	0.87723000	-1.49846400	-0.26734700
B	-0.87723000	-1.49846400	-0.26734700
B	-0.87723000	1.49846400	-0.26734700
B	1.42081700	0.00000000	-0.98827800
B	-1.42081700	0.00000000	-0.98827800
B	0.00000000	0.88720300	-1.64801600
B	0.00000000	-0.88720300	-1.64801600
H	0.00000000	2.42066600	1.90800600
H	0.00000000	-2.42066600	1.90800600
H	2.43704800	0.00000000	1.34730700
H	-2.43704800	0.00000000	1.34730700
H	0.00000000	1.47027100	-2.70127600
H	0.00000000	-1.47027100	-2.70127600
H	1.55220400	-2.49272100	-0.34696000
H	1.55220400	2.49272100	-0.34696000
H	-1.55220400	2.49272100	-0.34696000
H	-1.55220400	-2.49272100	-0.34696000
H	-2.49210000	0.00000000	-1.53822400
H	2.49210000	0.00000000	-1.53822400
H	0.00000000	0.00000000	3.31846600

$[B_{14}H_{14}]^{2-}$ 

B	0.00000000	1.74109500	0.75647100
B	-1.74109500	0.00000000	-0.75647100
B	-1.50752100	0.87073600	0.75761300
B	0.00000000	-1.74109500	0.75647100
B	1.50752100	-0.87073600	0.75761300
B	1.50752100	0.87073600	0.75761300
B	-0.87073600	1.50752100	-0.75761300
B	1.74109500	0.00000000	-0.75647100
B	-1.50752100	-0.87073600	0.75761300
B	-0.87073600	-1.50752100	-0.75761300
B	0.87073600	1.50752100	-0.75761300
B	0.00000000	0.00000000	1.56258600
B	0.00000000	0.00000000	-1.56258600
B	0.87073600	-1.50752100	-0.75761300
H	1.39304500	2.41234900	-1.35592600
H	-1.39304500	2.41234900	-1.35592600
H	0.00000000	0.00000000	-2.76600200
H	-2.78623400	0.00000000	-1.35425700
H	-2.41234900	1.39304500	1.35592600
H	-2.41234900	-1.39304500	1.35592600
H	-1.39304500	-2.41234900	-1.35592600
H	1.39304500	-2.41234900	-1.35592600
H	0.00000000	-2.78623400	1.35425700
H	0.00000000	0.00000000	2.76600200
H	0.00000000	2.78623400	1.35425700
H	2.41234900	1.39304500	1.35592600
H	2.78623400	0.00000000	-1.35425700
H	2.41234900	-1.39304500	1.35592600

 $[B_{15}H_{15}]^{2-}$ 

B	-0.85852200	-0.49566800	1.82187100
B	0.00000000	0.99133500	1.82187100
H	0.00000000	1.76333900	2.74210400
B	0.85852200	-0.49566800	1.82187100
H	1.52709700	-0.88167000	2.74210400
B	-1.45742400	0.84144400	0.84309900
B	1.45742400	0.84144400	0.84309900
H	2.43251400	1.40441200	1.26598000
B	0.00000000	-1.68288900	0.84309900
H	0.00000000	-2.80882500	1.26598000



B	0.00000000	1.68659700	0.00000000
B	1.46063600	-0.84329900	0.00000000
H	2.50196600	-1.44451100	0.00000000
B	-1.46063600	-0.84329900	0.00000000
H	-2.50196600	-1.44451100	0.00000000
B	1.45742400	0.84144400	-0.84309900
H	2.43251400	1.40441200	-1.26598000
B	0.00000000	-1.68288900	-0.84309900
H	0.00000000	-2.80882500	-1.26598000
B	-1.45742400	0.84144400	-0.84309900
H	-2.43251400	1.40441200	-1.26598000
B	0.85852200	-0.49566800	-1.82187100
H	1.52709700	-0.88167000	-2.74210400
B	-0.85852200	-0.49566800	-1.82187100
H	-1.52709700	-0.88167000	-2.74210400
B	0.00000000	0.99133500	-1.82187100
H	-1.52709700	-0.88167000	2.74210400
H	-2.43251400	1.40441200	1.26598000
H	0.00000000	2.88902200	0.00000000
H	0.00000000	1.76333900	-2.74210400

**[B<sub>16</sub>H<sub>16</sub>]<sup>2-</sup>**

B	0.94546300	-0.94546300	1.32665500
B	-1.46175900	1.46175900	-0.35659100
B	0.00000000	-1.33708700	-1.32665500
B	1.33708700	0.00000000	-1.32665500
B	-1.33708700	0.00000000	-1.32665500
B	-0.94546300	-0.94546300	1.32665500
B	0.00000000	2.06723900	0.35659100
B	-2.06723900	0.00000000	0.35659100
B	0.94546300	0.94546300	1.32665500
B	-0.94546300	0.94546300	1.32665500
B	1.46175900	1.46175900	-0.35659100
B	2.06723900	0.00000000	0.35659100
B	1.46175900	-1.46175900	-0.35659100
B	0.00000000	-2.06723900	0.35659100
B	-1.46175900	-1.46175900	-0.35659100
B	0.00000000	1.33708700	-1.32665500
H	-1.41338200	1.41338200	2.33032000
H	0.00000000	3.22793600	0.66707200
H	1.41338200	1.41338200	2.33032000
H	3.22793600	0.00000000	0.66707200
H	2.28249500	-2.28249500	-0.66707200

H	0.00000000	-3.22793600	0.66707200
H	1.41338200	-1.41338200	2.33032000
H	-1.41338200	-1.41338200	2.33032000
H	-2.28249500	-2.28249500	-0.66707200
H	-3.22793600	0.00000000	0.66707200
H	-2.28249500	2.28249500	-0.66707200
H	0.00000000	1.99882400	-2.33032000
H	1.99882400	0.00000000	-2.33032000
H	2.28249500	2.28249500	-0.66707200
H	-1.99882400	0.00000000	-2.33032000
H	0.00000000	-1.99882400	-2.33032000

## Appendix B. Optimized geometries of *o*-CB-Ant and *o*-CB-Pent S1 state conformers

### *o*-CB-Ant \_ LE conformer

C	-1.798418	1.222064	0.347902
C	-0.991210	-0.110567	-0.197375
B	-3.399350	-1.513682	-0.059919
B	-1.509097	-0.012601	1.472397
B	-3.036144	0.882867	1.451922
B	-3.380128	1.340845	-0.222957
B	-2.090886	0.719388	-1.258840
B	-2.091876	-1.034783	-1.150139
B	-3.621421	-0.139868	-1.160210
B	-4.211606	-0.042654	0.510296
B	-3.042148	-0.876321	1.558630
B	-1.737526	-1.488216	0.531762
H	-1.067684	-2.423009	0.795154
H	-1.664395	-1.634897	-2.074744
H	-1.636274	1.316026	-2.168213
H	-4.330431	-0.167717	-2.110996
H	-3.800038	2.419857	-0.469543
H	-5.369592	0.003352	0.766706
H	-3.219986	1.662746	2.323412
H	-3.337668	-1.442746	2.558686
H	-0.653596	0.146865	2.271751
H	-3.963574	-2.546110	-0.219310
H	-1.195131	2.110674	0.478105
C	0.497254	-0.018202	-0.361199
C	1.294297	-1.229028	-0.314479
C	1.184227	1.261288	-0.324937
C	0.894560	-2.475478	-0.809995

C	2.598147	-1.153804	0.294820
C	2.483217	1.302328	0.304079
C	0.699772	2.468245	-0.848034
C	1.676772	-3.632528	-0.645200
H	-0.037902	-2.566617	-1.349007
C	3.347128	-2.328261	0.482476
C	3.116786	0.099528	0.670586
C	3.122727	2.538497	0.503084
H	-0.206813	2.478824	-1.438289
C	1.374980	3.690098	-0.669934
C	2.891918	-3.565960	0.017702
H	1.310720	-4.576431	-1.034604
H	4.297644	-2.257371	1.004257
H	4.102221	0.145602	1.128398
C	2.572181	3.731089	0.026164
H	4.067703	2.549760	1.038954
H	0.942551	4.596262	-1.080462
H	3.490258	-4.457743	0.171562
H	3.086866	4.671948	0.189511

***o*-CB-Ant \_ HLCT conformer**

C	-1.989700	0.000021	1.618459
C	-0.916923	-0.000022	-0.357448
B	-3.528278	-0.000019	-1.311072
B	-1.783544	-1.279159	0.553564
B	-3.332370	-0.889668	1.421169
B	-3.332402	0.889645	1.421151
B	-1.783598	1.279175	0.553583
B	-1.995261	0.894603	-1.210206
B	-3.386617	1.425494	-0.262642
B	-4.329311	-0.000025	0.245316
B	-3.386589	-1.425522	-0.262641
B	-1.995285	-0.894599	-1.210231
H	-1.573805	-1.557270	-2.097894
H	-1.573769	1.557312	-2.097831
H	-1.156691	2.215133	0.915493
H	-3.884583	2.468916	-0.538490
H	-3.691179	1.583219	2.315549
H	-5.515071	-0.000024	0.331291
H	-3.691097	-1.583244	2.315583
H	-3.884510	-2.468977	-0.538446
H	-1.156556	-2.215070	0.915451

H	-4.131338	0.000032	-2.336147
H	-1.387081	0.000003	2.518905
C	0.536722	-0.000004	-0.349539
C	1.295631	-1.243382	-0.270111
C	1.295623	1.243387	-0.270124
C	0.806293	-2.489374	-0.697826
C	2.625911	-1.219909	0.269662
C	2.625896	1.219918	0.269677
C	0.806294	2.489371	-0.697866
C	1.547940	-3.663734	-0.558518
H	-0.163604	-2.557273	-1.166807
C	3.340740	-2.426837	0.442188
C	3.238741	0.000010	0.589690
C	3.340709	2.426859	0.442221
H	-0.163587	2.557250	-1.166883
C	1.547930	3.663735	-0.558547
C	2.810288	-3.640479	0.034379
H	1.126629	-4.598944	-0.911295
H	4.328752	-2.381411	0.891859
H	4.242206	0.000012	1.007637
C	2.810258	3.640492	0.034396
H	4.328717	2.381439	0.891904
H	1.126633	4.598943	-0.911347
H	3.376065	-4.556868	0.163656
H	3.376014	4.556890	0.163705

***o*-CB-Ant \_ CT conformer**

C	2.720247	1.511976	-0.000042
C	0.852266	-0.198431	0.000253
B	3.069743	-1.862159	0.000196
B	1.992114	0.549913	-1.149807
B	3.852400	0.789625	-0.889717
B	3.852538	0.789765	0.889574
B	1.992312	0.550084	1.150006
B	1.656325	-1.282987	0.906009
B	3.255690	-0.786897	1.409347
B	4.345242	-0.658470	-0.000004
B	3.255460	-0.787120	-1.409155
B	1.656179	-1.283120	-0.905463
H	1.008024	-1.920457	-1.669552
H	1.008299	-1.920233	1.670281
H	1.451725	1.085847	2.064661
H	3.597413	-1.187461	2.476571

H	4.532129	1.453458	1.602904
H	5.481802	-1.012073	-0.000073
H	4.531883	1.453210	-1.603251
H	3.597007	-1.187841	-2.476374
H	1.451340	1.085522	-2.064442
H	3.333970	-3.023554	0.000262
C	-0.595239	-0.033319	0.000233
C	-1.490743	-1.178227	0.000204
C	-1.188216	1.286884	-0.000011
C	-1.060042	-2.525551	0.000402
C	-2.912322	-0.972369	-0.000089
C	-2.611381	1.449831	-0.000289
C	-0.421534	2.469918	-0.000041
C	-1.961963	-3.577488	0.000364
H	-0.012632	-2.773456	0.000613
C	-3.813640	-2.066127	-0.000138
C	-3.436880	0.323731	-0.000325
C	-3.198225	2.740244	-0.000542
H	0.651211	2.412248	0.000165
C	-1.014644	3.721398	-0.000287
C	-3.348486	-3.359618	0.000096
H	-1.578162	-4.592204	0.000553
H	-4.879122	-1.856618	-0.000361
H	-4.516169	0.457389	-0.000567
C	-2.411649	3.868237	-0.000535
H	-4.281433	2.816055	-0.000746
H	-0.381853	4.602618	-0.000287
H	-4.036629	-4.197274	0.000053
H	-2.859156	4.855730	-0.000727
H	2.615044	2.589392	-0.000132

***o*-CB-Pent \_ LE conformer**

C	1.320278	2.311972	0.472970
C	-0.042454	1.556869	-0.069075
B	-1.313391	4.042973	-0.046027
B	0.054786	2.133883	1.582310
B	1.034790	3.608454	1.519351
B	1.536149	3.860821	-0.158704
B	0.859167	2.564502	-1.152792
B	-0.892541	2.666387	-1.074900
B	0.085126	4.143075	-1.130564
B	0.190969	4.794586	0.516530

B	-0.721737	3.715516	1.595132
B	-1.388590	2.407671	0.611664
H	-2.364547	1.810707	0.898370
H	-1.501018	2.234352	-1.992155
H	1.442844	2.045791	-2.035563
H	0.113327	4.814607	-2.108011
H	2.640136	4.210470	-0.404012
H	0.297315	5.957845	0.727696
H	1.809445	3.781767	2.397497
H	-1.286968	4.079558	2.572999
H	0.154096	1.305436	2.418626
H	-2.310390	4.656255	-0.245162
H	2.170535	1.667853	0.650074
C	-0.025752	0.047366	-0.177862
C	-1.272679	-0.674120	-0.135784
C	1.209857	-0.698262	-0.136386
C	-2.496141	-0.190895	-0.591702
C	-1.271757	-2.026227	0.410154
C	1.177220	-2.048019	0.423179
C	2.448614	-0.258504	-0.601204
C	-3.716002	-0.904486	-0.455418
H	-2.552009	0.763153	-1.096549
C	-2.472253	-2.715953	0.582293
C	-0.054832	-2.634789	0.743745
C	2.360254	-2.764149	0.605641
H	2.533629	0.671141	-1.148021
C	3.650523	-1.003306	-0.458877
C	-3.712415	-2.187806	0.169900
H	-2.443643	-3.702366	1.040253
H	-0.065580	-3.637594	1.164095
C	3.614490	-2.275592	0.186312
H	2.304472	-3.746478	1.069805
C	-4.932154	-2.884037	0.329682
C	-6.115601	-2.334445	-0.121307
C	4.814913	-3.004874	0.347828
C	6.009992	-2.499480	-0.122843
C	6.045028	-1.249059	-0.771938
C	4.886103	-0.514600	-0.936151
C	-4.940181	-0.370351	-0.912340
C	-6.119400	-1.072657	-0.748406
H	-7.054258	-0.651155	-1.103380
H	4.779278	-3.971805	0.842499
H	6.926667	-3.066926	0.001685

H	6.987971	-0.862095	-1.144457
H	4.914260	0.451466	-1.433473
H	-4.942708	0.605573	-1.390571
H	-7.047991	-2.875478	0.003673
H	-4.922416	-3.858979	0.809614

***o*-CB-Pent \_ HLCT conformer (full optimization)**

C	0.000209	2.280309	1.460970
C	0.000091	1.562213	-0.093987
B	0.000133	4.154029	-1.143945
B	-1.416441	2.348340	0.556370
B	-0.879535	3.715559	1.540174
B	0.880083	3.715517	1.540178
B	1.416679	2.348097	0.556376
B	0.881067	2.619616	-1.115049
B	1.436863	3.974316	-0.119832
B	0.000289	4.831526	0.487383
B	-1.436500	3.974521	-0.119756
B	-0.880986	2.619696	-1.115036
H	-1.463962	2.147222	-2.028677
H	1.464376	2.147246	-2.028545
H	2.329933	1.696299	0.909652
H	2.473263	4.506376	-0.345896
H	1.495333	3.935449	2.527392
H	0.000396	5.998939	0.702670
H	-1.494627	3.935561	2.527474
H	-2.472863	4.506732	-0.345629
H	-2.329297	1.696304	0.910280
H	0.000390	4.819408	-2.127160
H	-0.000027	1.560305	2.271404
C	-0.000048	0.054869	-0.148142
C	-1.239695	-0.689102	-0.113863
C	1.239566	-0.689206	-0.113957
C	-2.463725	-0.242589	-0.602437
C	-1.223960	-2.032311	0.455719
C	1.223757	-2.032377	0.455692
C	2.463613	-0.242748	-0.602498
C	-3.672940	-0.976005	-0.471774
H	-2.529787	0.699773	-1.128030
C	-2.414574	-2.738721	0.628129
C	-0.000115	-2.623981	0.799060
C	2.414324	-2.738872	0.628094

H	2.529776	0.699677	-1.127981
C	3.672798	-0.976231	-0.471798
C	-3.657693	-2.243073	0.184925
H	-2.374527	-3.715823	1.104927
H	-0.000127	-3.620812	1.233606
C	3.657471	-2.243302	0.184880
H	2.374220	-3.715964	1.104907
C	-4.867217	-2.958221	0.340260
C	-6.051821	-2.442902	-0.146276
C	4.866956	-2.958527	0.340215
C	6.051589	-2.443265	-0.146290
C	6.066784	-1.197338	-0.804669
C	4.898179	-0.476891	-0.963996
C	-4.898279	-0.476628	-0.964033
C	-6.066934	-1.197000	-0.804691
H	-7.002540	-0.802271	-1.187386
H	4.847677	-3.921004	0.844406
H	6.975921	-2.998999	-0.025752
H	7.002422	-0.802655	-1.187331
H	4.909952	0.486293	-1.467233
H	-4.909995	0.486539	-1.467304
H	-6.976179	-2.998595	-0.025748
H	-4.848004	-3.920699	0.844453

***o*-CB-Pent \_ CT conformer (full optimization)**

C	2.095076	2.876018	0.000995
C	0.058017	1.422257	-0.000391
B	-1.121889	3.926970	-0.000263
B	1.004887	2.377463	1.164849
B	1.628995	4.138077	0.889956
B	1.629863	4.138618	-0.887668
B	1.006004	2.378199	-1.164218
B	-0.839868	2.424558	-0.906623
B	-0.033857	3.892084	-1.412655
B	0.317463	4.925355	0.000741
B	-0.035242	3.891273	1.413183
B	-0.840757	2.424072	0.905517
H	-1.604900	1.920394	1.663025
H	-1.603278	1.921332	-1.665174
H	1.414980	1.755734	-2.093343
H	-0.360355	4.324668	-2.472703
H	2.427866	4.664347	-1.594945
H	0.210628	6.111581	0.001037



H	2.426314	4.663377	1.598321
H	-0.362741	4.323272	2.473158
H	1.413015	1.754436	2.093965
H	-2.205684	4.423471	-0.000650
C	-0.081985	-0.041284	-0.000519
C	-1.381044	-0.681231	-0.000465
C	1.081890	-0.890017	-0.000186
C	-2.596842	0.011167	-0.001341
C	-1.475858	-2.131933	0.000684
C	0.949832	-2.333716	0.000973
C	2.382665	-0.384999	-0.000985
C	-3.844032	-0.638560	-0.001073
H	-2.624147	1.087938	-0.002354
C	-2.719677	-2.781088	0.001026
C	-0.318425	-2.914845	0.001485
C	2.081888	-3.163458	0.001523
H	2.544735	0.678004	-0.002139
C	3.519804	-1.211916	-0.000604
C	-3.917341	-2.068009	0.000193
H	-2.740734	-3.868078	0.001953
H	-0.409606	-3.998561	0.002440
C	3.372946	-2.636919	0.000783
H	1.940408	-4.241489	0.002477
H	3.128725	2.555051	0.001490
C	-5.191427	-2.707020	0.000520
C	-5.054632	0.108681	-0.002018
C	-6.264200	-0.534741	-0.001648
H	-7.183460	0.041611	-0.002333
C	-6.334725	-1.956217	-0.000430
H	-7.305699	-2.440195	-0.000025
C	4.534652	-3.463439	0.001245
C	4.830685	-0.660152	-0.001594
C	5.927195	-1.481774	-0.001124
H	6.924201	-1.053473	-0.001931
C	5.779642	-2.897052	0.000376
H	6.664978	-3.523738	0.000793
H	-5.233535	-3.792054	0.001637
H	-5.000626	1.193183	-0.002958
H	4.409223	-4.542050	0.002402
H	4.947081	0.419381	-0.002762

## Appendix C. Rights and Permissions

- Figure 1.2: “Reprinted with permission from [*INTERNATIONAL REVIEWS IN PHYSICAL CHEMISTRY* 2016, 35, 69-142]. Copyright 2016 Taylor & Francis Online”
- Figure 1.6: “Reprinted with permission from [*ANGEWANDTE CHEMIE INTERNATIONAL EDITION* 2013, 52, 11, 3222-3226]. Copyright 2013 Wiley-CVH Verlag GmbH & Co. KGaA, Weinheim.”
- Chapter 3: “Reprinted by permission from Springer Nature: Springer J. MOL. MODEL., Tahaoğlu, D., Alkan, F. & Durandurdu, M. Theoretical investigation of substituent effects on the relative stabilities and electronic structure of  $[B_nX_n]^{2-}$  clusters. (2021). Copyright 2021 Springer Nature.”  
<https://doi.org/10.1007/s00894-021-04980-1>
- Chapter 4: “Reprinted with permission from [*J. PHYS. CHEM. A* 2022, XXXX, XXX, XXX-XXX]. Copyright 2022 American Chemical Society.”  
<https://pubs.acs.org/doi/10.1021/acs.jpca.2c02435>

# CURRICULUM VITAE

## EMPLOYMENT

**2013 –** Teaching/Research Assistant in Abdullah Gül University  
Department of Nanotechnology Engineering

## EDUCATION

**2016 – 2022** **PhD.**, Materials Science and Mechanical Engineering  
Abdullah Gül University, Kayseri/Turkey  
Advisor: Prof. Dr. Murat Durandurdu, Assist. Prof. Fahri Alkan

**2019 – 2020** **PhD.** in Theoretical and Computational Chemistry (as a short-term student)  
Ruprecht-Karls-Universität Heidelberg, Heidelberg/Germany

**2013 – 2016** **M.Sc.** in Advanced Materials and Nanotechnology  
Abdullah Gül University, Kayseri/Turkey  
Advisor: Assoc. Prof. Dr. Murat Çıtır

**2005 – 2010** **B.Sc.** in Chemical Engineering  
Hacettepe University, Ankara/Turkey

## SCHOLARSHIP/GRANT

**2019 – 2020** **Overseas Research Scholarship for Research Assistants,**  
Higher Education Council (YÖK) of Turkey

**2014** **IMID 2014 - Student Travel Grant – South Korea**

## PUBLICATIONS

### Journals That Entered SCI, SSCI, and AHCI Indexes

- I. TAHAOĞLU DUYGU, USTA HAKAN, ALKAN FAHRİ (2022). Revisiting the Role of Charge Transfer on the Emission Properties of Carborane-Fluorophore Systems: a TDDFT Investigation. JOURNAL OF PHYSICAL CHEMISTRY A, (Accepted) Doi: 10.1021/acs.jpca.2c02435
- II. MENDUTI LUIGI, BALDOLI CLARA, ARNABOLDI SERENA, DREUW ANDREAS, TAHAOĞLU DUYGU, BOSSI ALBERTO, LICANDRO EMANUELA (2022). (Dimesityl)boron Benzodithiophenes: Synthesis, Electrochemical, Photophysical and Theoretical Characterization. CHEMISTRYOPEN, 11, e2021002, Doi: 10.1002/open.202100265
- III. TAHAOĞLU DUYGU, ALKAN FAHRİ (2021). Theoretical investigation of substituent effects on the relative stabilities of  $[B_nX_n]^{2-}$  clusters. JOURNAL OF MOLECULAR MODELLING, 27:365, Doi:10.1007/s00894-021-04980-1
- IV. TAHAOĞLU DUYGU, DURANDURDU MURAT (2018). Solute aggregation in  $Ca_{72}Zn_{28}$  metallic glass. JOURNAL OF NON-CRYSTALLINE SOLIDS, 500, 410-416., Doi: 10.1016/j.jnoncrysol.2018.08.030
- V. TAHAOĞLU DUYGU, DURANDURDU MURAT (2018). Permanent densification of amorphous zinc oxide under pressure: A first-principles study. JOURNAL OF NON-CRYSTALLINE SOLIDS, 481, 27-32., Doi: 10.1016/j.jnoncrysol.2017.10.016

### Refereed Congress / Symposium Publications in Proceedings

- I. TAHAOĞLU DUYGU, ALKAN FAHRİ (2021). Pondering Over the Photophysical Properties of Anthracene-Carborane Dyad in Solution. IATS'21: International Advanced Technologies Symposium
- II. TAHAOĞLU DUYGU, DURANDURDU MURAT (2018). Derivative Structures of Closo Boron Hydride Cluster,  $B_{16}X_{16}$ : A DFT Study. CSC2018: International Computational Science Congress
- III. TAHAOĞLU DUYGU, DURANDURDU MURAT (2018). Stability Investigation of  $B_{16}H_{16}^{2-}$  Derivatives by DFT Calculations. International Conference on Materials Science and Technology (IMSTEC) in Cappadocia
- IV. TAHAOĞLU DUYGU, DURANDURDU MURAT (2018). Effects of Production Methods on Structural and Mechanical Properties for Metallic  $Ca_{72}Zn_{28}$  Glass-A DFT

Study. The International Conference on Materials Science Mechanical and Automation Engineering and Technology (IMSMATEC'18)

- V. TAHAOĞLU DUYGU, DURANDURDU MURAT (2017). Metallic  $\text{Ca}_{72}\text{Zn}_{28}$  Glass from First Principle Molecular Dynamics Simulations. International Congress on Chemistry and Materials Science
- VI. TAHAOĞLU DUYGU, DURANDURDU MURAT (2017). Investigation of Phase Transformation of Amorphous Zinc Oxide under Pressure: a DFT Study. Turkish Physics Association 33<sup>rd</sup> International Physics Congress
- VII. TAHAOĞLU DUYGU, Essy Kouadio Fodyo, ÇITIR MURAT (2016). Interaction of cysteine with Group Ib ( $\text{Cu}^+$ ,  $\text{Ag}^+$ ,  $\text{Au}^+$ ) and IIb ( $\text{Zn}^{2+}$ ,  $\text{Cd}^{2+}$ ,  $\text{Hg}^{2+}$ ) metal cations: a theoretical study. International Conference on Quantum Science and Applications (ICQSA-2016)
- VIII. TAHAOĞLU DUYGU, USTA HAKAN, ŞEN ÜNAL, ÇITIR MURAT (2015). Kinetic Study on Catalytic Degradation of Organic Dyes with Copper Nanowire Catalyst. 2nd International Nanoscience and Nanotechnology for Next Generation (NaNONG) 2015
- IX. TAHAOĞLU DUYGU, ÇITIR MURAT, ŞEN ÜNAL, CANLIER ALİ (2014). Experimental Methods for Thin Layer Coating of Metal Nanowires with Inert Metals Through Galvanic Exchange Reactions. The 14th International Meeting on Information Display (IMID14)